University of Central Florida
STARS

Electronic Theses and Dissertations, 2004-2019

2012

Nonlinear Dynamic Modeling, Simulation And Characterization Of The Mesoscale Neuron-electrode Interface

Vaibhav Thakore
University of Central Florida

Part of the Physics Commons
Find similar works at: https://stars.library.ucf.edu/etd
University of Central Florida Libraries http://library.ucf.edu

This Doctoral Dissertation (Open Access) is brought to you for free and open access by STARS. It has been accepted for inclusion in Electronic Theses and Dissertations, 2004-2019 by an authorized administrator of STARS. For more information, please contact STARS@ucf.edu.

STARS Citation

Thakore, Vaibhav, "Nonlinear Dynamic Modeling, Simulation And Characterization Of The Mesoscale Neuron-electrode Interface" (2012). *Electronic Theses and Dissertations, 2004-2019*. 2465.
https://stars.library.ucf.edu/etd/2465

Showcase of Text, Archives, Research & Scholarship

NONLINEAR DYNAMIC MODELING, SIMULATION AND CHARACTERIZATION OF THE MESOSCALE NEURON-ELECTRODE INTERFACE

by

VAIBHAV THAKORE
B.S. in Physics (Honors) University of Delhi, 1997
M.S. in Physics, Indian Institute of Technology Delhi, 1999
M.Tech. in Solid State Materials, Indian Institute of Technology Delhi, 2001

A dissertation submitted in partial fulfillment of the requirements
for the degree of Doctor of Philosophy
in the Department of Physics
in the College of Sciences
at the University of Central Florida
Orlando, Florida

Fall Term
2012

Major Professors:
James J. Hickman (Chair)
Eduardo Mucciolo (Co-Chair)

© 2012 Vaibhav Thakore

ABSTRACT

Extracellular neuroelectronic interfacing has important applications in the fields of neural prosthetics, biological computation and whole-cell biosensing for drug screening and toxin detection. While the field of neuroelectronic interfacing holds great promise, the recording of high-fidelity signals from extracellular devices has long suffered from the problem of low signal-to-noise ratios and changes in signal shapes due to the presence of highly dispersive dielectric medium in the neuron-microelectrode cleft. This has made it difficult to correlate the extracellularly recorded signals with the intracellular signals recorded using conventional patch-clamp electrophysiology. For bringing about an improvement in the signal-to-noise ratio of the signals recorded on the extracellular microelectrodes and to explore strategies for engineering the neuron-electrode interface there exists a need to model, simulate and characterize the cell-sensor interface to better understand the mechanism of signal transduction across the interface.

Efforts to date for modeling the neuron-electrode interface have primarily focused on the use of point or area contact linear equivalent circuit models for a description of the interface with an assumption of passive linearity for the dynamics of the interfacial medium in the cell-electrode cleft. In this dissertation, results are presented from a nonlinear dynamic characterization of the neuroelectronic junction based on Volterra-Wiener modeling which showed that the process of signal transduction at the interface may have nonlinear contributions from the interfacial medium. An optimization based study of linear equivalent circuit models for representing signals recorded at the neuron-electrode interface subsequently

proved conclusively that the process of signal transduction across the interface is indeed nonlinear. Following this a theoretical framework for the extraction of the complex nonlinear material parameters of the interfacial medium like the dielectric permittivity, conductivity and diffusivity tensors based on dynamic nonlinear Volterra-Wiener modeling was developed. Within this framework, the use of Gaussian bandlimited white noise for nonlinear impedance spectroscopy was shown to offer considerable advantages over the use of sinusoidal inputs for nonlinear harmonic analysis currently employed in impedance characterization of nonlinear electrochemical systems.

Signal transduction at the neuron-microelectrode interface is mediated by the interfacial medium confined to a thin cleft with thickness on the scale of 20-110 nm giving rise to Knudsen numbers (ratio of mean free path to characteristic system length) in the range of 0.015 and 0.003 for ionic electrodiffusion. At these Knudsen numbers, the continuum assumptions made in the use of Poisson-Nernst-Planck system of equations for modeling ionic electrodiffusion are not valid. Therefore, a lattice Boltzmann method (LBM) based multiphysics solver suitable for modeling ionic electrodiffusion at the mesoscale neuron-microelectrode interface was developed. Additionally, a molecular speed dependent relaxation time was proposed for use in the lattice Boltzmann equation. Such a relaxation time holds promise for enhancing the numerical stability of lattice Boltzmann algorithms as it helped recover a physically correct description of microscopic phenomena related to particle collisions governed by their local density on the lattice. Next, using this multiphysics solver simulations were carried out for the charge relaxation dynamics of an electrolytic nanocapacitor with the intention of ultimately employing it for a simulation of the capacitive coupling between the neuron and the

planar microelectrode on a microelectrode array (MEA). Simulations of the charge relaxation dynamics for a step potential applied at t = 0 to the capacitor electrodes were carried out for varying conditions of electric double layer (EDL) overlap, solvent viscosity, electrode spacing and ratio of cation to anion diffusivity. For a large EDL overlap, an anomalous plasma-like collective behavior of oscillating ions at a frequency much lower than the plasma frequency of the electrolyte was observed and as such it appears to be purely an effect of nanoscale confinement. Results from these simulations are then discussed in the context of the dynamics of the interfacial medium in the neuron-microelectrode cleft. In conclusion, a synergistic approach to engineering the neuron-microelectrode interface is outlined through a use of the nonlinear dynamic modeling, simulation and characterization tools developed as part of this dissertation research.

Dedicated to all my gurus and teachers…

ACKNOWLEDGMENTS

First and foremost, I begin by thanking my dissertation advisor Professor James J. Hickman for his unstinted support and encouragement during the entire period of my doctoral degree. I will always be indebted and grateful to him for the freedom that he allowed me to pursue new approaches and ideas towards a solution of the problem assigned to me for my dissertation research. His firm and steady mentorship always helped me steer my research in the right direction and stay focused. His unwavering commitment to work and research sets a great example for emulation and shall continue to inspire me throughout my life. I consider myself fortunate to have had him as my dissertation advisor.

I thank my Dissertation Committee members Professors Eduardo Mucciolo, Aman Behal, Talat Rahman, Michael Johnson and Peter Molnar for their insightful comments and thought provoking questions that always helped me dig deeper for answers whenever I was stuck with a seemingly unsolvable research problem. I express heartfelt gratitude for the constant support and encouragement that they provided during my dissertation research.

I am grateful and indebted to Dr. Molnar for providing me with all the experimental data reported in this dissertation and for his friendship and help through the years. I also, wish to thank him and my colleague and friend Dr. Mainak Das (now faculty at IIT-Kanpur) for teaching me patch clamp electrophysiology.

I thank Dr. Behal for hosting me thrice at Clarkson University, Potsdam NY. The days that I spent working with Dr. Behal on Volterra-Wiener modeling at Clarkson University were unarguably the best days of my PhD student life, characterized by an intense focus on research and absence of any distractions. I shall always be grateful to him for this experience. The systematic step-by-step approach to modeling and simulation through validation of simulation results with a test problem, that I learnt by working with Dr. Behal, proved to be of immense help in my work with lattice Boltzmann method (LBM) based modeling.

I am grateful to Professor Ranganathan Kumar for allowing me to audit his course on Computational Fluid Dynamics and for teaching me the basics of it. One of his remarks during a class that will always stay with me was something to this effect “Dear students, it isn’t Colorful Fluid Dynamics (CFD) that you are trying to learn here. It is called Computational Fluid dynamics for a reason, so pay attention to the math that I am trying to teach you in the class.” This was a very sane advice indeed as I realized while working on LBM.

I am also indebted and grateful to Dr. Kumar’s student and my friend Dr. Amit Gupta (now faculty at IIT-Delhi) for providing me with a serial implementation of an LBM code for simulation of plane Poiseuille flow in a channel with periodic and bounce-back boundary conditions. I later parallelized and modified this code to simulate the entrance flow problem for the development of the LBM based multiphysics solver. Early discussions on LBM with Amit and the introduction to LBM literature that my interaction with him afforded me were most useful.

I also express my heartfelt gratitude and thanks to (late) Mr. Paul Alman, the former manager of Hybrid Systems Laboratory (HSL), for helping smooth the transition to life here in the United States, for his help in the move to Orlando from Clemson and for teaching me to drive.

Thanks are also due to Dr. Cathleen Wolf for her help with submission and preparation of manuscripts for journals, grants to funding agencies and other administrative support. Her extreme diligences in proof-reading journal articles before submission and after acceptance have saved me a lot of costly errors and valuable time over the years. Her work ethic and dedication to her job are truly amazing.

I also thank my officemate and colleague Craig Finch, and friends Kishore Reddy, Mainak Das, Neelima Bhargava, Suraj Vemuri, Sergio Tafur and Hari Prasad Paudel for numerous discussions on biology, physics and computing and just about everything else during the course of my PhD. Thanks are also due to all my wonderful colleagues of the past several years at the Hybrid Systems Laboratory for their help and support. Good times spent with them shall always stay with me in memory.

I gratefully acknowledge and thank my parents and brother Vivek for all their love and support during my academic pursuits and endeavors. I am also grateful for the countless blessings my late grandparents and father-in-law showered on me for success and happiness in life.

Last but not the least I thank my wonderful wife Arti for her unconditional love and support. Life would have been infinitely more difficult as a doctoral student had it not been for her incredible support, understanding and sacrifice. I consider myself truly fortunate and blessed to have her in my life!

Sincerely,
Vaibhav Thakore.

October 22nd, 2012
Orlando, FL USA.

TABLE OF CONTENTS

LIST OF FIGURES XIV

LIST OF TABLES XX

CHAPTER-1: INTRODUCTION 1

- 1.1. Background and significance 1
- 1.2. Motivation – Techniques for studying neural signals 2
  - 1.2.1. Patch-clamp electrophysiology 2
  - 1.2.2. Voltage sensitive dyes 3
  - 1.2.3. Extracellular recording devices 5
- 1.3. Previous studies on modeling and characterization of the cell-sensor interface 7
- 1.4. Objectives 8
- 1.5. Dissertation Outline 8

CHAPTER-2: NONLINEAR DYNAMIC CHARACTERIZATION OF THE NEURON-ELECTRODE JUNCTION 11

- 2.1. Introduction 11
- 2.2. Theory 12
- 2.3. Materials and methods 14
  - 2.3.1. Cell Culture 14
  - 2.3.2. Electrophysiological recordings 15
- 2.4. Results 18
- 2.5. Discussion 22
  - 2.5.1. Possible hypotheses 22
    - 2.5.1.1. Linear interface 22
    - 2.5.1.2. Nonlinear interface 23
- 2.6. Conclusions 24

CHAPTER-3: EQUIVALENT CIRCUIT MODELS FOR REPRESENTING EXTRACELLULAR RECORDINGS AT THE NEURON-ELECTRODE INTERFACE 25

- 3.1. Introduction 25
- 3.2. Materials and methods 28

3.2.1. Cell culture and electrophysiological recording protocols 28
3.2.2. Mathematical models 29
3.2.2.1. NG108-15 neurons 29
3.2.2.2. 'On-cell' neuron patch-electrode interface 32
3.2.2.3. Planar neuron-microelectrode interface 34
3.2.3. Optimization of the model parameters 35
3.2.3.1. NG108-15 neurons 35
3.2.3.2. Neuron-electrode interface 35
3.2.4. Numerical methods 37
3.3. Results 38
3.3.1. Ion-channel parameters for the NG-108-15 neurons 38
3.3.2. 'On-cell' neuron patch electrode interface 42
3.3.3. Planar neuron-microelectrode interface 45
3.4. Discussion 50
3.5. Conclusions 53
CHAPTER-4: THEORETICAL FRAMEWORK FOR EXTRACTION OF INTERFACE PARAMETERS USING NONLINEAR IMPEDANCE SPECTROSCOPY 55
4.1. Introduction 55
4.1.1. Impedance spectroscopy – Linear Vs Nonlinear 55
4.1.2. Neuron-microelectrode interface 56
4.2. Theoretical framework 58
4.2.1. Nonlinear dielectric medium 58
4.2.2. Connection to the impedance spectrum 62
4.3. Discussion 66
4.4. Conclusions 68
CHAPTER-5: DEVELOPMENT OF A LATTICE BOLTZMANN METHOD BASED MULTIPHYSICS SOLVER 69
5.1. Introduction 69
5.2. Lattice Boltzmann method - Background and a brief history of development 71
5.3. Lattice Boltzmann algorithm 73

- 5.4. Hydrodynamics – Simulating fluid flows 77
  - 5.4.1. Entrance flow problem 78
  - 5.4.2. Boundary conditions 79
  - 5.4.3. Validation results 80
- 5.5. Lattice Poisson-Boltzmann Method - Computing electric potential and field 83
  - 5.5.1. Theory 83
  - 5.5.2. Electrode-electrolyte interface 85
    - 5.5.2.1. Boundary conditions 85
    - 5.5.2.2. Validation results 86
- 5.6. Electroosmotic flow in a nanochannel 88
  - 5.6.1. Theory 89
  - 5.6.2. Boundary conditions 89
  - 5.6.3. Validation results 91
- 5.7. Advection-diffusion of solute particles 91
  - 5.7.1. Theory 91
    - 5.7.1.1. One dimensional advection-diffusion 91
    - 5.7.1.2. Two dimensional advection-diffusion 92
  - 5.7.2. Boundary conditions 92
  - 5.7.3. Validation Results 93
- 5.8. Surface chemical reaction in a microfluidic channel 95
  - 5.8.1. Boundary Conditions 95
  - 5.8.2. Validation results 97
- 5.9. Molecular speed dependent relaxation time – Entrance flow problem revisited 100
  - 5.9.1. Molecular speed dependent relaxation time 101
  - 5.9.2. Validation results 107
  - 5.9.3. Discussion 108
- 5.10. Conclusions 109

CHAPTER-6: SIMULATION OF IONIC ELECTRODIFFUSION AT MESOSCALE INTERFACES 110

- 6.1. Introduction 110

6.2. Theory 110

6.3. Boundary Conditions 114

6.4. Results 114

6.4.1. Spatially averaged current density J_{avg} 116

6.4.1.1. Effect of overlapping electric double layers and solvent viscosity 116

6.4.1.2. Effect of ratio of ionic diffusion coefficients 118

6.4.1.3. Effect of electrode separation 119

6.4.1.4. Summary and discussion 121

6.4.2. Oscillations in J_{avg} 123

6.4.3. Persistence of oscillations in J_{avg}: A quest for an answer 130

6.5. Discussion 144

6.6. Conclusions 148

CHAPTER-7: CONCLUSIONS AND FUTURE WORK 150

7.1. Conclusions 150

7.2. Future work 154

7.2.1. Lattice Boltzmann model of the neuron-electrode interface 154

7.2.2. Nonlinear impedance spectroscopy based on Volterra-Wiener modeling 154

REFERENCES 156

LIST OF FIGURES

Figure 1. An image showing a glass micropipette, microscope objective lens and the patching chamber on an electrophysiology rig. (Courtesy: Aditya Reddy Kolli, Hybrid Systems Laboratory, UCF.) 4

Figure 2. An image showing the patch clamp electrophysiology rig with an optical microscope and patch clamp amplifiers mounted on it. 4

Figure 3. An image showing a microelectrode array (MEA) mounted on an extracellular recording amplifier. A coin is placed by the side of the MEA to give an idea of its size. (Courtesy: Maria Stancescu, Hybrid Systems Laboratory, UCF) 6

Figure 4. A schematic of the neuron-microelectrode interface 6

Figure 5. A neuron covering a microelectrode and being stimulated with bandlimited Gaussian white noise through a glass micropipette. 15

Figure 6. Examples of (A) Inward sodium and outward potassium currents obtained under voltage clamp from the patched neuron covering the microelectrode, (B) Intracellular action potentials, and, (C) their corresponding extracellular responses as recorded on the microelectrode. 17

Figure 7. A schematic for the characterization of the neuron-electrode junction using bandlimited Gaussian white noise. 18

Figure 8. (A) First, and, (B) second order Wiener kernels computed from the input-output records corresponding to Gaussian white noise stimulus obtained from the neuron electrode junction. 20

Figure 9. (A) Intracellular action potential as recorded from the neuron-electrode system shown in Figure 5, and, (B) Actual output as recorded on the extracellular microelectrode (solid line), linear predicted output from the first order kernel (dotted), quadratic predicted output from the second order kernel (dash-dot-dash) and the total predicted output obtained by summing the outputs obtained from the two Wiener kernels (dashed). 21

Figure 10 (A) An illustration of the experimental arrangement for the electrophysiological characterization of the 'on-cell' neuron-patch electrode and neuron-microelectrode interfaces.

(B) An image of a NG108-15 neuron covering a planar microelectrode on an MEA interfaced simultaneously to intracellular and 'on-cell' extracellular Ag/AgCl patch electrodes. 27

Figure 11. Schematics of the point contact equivalent circuit models for (A) the 'on-cell' neuron-patch electrode interface and (B) the neuron-microelectrode interface. V_o represents the extracellular output. 33

Figure 12. A comparison of the simulated results with the experimentally recorded intracellular signals after an optimization of the ion-channel parameters. (A1 and B1) Experimental voltage clamp signals recorded using 10mV potential steps starting from a holding potential of -85mV (solid line) and their corresponding simulated voltage clamp signals (dotted line) using optimized ion-channel parameters for Cell 1 and Cell 2 respectively (See Table I, A and B). Currents to the left of the dashed black vertical lines represent inward sodium currents while to the right of the lines outward potassium currents are shown. (A2 and B2) Experimental sub- (solid line) and supra-threshold (solid line) intracellularly recorded current clamp signals from Cell 1 (Sub-threshold current injection, $I_{inj} = 560\,pA$ and supra-threshold current injection, $I_{inj} = 760\,pA$, $\Delta t = 4\,ms$; membrane capacitance $C_m = 70pF$; and, resting membrane potential $V_m^r = -54.6\,mV$) and Cell 2 (Sub- and supra-threshold current injection, $I_{inj} = 1180\,pA$, $\Delta t = 4\,ms$; membrane capacitance $C_m = 80pF$; and, resting membrane potential $V_m^r = -40.0\,mV$) respectively. Simulated sub- (dotted line) and supra- threshold (dotted line) intracellular current clamp signals for Cell 1 and Cell 2 using optimized ion-channel parameters shown in Table I, A and B. 39

Figure 13. A comparison of the simulated and the experimental results for the extracellular signals recorded from the 'on-cell' neuron-patch electrode interfaces for Cell 1 and Cell 2 after optimization of the point contact equivalent circuit model (Figure 11 A) parameters. (A1 and B1) Sub-threshold stimulation for Cell 1 and Cell 2 respectively. (A2 and B2) Supra-threshold stimulation for Cell 1 and Cell 2 respectively. (See Table II, A and B, for values of optimized equivalent circuit parameters.) 43

Figure 14. A comparison of the simulated and the experimental extracellular signals recorded from the neuron-microelectrode interface corresponding to the stimulation of Cell 1 (Figure 12 A2) after optimization of the point contact equivalent circuit model (Figure 11 B) parameters.

(A) Sub-threshold stimulation and (B) Supra-threshold stimulation. (See Table IV for the corresponding values of the equivalent circuit parameters.) 48

Figure 15. A schematic of the experimental arrangement for the extraction of nonlinear dielectric permittivity and conductivity of the interfacial medium using impedance spectroscopy based on Volterra-Wiener modeling. An intracellular current monitor is employed through use of patch-clamp electrophysiology to ensure that all of output response current flows through the interfacial medium to the ground electrode and there is little or no current flowing through the neural membrane during impedance characterization. 58

Figure 16. A schematic of the inter-relationship between different electrokinetic processes and their coupling with the neuronal dynamics using Hodgkin-Huxley equations........................... 70

Figure 17. A schematic showing the nine directional density distributions and the discrete particle velocities for the two dimensional D2Q9 lattice 76

Figure 18. A schematic showing the streaming of the density distribution functions on the lattice defining the simulation domain from time t to $t + \Delta t$. 76

Figure 19. Pressure driven flow in a channel connecting two reservoirs.................................. 78

Figure 20. Fully developed Poiseuille flow in a microfluidic channel (A) velocity profile and (B) Pressure gradient along the length of the channel. 81

Figure 21. (A) Steady state parabolic flow profile across the width of the channel. (B) Pressure gradient along the length of the channel for a fully developed Poiseuille flow 82

Figure 22. Results for electric (A) potential and (B) electric field profiles computed using Lattice Poisson Boltzmann Method compared with results obtained from Poisson's equation linearized using Debye-Huckel approximation for various electrode surface potentials (150, 100, 50, 30 and 10 mV) in a 0.1 mM 1:1 electrolyte solution. 87

Figure 23. (A) Streamwise velocity profiles for electroosmotic flows in channels with widths of 100, 200 and 400 nm with a zeta potential of $\zeta = -50$ mV, $c_{\infty} = 0.1$ mM, solvent viscosity of $\upsilon = 1.787 \times 10 - 5$ m^2/s and a lateral electric field of $E = 500$ V/m. (B) Results from Tang et al, J. App. Phys. 100 ,094908 (2006) for comparison... 90

Figure 24. Advection-diffusion of an instantaneous point source created in the center of the simulation domain at $t = 0$. The peaks from left to right denote particle concentration profiles

at 0.77, 1.54, 2.31 and 3.08 ns. 93
Figure 25. Concentration profiles of particles after 0.44 ns for a two-dimensional advection-diffusion of particles for corresponding to an instantaneous point source created at the center of the simulation domain at $t = 0$.(A) Theoretical plot and (B) LBM simulation. 94
Figure 26. A schematic depicting the boundary conditions on solute concentration and fluid flow for instantaneous surface chemical reaction on the upper wall of a microfluidic channel. 96
Figure 27. LBM simulation results for solute concentration profiles as a function of different Peclet numbers in a microfluidic channel with instantaneous chemical reaction on the upper wall that fixes the solute concentration to zero for all times on the reaction wall 98
Figure 28. Results obtained using the commercially available multiphysics solver CFD-ACE+ for solute concentration profiles as a function of different Peclet numbers in a microfluidic channel with instantaneous chemical reaction on the upper wall that fixes the solute concentration to zero for all times on the reaction wall 99
Figure 29. Representation of a binary collision between two molecules in the center of mass frame. 103
Figure 30. Poiseuille flow in a microfluidic channel computed using a molecular speed dependent relaxation time based LBM algorithm. (A) Fluid velocity, (B) Pressure gradient and (C) Non-dimensional collision frequency. 105
Figure 31. Poiseuille flow in a microfluidic channel computed using a molecular speed dependent relaxation time based LBM algorithm. (A) Steady state parabolic flow profile across the width of the channel. (B) Pressure gradient along the length of the channel for a fully developed Poiseuille flow. 106
Figure 32. Effect of solvent viscosity μ_{solv} on the spatially averaged current density for an electric double layer overlap of $\alpha = 1.4$. 116
Figure 33. Effect of solvent viscosity μ_{solv} on the spatially averaged current density for an electric double layer overlap of $\alpha = 0.65$. 117
Figure 34. Effect of solvent viscosity μ_{solv} on the spatially averaged current density for an electric double layer overlap of $\alpha = 0.1$. 117
Figure 35. Effect of cation to anion diffusion coefficient ratio on spatially averaged current

density for $\alpha = 1.4$. 118

Figure 36. Effect of cation to anion diffusion coefficient ratio on spatially averaged current density for $\alpha = 0.1$. 119

Figure 37. Effect of electrode separation on the spatially averaged current density for bulk electrolyte concentration of $n_b = 4.6$ mM. 120

Figure 38. Effect of electrode separation on the spatially averaged current density for bulk electrolyte concentration of $n_b = 92.5$ mM. 120

Figure 39. Oscillating electric potential ψ and y-component of the electric field E_y for EDL overlap $\alpha = 1.4$ and cation to anion diffusion coefficient ratio of $1:1$. 124

Figure 40. Oscillating cation and anion density distributions for EDL overlap $\alpha = 1.4$ and cation to anion diffusion coefficient ratio of $1:1$. 125

Figure 41. Oscillating non-dimensional cation and anion current density distributions for EDL overlap $\alpha = 1.4$ and cation to anion diffusion coefficient ratio of $1:1$. 126

Figure 42. Monotonic behavior of electric potential ψ and y-component of the electric field Ey for EDL overlap $\alpha = 0.1$ and cation to anion diffusion coefficient ratio of $1:1$. 127

Figure 43. Monotonic behavior of cation and anion density distributions for EDL overlap $\alpha = 0.1$ and cation to anion diffusion coefficient ratio of $1:1$. 128

Figure 44. Monotonic behavior of non-dimensional cation and anion current density distributions for EDL overlap $\alpha = 0.1$ and cation to anion diffusion coefficient ratio of $1:1$.. 129

Figure 45. Oscillatory behavior of the space averaged total, cation and anion current densities for an EDL overlap of $\alpha = 1.4$ and cation to anion diffusion coefficient ratio of $1:1$. 131

Figure 46. (Zoomed-In) Oscillatory behavior of the space averaged total, cation and anion current densities for an EDL overlap of $\alpha = 1.4$, cation to anion diffusion coefficient ratio of $1:1$ and $\mu_{solv} = 0.0008\ kgm^{-1}s^{-1}$ 131

Figure 47. Oscillatory behavior of the space averaged total, cation and anion current densities for an EDL overlap of $\alpha = 1.4$ and cation to anion diffusion coefficient ratio of $2:1$. 132

Figure 48. (Zoomed-In) Oscillatory behavior of the space averaged total, cation and anion current densities for an EDL overlap of $\alpha = 1.4$, cation to anion diffusion coefficient ratio of $2:1$ and $\mu_{solv} = 0.0008\ kgm^{-1}s^{-1}$ 132

Figure 49. Time evolution of y-component of cation u_y^{Cn} and anion u_y^{An} velocities for the times when the space-averaged cation J_{Cn}^{avg} and anion J_{An}^{avg}current densities are in-phase for an EDL overlap of $\alpha = 1.4$. 133

Figure 50. Time evolution of cation ω_{Cn} $and\, anion\, \omega_{An}$ collision frequencies for the times when the space-averaged cation $J_{Cn}^{avg}$and anion J_{An}^{avg} current densities are in-phase for an EDL overlap of $\alpha = 1.4$. 134

Figure 51. Time evolution of y-component of cation $u_y^{Cn}$and anion u_y^{An}velocities for the times when the space-averaged cation $J_{Cn}^{avg}$and anion J_{An}^{avg} current are out-of-phase for an EDL overlap of $\alpha = 1.4$. 135

Figure 52. Time evolution of cation ω_{Cn} and anion ω_{An} collision frequencies for the times when the space-averaged cation $J_{Cn}^{avg}$and anion J_{An}^{avg} current densities are out-of-phase for an EDL overlap of $\alpha = 1.4$. 136

Figure 53. Time evolution of y-component of the electric field E_y and spatial cross-correlation J_y^{corr} of ionic flux densities J_{Cn}^f and J_{An}^f for the times when the space-averaged cation J_{Cn}^{avg} and anion J_{An}^{avg} current densities are in-phase for an EDL overlap of $\alpha = 1.4$. 137

Figure 54. Time evolution of y-component of the electric field E_y and spatial cross-correlation J_y^{corr} of ionic flux densities J_{Cn}^f and J_{An}^f for the times when the space-averaged cation J_{Cn}^{avg} and anion J_{An}^{avg} current densities are out-of-phase for an EDL overlap of $\alpha = 1.4$. 138

Figure 55. Time evolution of y-component of the electric field Ey and spatial cross-correlation J_y^{corr} of ionic flux densities J_{Cn}^f and J_{An}^f for the times when the space-averaged J_{Cn}^{avg} and J_{An}^{avg} are out-of-phase for $\alpha = 1.4$ and ionic diffusion coefficient ratio of $2{:}\,1$. 141

Figure 56. Time evolution of y-component of the electric field Ey and spatial cross-correlation J_y^{corr} of ionic flux densities J_{Cn}^f and J_{An}^f for an EDL overlap of $\alpha = 0.1$ and ionic diffusion coefficient ratio of $1{:}\,1$. 142

Figure 57. Dielectric slab in a capacitor. 143

Figure 58. A schematic of the sysnergistic approach advocated in this dissertation for engineering the neuron-microelectrode interface. 153

LIST OF TABLES

Table 1. Optimized ion channel parameters for (A) Cell 1 and (B) Cell 2 obtained by a fitting of the simulated current and voltage clamp intracellular signals to the experimentally recorded signals[a]. 40

Table 2. Optimized parameters of the point contact equivalent circuit model for the ‘on-cell’ neuron-patch electrode interfaces for (A) Cell 1 and (B) Cell 2b. 41

Table 3. nssr values for fitting of the simulated supra-threshold signal to experimental recordings after selective fixation of equivalent circuit parameter values at the sub-threshold level for the ‘on-cell’ patch electrode.......... 45

Table 4. Optimized parameters of the point contact equivalent circuit model of the neuron-microelectrode interface for Cell 1[b]. 49

CHAPTER-1: INTRODUCTION

1.1. Background and significance

A neuron encodes and expresses its response to environmental cues through a change in the shape and/or firing rate of action potentials. Action potentials are changes in the membrane potential of a neuron generated in response to an activation of the nonlinear ionic currents flowing across voltage gated ion channels in the neural cell membrane. The wide variety of sensory neurons observed in nature, specialized for survival of various organisms in constantly changing and often times hostile physical and chemical environs, makes them suitable as highly sensitive probes of their extracellular environment. The detection and analysis of action potential shapes and firing rates can, therefore, be employed for applications in high throughput functional screening of drugs or toxins [1-4]. On the other hand, changes in neural signal coordinates can also be an important indicator in ascertaining the physiological health of neurons themselves. An understanding of the factors affecting the health of neurons can, therefore, help advance our knowledge of the progression of various diseases of the nervous system and the brain and the effects accruing from traumatic injuries to them [5-7]. This can then enable development of more effective drug treatments and therapies for them. Further, a study of the network behavior of neurons can be employed for gaining significant insights into biological computation taking place in the brain, the most complex of all organs in any organism [8]. Biological organisms with their cognitive powers can process and integrate visual and other sensory inputs far better than the most advanced of supercomputers. Therefore, the knowledge of the network behavior of neurons thus gained can be employed for making better computers and functionally improved prosthetic devices. The study of neural action potential shapes, firing rates and network behavior thus assumes technological relevance for the advancement of human health and well being.

1.2. Motivation – Techniques for studying neural signals

Neural signals can be studied at various levels of hierarchy. Whole brain studies typically employ electroencephalography (EEG), magnetic resonance imaging or computer aided tomography [9, 10]. Organotypic slices in in-vitro cultures are used to study the interrelationship between different parts of the brain and information processing in networks of neurons involved in higher cognitive functions like memory formation, information retrieval and pattern recognition [11-13]. Typically, such an electrical characterization of the nervous tissue is carried out using patch-clamp technique, microelectrode arrays (MEAs), field effect transistor (FET) arrays or voltage sensitive dyes. In-vivo studies of nervous tissue can also be performed using patch-clamp electrophysiology or implanted microelectrode or FET arrays [14-17]. The work presented in this dissertation, however, concerns itself with the study of the neuroelectronic interface of dissociated single neurons with electrodes in in-vitro cultures.

1.2.1. Patch-clamp electrophysiology

Conventional technique of patch-clamp electrophysiology for studying electrical activity of neurons in in-vitro culture systems can be employed in two distinct modes: voltage clamp and current clamp. In voltage clamp mode, a step-by-step increment of membrane potential from a typical holding potential of -70 mV (hyperpolarized state of neuron) enables a study of the current-voltage relationship of the ionic currents flowing through the voltage-gated ion-channels in the neural membrane. The current clamp mode, on the other hand, is employed to study the electrical response of a neuron in the form of a free variation of its membrane potential upon stimulation with square current pulses that either depolarize or hyperpolarize a neuron. If the holding potential for the cell membrane is below the resting membrane potential (typically around -50 to -30 mV) of the neuron then the state of a neuron is referred to as hyperpolarized and if it is greater than the resting membrane potential then it is referred to as depolarized. The use of patch clamp electrophysiology to characterize the electrical properties of a neuron requires a breach of the neuronal membrane using a sharp glass micropipette for recording intracellular membrane currents or potentials (Figure 1). As a result, the signals recorded using patch-clamp electrophysiology are of the highest quality. However, the invasive nature of such a technique typically limits the life of a neuron to a few hours. Additionally, the experimental set-up for patch clamp electrophysiology demands a high level of operator skill, is extremely bulky and limits the number of cells being patched at a given time to at most two cells (Figure 2). These limitations make patch-clamp electrophysiology unsuitable and unattractive for applications in high-throughput screening of drugs and toxins, for study of neural network behavior or for chronic studies employing in-vitro models of neurodegenerative diseases or spinal cord injury.

1.2.2. Voltage sensitive dyes

Neural membrane potentials can also be studied using voltage sensitive dyes that are organic molecular probes which attach themselves to the cell membrane.

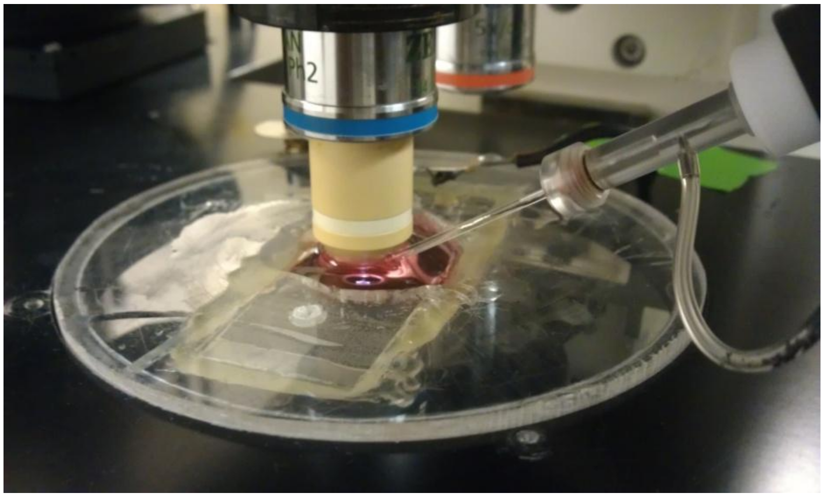

Figure 1. An image showing a glass micropipette, microscope objective lens and the patching chamber on an electrophysiology rig. (Courtesy: Aditya Reddy Kolli, Hybrid Systems Laboratory, UCF.)

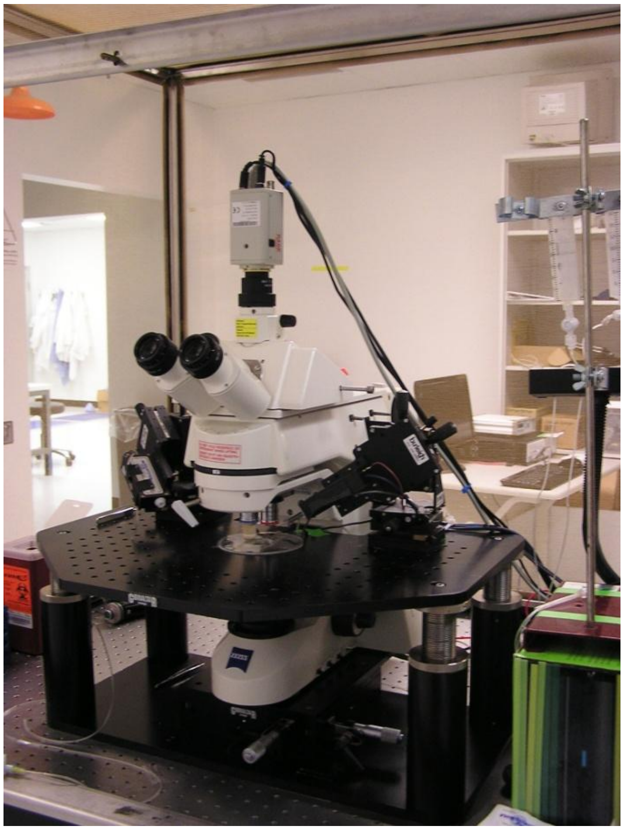

Figure 2. An image showing the patch clamp electrophysiology rig with an optical microscope and patch clamp amplifiers mounted on it.

Changes in membrane potentials lead to a change in the absorbance, fluorescence or birefringence of these molecular probes giving rise to an optically detectable signal that enables visualization of the neuron generated potentials. Besides suffering from problems of low signal to noise ratio, the use of voltage sensitive dyes, although non-invasive, proves to be toxic when employed for chronic experimental studies [4, 18]. Another problem associated with using voltage sensitive dyes for high throughput drug and toxin detection is that the dyes may themselves interfere with the drug or toxin chemistry [4, 18]. For this reason, the development of technology for non-invasive extracellular recording of neuron-generated potentials using microelectrode (MEAs) and field effect transistor (FET) arrays assumes great significance [2, 19, 20].

1.2.3. Extracellular recording devices

The use of compact extracellular recording devices like MEAs and FET arrays is also, however, not without its own set of problems (Figure 3). Typically, extracellular signals recorded through these extracellular devices get attenuated by three orders of magnitude as compared to the signals recorded using intracellular patch clamp electrophysiology. There also occurs a modification of the signal waveform due to the dispersive dynamics of the dielectric medium comprising the porous protein-glycocalyx matrix in the neuron-electrode cleft (Figure 4). The wealth of information present in the action potential shapes recorded using patch clamp electrophysiology is thus inaccessible for analysis in the extracellular recording methods employing MEAs and FET arrays.

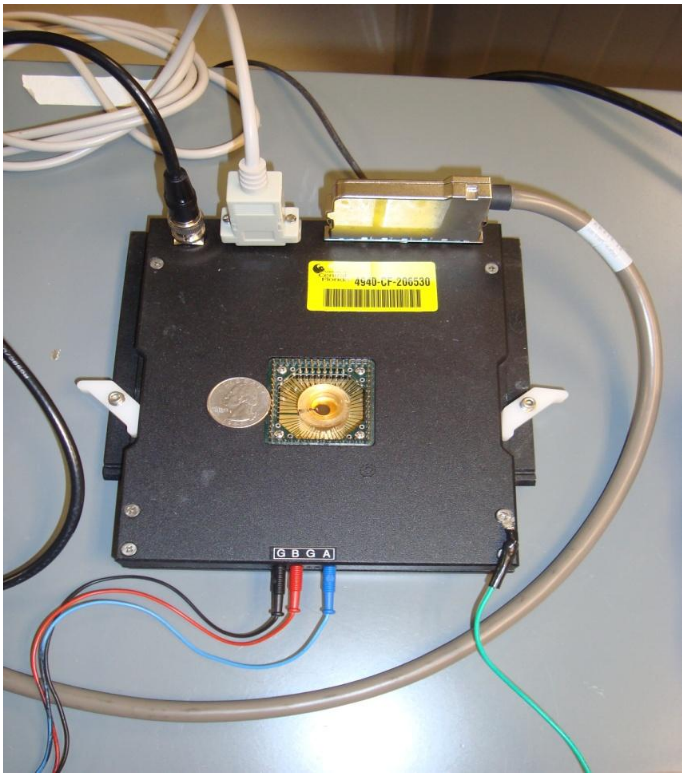
4940-CF-206530
G B G A

Figure 3. An image showing a microelectrode array (MEA) mounted on an extracellular recording amplifier. A coin is placed by the side of the MEA to give an idea of its size. (Courtesy: Maria Stancescu, Hybrid Systems Laboratory, UCF)

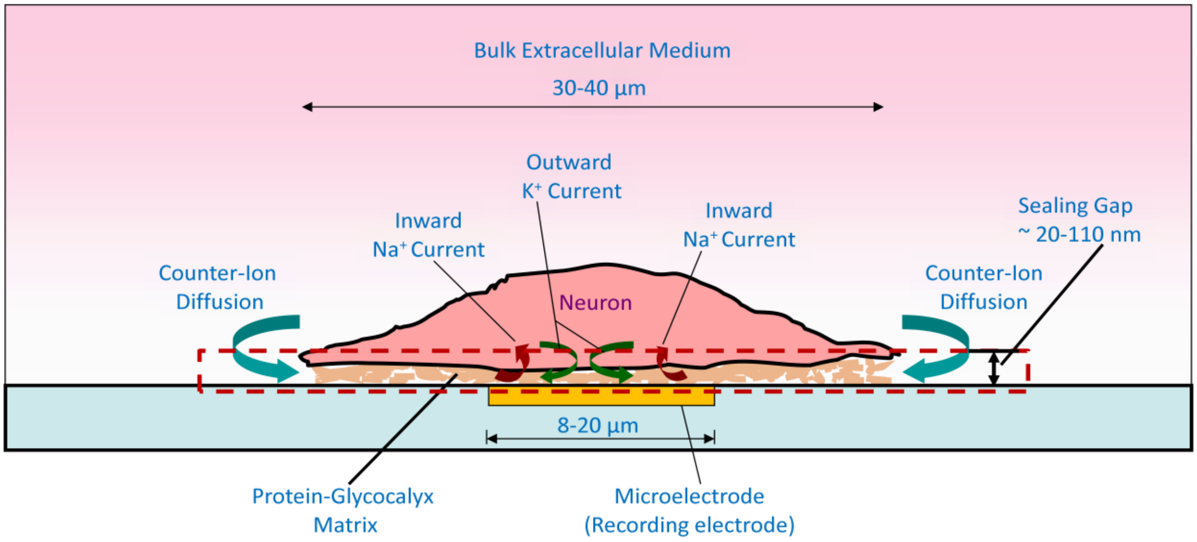
Bulk Extracellular Medium
30-40 μm
Outward K+ Current
Inward Na+ Current
Inward Na+ Current
Sealing Gap ~ 20-110 nm
Counter-Ion Diffusion
Counter-Ion Diffusion
Neuron
8-20 μm
Protein-Glycocalyx Matrix
Microelectrode (Recording electrode)

Figure 4. A schematic of the neuron-microelectrode interface

As a result, the problems associated with MEAs and FET arrays have limited their use to studies of changes in firing rate/pattern of action potentials in response to changes in environmental factors or in chronic experiments [19, 21, 22].

1.3. Previous studies on modeling and characterization of the cell-sensor interface

For the greater part so far, much of the effort on modeling the cell-sensor interface has focused on the use of point or area contact linear equivalent circuit [23-28] and finite element models [29-32] for a description of the interface with an assumption of passive linearity for the dynamics of the interfacial medium in the cell-electrode cleft. These models, therefore, fail to take in to account the complex processes of nonlinear electrodiffusion of ions through the porous protein-glycocalyx matrix and the dielectric dispersion involved in signal transduction across the neuron-electrode interface (Figure 4). Consequently, these models have proven to be inadequate for the correlation of the ion channel dynamics of an electrically active neuron with the potentials recorded on the extracellular microelectrode. For bringing about an improvement in the signal to noise ratio of the signals recorded on the extracellular microelectrodes and to explore strategies for engineering the cell-sensor interface using surface chemical modification of electrodes [33-35], microelectrode design or new electrode materials [36, 37], there exists a need to simulate and model the cell-sensor interface to better understand the mechanism of signal transduction across the interface. An understanding of the dynamics of the interfacial medium and the accompanying physicochemical changes during the process of signal transduction would then enable an identification of the tools and strategies necessary for systematically engineering the neuron-microelectrode interface for improving the signal to noise ratio of the extracellular recording devices.

1.4. Objectives

The goals of this dissertation project were, therefore, to develop tools that would allow for

1. A 'data-true' characterization of the neuron-electrode interface aimed at understanding the mechanism of signal transduction at the neuron-electrode junction.
2. Extraction of nonlinear material parameters like dielectric susceptibility, conductivity and ionic diffusivities for use in conjunction with a computational fluid dynamics model of the neuron-microelectrode interface to facilitate an engineering of the neuron-electrode interface.
3. A simulation of the transient dynamics of the nonlinear electrodiffusion of ions in the mesoscale neuron-electrode cleft.

To achieve the aforementioned goals a synergistic three pronged approach making use of Volterra-Wiener characterization, linear equivalent circuit and computational fluid dynamics modeling was employed.

1.5. Dissertation Outline

The rest of the dissertation is organized as follows:

Chapter 2 describes the 'data-true' characterization of the neuron-microelectrode junction through a Volterra-Wiener model estimated using Lee-Schetzen technique of cross-correlation from experimentally obtained stimulus-response data. The system identification results presented in the chapter show that there may or may not be any nonlinear contribution from the interfacial medium during signal transduction across the neuroelectronic interface [38].

Employing an optimization based study of the equivalent circuit models for representing signals recorded at the neuron-electrode interface Chapter 3 establishes that there is indeed a nonlinear contribution from the interfacial medium in the extracellular signal recorded at the metal microelectrode [39].

Chapter 4 develops a theoretical framework for the extraction of the material parameters of the interfacial medium using nonlinear impedance spectroscopy based on an estimation of a Volterra-Wiener model of the interface through I-V characterization.

Chapter 5 details the step-by-step development of a lattice Boltzmann method (LBM) based multiphysics solver aimed at the simulation of ionic electrodiffusion in mesoscale systems. Further, it introduces a lattice Boltzmann algorithm based on a molecular speed dependent relaxation time that holds promise for enhancing the numerical stability of the lattice Boltzmann equation.

Chapter 6 employs the multiphysics solver developed in chapter 5 along with the molecular speed dependent relaxation time to simulate the charge relaxation dynamics of overlapping electric double layers in an electrolytic nanocapacitor under differing conditions of double layer overlap, solvent viscosity, electrode separation and ratio of cation to anion diffusion coefficients.

Chapter 7 concludes the dissertation by outlining a synergistic approach to an engineering of the neuron-microelectrode interface through the use of Volterra-Wiener modeling in conjunction with lattice Boltzmann and equivalent circuit models of the interface developed as part of this dissertation.

CHAPTER-2: NONLINEAR DYNAMIC CHARACTERIZATION OF THE NEURON-ELECTRODE JUNCTION

2.1. Introduction

System identification is the technique of determining the transfer characteristics of a system based on its stimulus-response relationship. Models estimated using system identification can be classified in to two possible types: parametric and non-parametric [40, 41]. Both parametric and non-parametric models can be estimated using the experimentally obtained stimulus-response data records of the system. Parametric models make an assumption regarding the underlying structure of the system and as a consequence impose certain constraints on its dynamics. For example, equivalent circuit models of the neuron-electrode interface assume that the dynamics of the interface are linear and can be represented using a combination of resistors and capacitors. Such models have been estimated in the past using experimental input-output data records obtained through linear impedance spectroscopy that employs sinusoidal inputs to characterize the interface [28, 42-44]. Linear equivalent circuit representations of the neuron-electrode interface, since they assume an underlying structure in terms of the connectivity of the different circuit elements and thereby impose constraints on the dynamics of the system, are inherently ‘biased’ and hence not ‘data true’. On the contrary, non-parametric models such as the Volterra-Wiener models are estimated exclusively from the experimentally obtained stimulus-response data records without any assumption of an underlying structure for the system under study. Non-parametric Volterra-Wiener models are therefore both ‘unbiased’ and ‘data-true’.

In this chapter, results are presented from a Volterra-Wiener model of the neuron-electrode junction estimated through a nonlinear dynamic characterization using a bandlimited Gaussian white noise input stimulus.

2.2. Theory

The output $y(t)$ of a nonlinear causal, stationary and continuous system with a finite memory can be represented as a Volterra series in terms of its input $x(t)$ as

$$y(t) = k_0 + \int_0^\infty k_1(\tau)x(t-\tau)d\tau + \iint_0^\infty k_2(\tau_1,\tau_2)x(t-\tau_1)x(t-\tau_2)d\tau_1 d\tau_2$$

$$+\ldots+\int \ldots \int_0^\infty k_r(\tau_1,\ldots,\tau_r)x(t-\tau_1)\ldots x(t-\tau_r)d\tau_1 \ldots d\tau_r +\ldots \tag{1}$$

where kernels k_r represent the impulse response of the system given by

$$y(t) = k_0 + k_1(t) + k_2(t,t)+\ldots+k_r(t,\ldots,t)+\ldots \tag{2}$$

and integration over τ from 0 to ∞ embodies the effect of all past and present inputs to the system beginning at t = 0. In general, for practical finite memory systems of the kind considered here the integration is carried out from 0 to μ, the extent of the system memory. The rth order Volterra kernel describes the pattern of nonlinear interaction between r past stimulus impulses or epochs of a continuous input signal with regard to the effect that it has on the total system response. Based on equation (2) it can be seen that the impulse response of a nonlinear system includes contributions from the diagonals of all the kernels. The rth order interaction therefore includes contributions from not just the rth order kernel but also from kernels of order higher than r^{th} [41]. As a result, this complicates the process of kernel estimation or system identification using impulses. To overcome this problem Wiener showed that if one employs a bandlimited Gaussian white noise $x(t)$ as input stimulus and orthogonalizes the functionals in the Volterra series using a procedure similar to Gram-Schmidt orthogonalization then the output $y(t)$ can be expressed in terms of a series of orthogonal functionals G_i as

$$y(t) = \sum_{i=0}^{\infty} G_i[h_i(\tau_1, \dots \tau_i); x(t'), t' \leq t]$$

$$\begin{aligned} &= [h_0] + \left[\int_0^{\infty} h_1(\tau)x(t-\tau)d\tau\right] \\ &\quad + \left[\iint_0^{\infty} h_2(\tau_1,\tau_2)x(t-\tau_1)x(t-\tau_2)d\tau_1 d\tau_2 - P\int_0^{\infty} h_2(\tau_1,\tau_1)d\tau_1\right] \\ &\quad + \left[\iiint_0^{\infty} h_3(\tau_1,\tau_2,\tau_3)x(t-\tau_1)x(t-\tau_2)x(t-\tau_3)d\tau_1\, d\tau_2 d\tau_3 \right. \\ &\quad \left. - 3P\iint_0^{\infty} h_3(\tau_1,\tau_2,\tau_2)x(t-\tau_1)d\tau_1 d\tau_2\right] + \dots \end{aligned} \tag{3}$$

where h_i are the Wiener kernels and the terms in square brackets are the zeroth, first, second and third order Wiener functionals G_i respectively. Orthogonality of the Wiener functionals G_i implies zero covariance such that

$$E\left[G_i(t)G_j(t)\right] = 0, \forall\ i \neq j \text{ and } \forall\ t, t' \tag{4}$$

where $E[.]$ represents the expectation value operator. The zeroth order Wiener kernel is just the expectation value of the system output and is given by

$$h_0 = E[y(t)] \tag{5}$$

Now, making use of the Lee-Schetzen cross-correlation technique [45] which employs the fact that the odd moments of the Gaussian input signal $x(t)$ vanish identically, one can obtain the next three higher order Wiener kernels as

$$h_1(\tau) = \frac{1}{P}\left(\frac{1}{T-\tau}\int_0^T y_L(t)x(t-\tau)dt\right) \tag{6}$$

$$h_2(\tau_1,\tau_2) = \frac{1}{2P^2}\left(\frac{1}{T-\max\,[\tau_1,\tau_2]}\int_0^T y_Q(t)x(t-\tau_1)x(t-\tau_2)dt\right) \tag{7}$$

$$h_3(\tau_1,\tau_2,\tau_3) = \frac{1}{6P^3}\left(\frac{1}{T-\max\,[\tau_1,\tau_2,\tau_3]}\int_0^T y_C(t)x(t-\tau_1)x(t-\tau_2)x(t-\tau_3)dt\right) \tag{8}$$

where T is the total time length of the recorded data, τ_i are the lags, $y_L(t) = y(t) - G_0$, $y_Q(t) = y(t) - G_0 - G_1(t)$ and $y_C(t) = y(t) - G_0 - G_1(t) - G_2(t)$.

2.3. Materials and methods

2.3.1. Cell Culture

NG108-15 cell line (passage number: 16) was obtained from Dr. M. W. Nirenberg (NIH). NG108-15 cells were cultured according to published protocols [46, 47]. Briefly, stock was grown in T-25 and T-75 flasks in 90% Dulbecco's modified Eagle's medium (DMEM, GIBCO) supplemented with 10% Fetal Bovine Serum and HAT (GIBCO, 100x) supplement at 37°C and 5%

CO_2. Differentiation was induced by plating the cells in a serum-free defined medium (DMEM + B27 supplement, GIBCO) on the top of substrate embedded microelectrode arrays (MEAs, Multichannel Systems, Reutlingen, Germany, 10 µm electrode, 200 µm separation) at a density of 40,000 cells/dish. Before plating, MEAs were incubated with poly-D-lysine (Sigma, 10 µg/ml) for 1 hour at 37 °C.

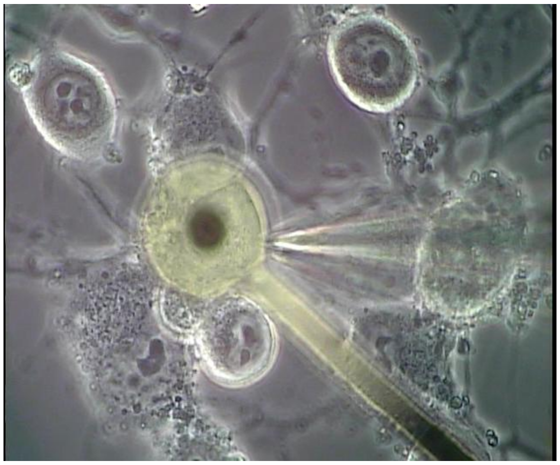

Figure 5. A neuron covering a microelectrode and being stimulated with bandlimited Gaussian white noise through a glass micropipette.

2.3.2. Electrophysiological recordings

On day 7 after plating of the cells on MEAs, the MEAs with cultured cells were transferred to the stage of a Zeiss Axioskop 2FS Plus microscope. Extracellular recordings from the substrate-embedded electrodes were performed with the help of a custom-made contact pad and an extracellular differential amplifier (Model 3000, A-M Systems). The extracellular solution for the recordings was DMEM (pH adjusted to 7.3 with HEPES, Sigma). Whole-cell patch clamp recordings were performed on neurons covering the microelectrodes completely (Figure 5). Cells on the electrodes were visualized by combining transmitted phase-contrast and reflected bright field illumination. Patch pipettes (4-6 $M\Omega$ resistance) were prepared from borosilicate glass (BF150-86-10; Sutter, Novato, CA) with a Sutter P97 pipette puller and were filled with intracellular solution containing (in mM) potassium gluconate 130, $MgCl_2$ 2, EGTA 1, HEPES 15, and ATP 5. Voltage clamp and current clamp experiments were performed with a Multiclamp 700A (Axon, Union City, CA) amplifier, Digidata 1322A interface, and pClamp 9 software.

The neuronal differentiation of the NG108-15 cells was confirmed by recording inward sodium (fast negative transients) and outward potassium currents (slow positive transients) in the voltage clamp mode and by measuring action potentials in the current clamp mode using a 200 ms depolarization stimulus (Figure 6 A and B). The corresponding extracellular response recorded on the microelectrode is shown in Figure 6 C.

Experiments employing white noise stimulation of the neuron-electrode junction were performed if the access resistance for the neuron was less than 15 $M\Omega$ and the action potential evoked a detectable signal on the extracellular electrode. For obtaining the input-output data records, neurons were stimulated through the intracellular patch pipette in voltage clamp mode with band limited (0-500 Hz) Gaussian white noise sampled at a rate of 9.8 kHz for 100 seconds (see Figure 7). The white noise signal was generated in MATLAB and imported to pCLAMP as a stimulus file. Whole cell capacitance and resistance were compensated but no series-resistance compensation was used. The holding membrane potential was -10 mV and the white noise stimulus spanning an amplitude range of ± 50 mV was superposed on this signal.

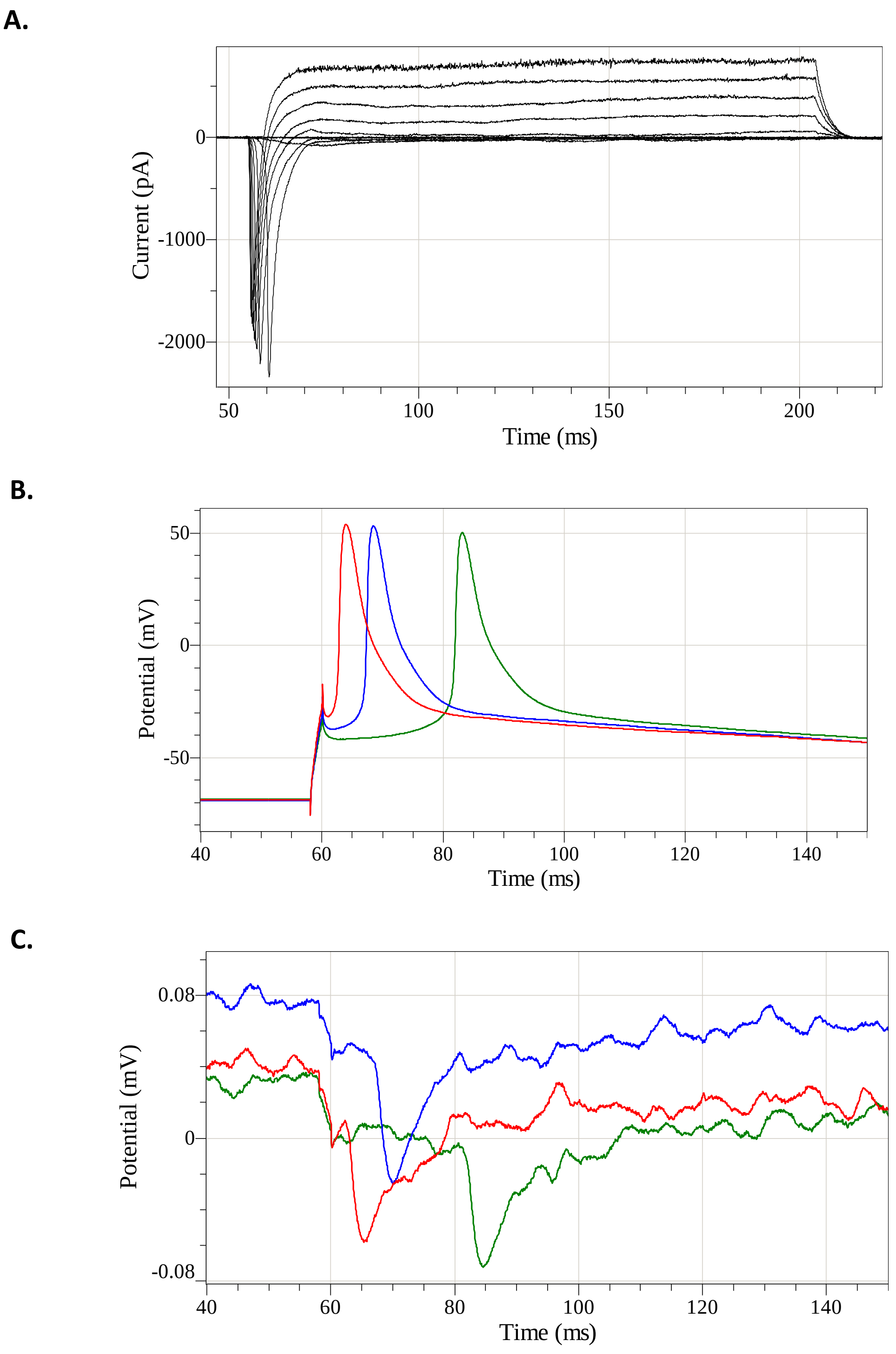

Figure 6. Examples of (A) Inward sodium and outward potassium currents obtained under voltage clamp from the patched neuron covering the microelectrode, (B) Intracellular action potentials, and, (C) their corresponding extracellular responses as recorded on the microelectrode.

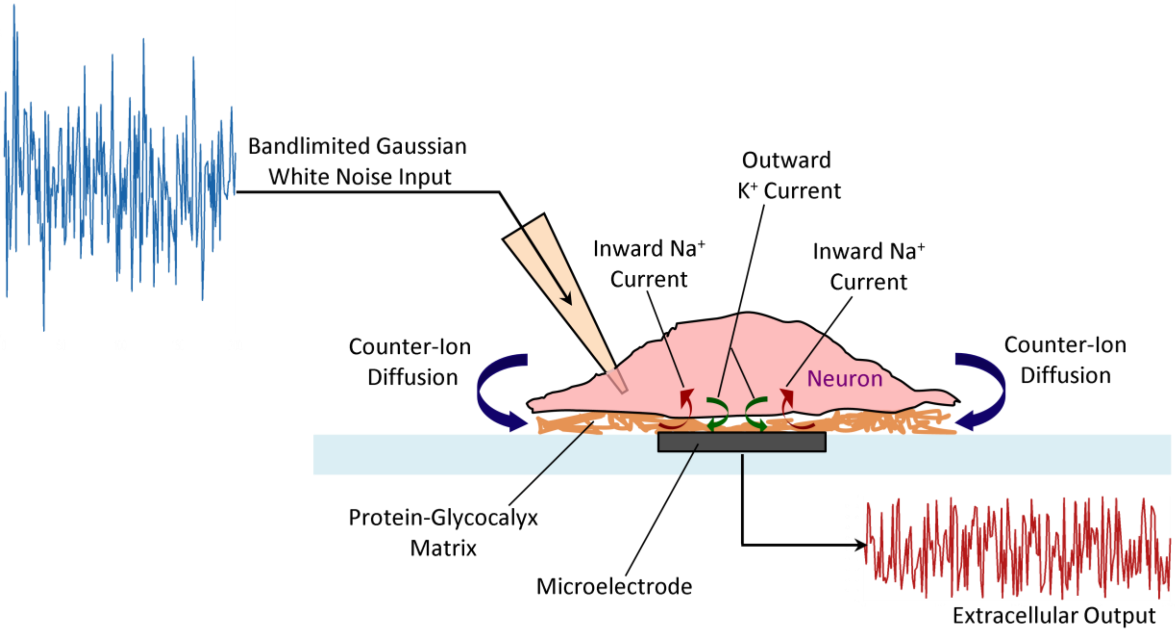
Bandlimited Gaussian
White Noise Input
Outward
K+ Current
Inward Na+
Current
Inward Na+
Current
Counter-Ion
Diffusion
Neuron
Counter-Ion
Diffusion
Protein-Glycocalyx
Matrix
Microelectrode
Extracellular Output

Figure 7. A schematic for the characterization of the neuron-electrode junction using bandlimited Gaussian white noise.

The extracellular signal was high and low pass filtered at 1Hz (using a second order Bessel filter) and 1 kHz (using a fourth order Bessel filter) respectively. The data, thus obtained, was then exported to Matlab for further analysis.

2.4. Results

For an estimation of the Volterra-Wiener model of a neuron-microelectrode junction, a bandlimited Gaussian white noise signal spanning the frequency and amplitude range of natural input for the system was employed to characterize the system. The non-parametric modeling of the neuron-electrode interface can be looked upon as a typical system identification problem involving determination of the stimulus-response transform wherein the neuron-generated potentials constitute the stimulus, the recorded extracellular potential on the microelectrode the response, and, the neuron-electrode cleft the stimulus transforming system. For the case of the neuron-electrode junction the model estimation was restricted to just the first and second order Wiener kernels. Figure 8 A and B show the first and second order Wiener kernels computed using the Lee-Schetzen technique of cross-correlation. As described in the experimental methods, the 1 Hz high pass Bessel filter was used to remove the slowly varying non-stationarities in the output signal that led to non-convergence of the first and second order kernels for even very large values of the time lags τ. These slowly varying non-stationarities could possibly be a result of the changes in the physiology of the cell due to a change in intracellular cytosolic factors upon impaling with a glass micropipette and gradual cell death occurring typically over a period of 1-2 hours. The 1 kHz low pass (fourth order) Bessel filter was used to limit the contribution of the high frequency noise to the output signal and frequencies at which there is no significant contribution from the frequency components present in the action potential generated by the neuron.

The response of the experimentally obtained Wiener kernels was then verified with the intracellular action potential serving as the test stimulus. Figure 9 A shows an intracellular action potential obtained from the neuron-electrode junction shown in Figure 5. Figure 9 B shows the corresponding predicted extracellular response with contributions from first and second order reconstructions obtained using the respective Wiener kernels. Also, the actual extracellular response recorded on the microelectrode is shown for comparison. It is evident that the predicted output closely follows the actual output recorded on the extracellular microelectrode.

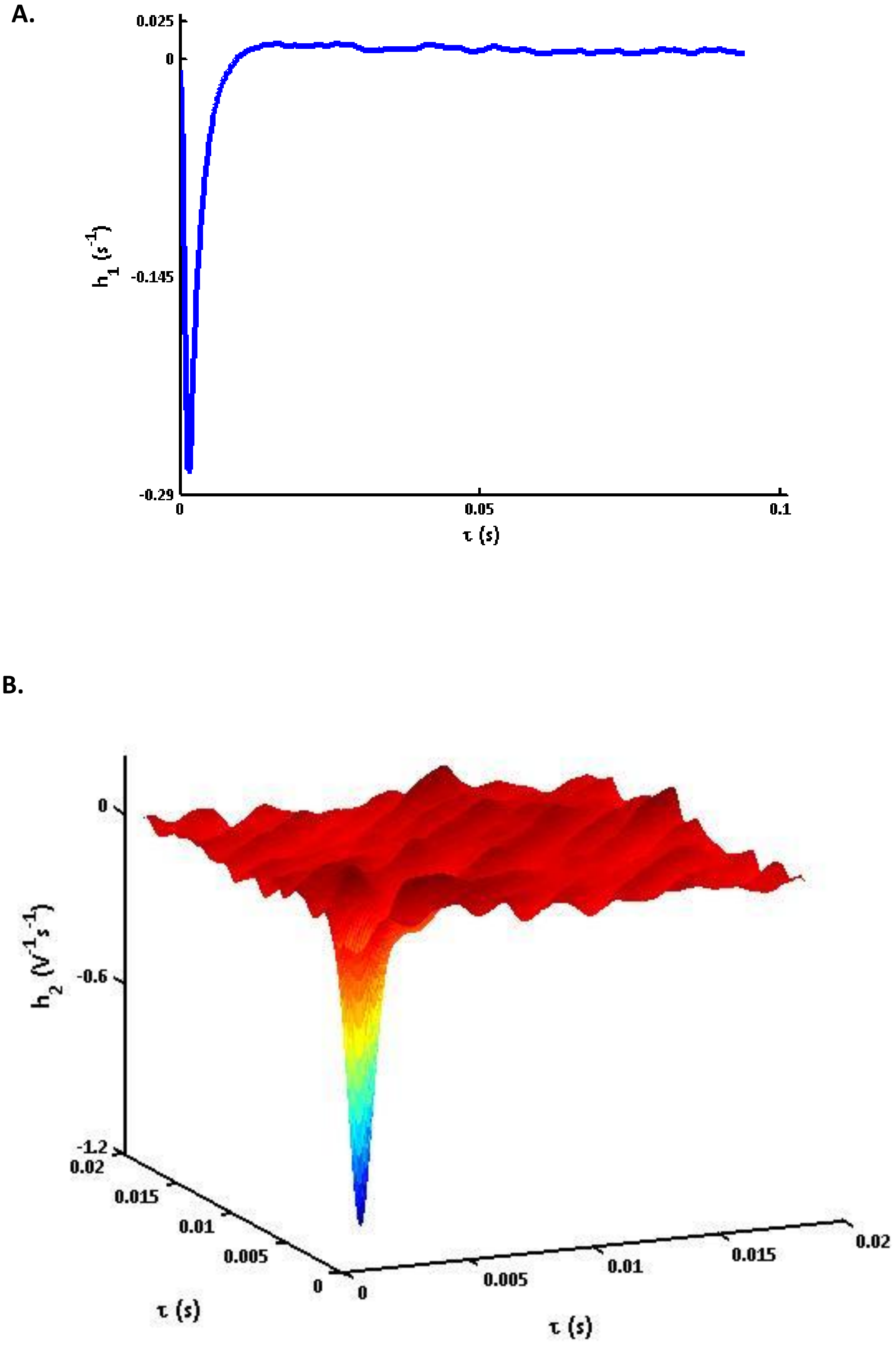

Figure 8. (A) First, and, (B) second order Wiener kernels computed from the input-output records corresponding to Gaussian white noise stimulus obtained from the neuron electrode junction.

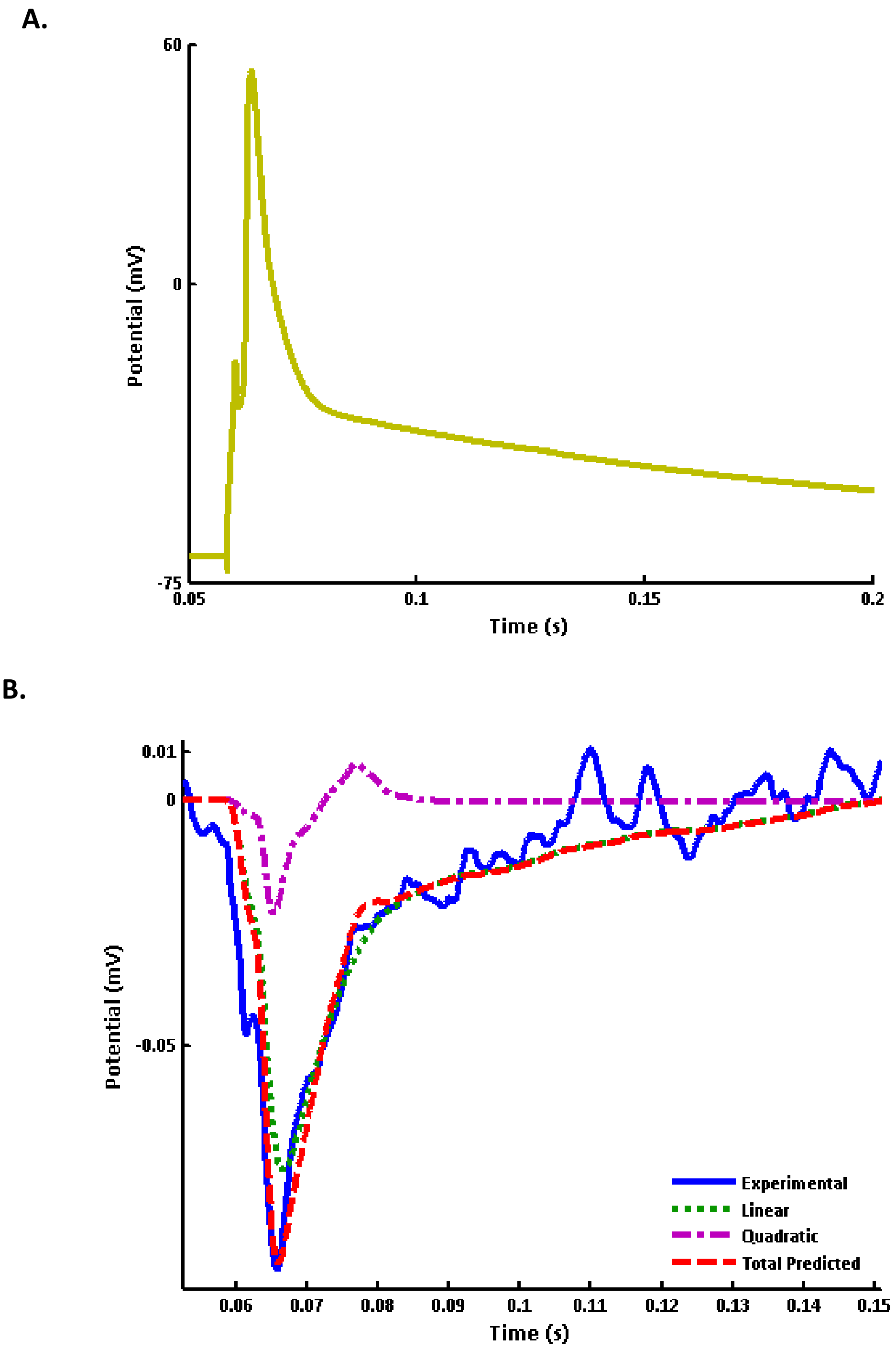

Figure 9. (A) Intracellular action potential as recorded from the neuron-electrode system shown in Figure 5, and, (B) Actual output as recorded on the extracellular microelectrode (solid line), linear predicted output from the first order kernel (dotted), quadratic predicted output from the second order kernel (dash-dot-dash) and the total predicted output obtained by summing the outputs obtained from the two Wiener kernels (dashed).

2.5. Discussion

Traditionally, as pointed out in the previous chapter, the neuron-electrode interface has been modeled as a passive linear equivalent circuit with a combination of resistances and capacitances representing the neuron-electrode cleft and the recording microelectrode [23-28]. The intracellular potentials generated through the use of Hodgkin-Huxley model or other similar models have then been employed as stimuli with the linear equivalent circuit (representing the interface) forming the input transforming system. In this chapter, we have presented results from a non-parametric Volterra-Wiener characterization for the composite neuron-electrode junction with the intracellular potentials forming the input; the recorded extracellular potentials on the microelectrode the output; and, the neuronal membrane and the neuron-electrode cleft the input transforming system. Results presented here show the presence of nonlinear dynamic processes occurring during the process of signal transduction across the neuron-electrode junction that contribute to the second order Wiener kernel. As a consequence it becomes important to revisit the assumptions pertaining to the passive linearity of the interface.

2.5.1. Possible hypotheses

The following two competing hypotheses can be advanced to explain the origins of the nonlinear contributions to the extracellular signal recorded on the microelectrode.

2.5.1.1. Linear interface

It can be seen that the second order nonlinear response shown in Figure 9 B is biphasic in nature with the initial negative going transient coinciding with the timing of the inward sodium current and the latter positive transient with the slow outward potassium current during the time course of the action potential. Based on this coincidence one could ascribe the nonlinear part of the extracellular response entirely to the active ionic currents flowing across the neuronal membrane allowing one to conveniently model the linear part of the response using an equivalent circuit model of the interface [43].

2.5.1.2. Nonlinear interface

On the other hand, based on an intuitive understanding of the physics of electrodiffusion governed by a system of coupled nonlinear Poisson-Nernst-Planck and the mass conservation or continuity equations together with the expected dielectric relaxation of biological macromolecules in the neuron-electrode cleft (thickness on the order of 20-110 nm [48]) in the presence of high electric fields generated during an action potential, it appears reasonable to expect and observe nonlinear effects in the process of signal transduction across the interface. It is notable in this regard that other researchers have also found it difficult to interpret extracellularly recorded signals based solely on the linear equivalent circuit modeling approach and have felt the need to take into account the electrodiffusion of ions in the neuron electrode cleft [49].

Whether the appearance of nonlinearity is due to the activity of ion channels in the neuronal membrane or due to the physics of electrodiffusion and dielectric relaxation or a combination thereof is difficult to say from the observations presented here and further careful experiments need to be designed to isolate the sources of nonlinearity. Understanding these phenomena taking place at the neuron-electrode interface during the process of signal transduction is key to correctly interpreting the extracellularly recorded potentials on the microelectrode and to ascertain their relationship to the corresponding intracellular potentials.

2.6. Conclusions

The complexity of the process of signal transduction across the interface precludes the possibility of using a direct physics based first principles approach to modeling the neuron-electrode interface. However, faced with such a predicament, the technique of Volterra-Wiener characterization circumvents, both, the difficulties inherent in the physics based modeling approach and the assumptions made in the formulation of equivalent circuit models. Non-parametric Volterra-Wiener modeling therefore offers a novel way to successfully characterize the neuron-electrode junction in a realistic fashion. The use of Volterra-Wiener characterization, thus, marks an important, albeit a small, step towards gaining an understanding of the processes governing the transformation of the intracellular potentials generated by the neuron into the signals recorded on the extracellular microelectrode.

CHAPTER-3: EQUIVALENT CIRCUIT MODELS FOR REPRESENTING EXTRACELLULAR RECORDINGS AT THE NEURON-ELECTRODE INTERFACE

3.1. Introduction

In Chapter 2, an estimation of a non-parametric Volterra-Wiener model of the neuron-electrode junction using experimentally obtained stimulus-response data records indicated the presence of second order nonlinear effects that occur during the process of signal transduction across the planar neuron-microelectrode interface. It was, however, not possible from the Volterra-Wiener model to conclusively prove whether these nonlinear contributions were exclusively from the neuron or from a combination of the dynamics of the neuron and the nonlinear ionic electrodiffusion and dielectric relaxation of the extracellular medium in the neuron-electrode cleft. If the former were to be true then linear equivalent circuit models of the interface would provide an appropriate representation of the signal transduction process at the neuroelectronic junction. However, in this regard, recently other researchers have also questioned the use of equivalent circuit models for simulating the cell-sensor interface based on arguments related to the physics of electrodiffusion of ions in the cleft between the electrically active cell and the sensor and a modulation of the surface potential on the sensor surface [50-52]. Although models based on a description of electrodiffusion of ions in the cell-biosensor interface have been advanced, to date there has been no systematic attempt to explore the limitations of linear equivalent circuit models for representing the cell-biosensor interface.

Non-parametric Volterra-Wiener models are useful to the extent that they offer an ‘unbiased’ and ‘data-true’ characterization of the system dynamics and can be employed to predict outputs for arbitrary inputs but they do not offer any additional insights into the inner workings of the system. However, they do offer plausible hypotheses regarding the underlying structure of the system dynamics which can then be tested further using parametric models. Therefore, to test if a passively linear interface employed in point or area contact equivalent circuit models is a valid representation of the system and to ascertain if there is indeed any contribution to the extracellular signals from the dynamics of the interfacial medium in the neuron-microelectrode cleft that cannot be modeled based purely on the theory of linear equivalent circuit models, a systematic study based on an optimization of the parameters of an equivalent circuit model for the neuron-microelectrode interface was undertaken. Additionally, results were compared and contrasted from the optimization of parameters of equivalent circuit models for a neuron simultaneously interfaced to an ‘on-cell’ patch electrode and the planar microelectrode (Figure 10 A and B) by fitting the simulated results to the extracellularly recorded signals obtained by a stimulation of the neuron through an intracellular patch electrode. It was believed that as a control system, the ‘on-cell’ patch model of the neuron-patch electrode interface having a gigaOhm seal with the neuronal membrane would allow for a direct measurement of the cell-generated membrane potentials and also serve as a limiting case for the neuron microelectrode interface (Figure 10 A and B). The ‘on-cell’ patch would have a smaller area of attachment on the neuronal membrane compared to the cell-electrode contact at the planar neuron-microelectrode interface, but would be better defined.

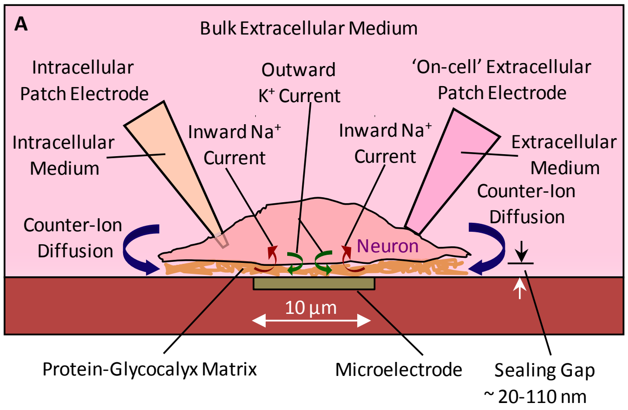
A
Bulk Extracellular Medium
Intracellular Patch Electrode
Outward K+ Current
'On-cell' Extracellular Patch Electrode
Intracellular Medium
Inward Na+ Current
Inward Na+ Current
Extracellular Medium
Counter-Ion Diffusion
Counter-Ion Diffusion
Neuron
10 µm
Protein-Glycocalyx Matrix
Microelectrode
Sealing Gap ~ 20-110 nm

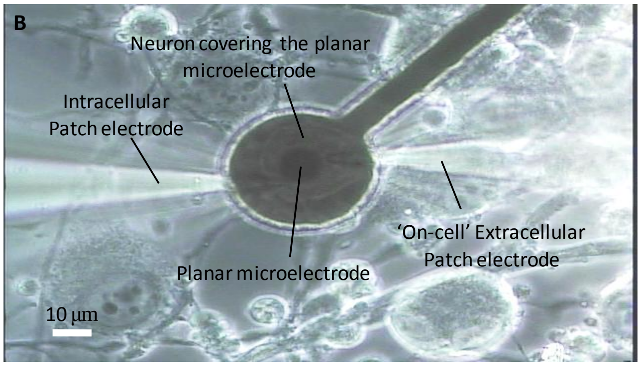
B
Neuron covering the planar microelectrode
Intracellular Patch electrode
'On-cell' Extracellular Patch electrode
Planar microelectrode
10 µm

Figure 10 (A) An illustration of the experimental arrangement for the electrophysiological characterization of the 'on-cell' neuron-patch electrode and neuron-microelectrode interfaces. (B) An image of a NG108-15 neuron covering a planar microelectrode on an MEA interfaced simultaneously to intracellular and 'on-cell' extracellular Ag/AgCl patch electrodes.

Also, at the extracellular neuron-patch electrode interface the cell membrane would be in direct contact with a large volume of the extracellular bath solution inside the patch electrode in sharp contrast to the small volume of the extracellular solution in the narrow (20-110 nm) neuron-microelectrode cleft. The two systems would also be different due to the presence of the porous protein-glycocalyx matrix and the extracellular matrix proteins deposited on the microelectrode due to a prolonged contact with the cell membrane. However, by studying the effect of these differences it was hoped to further understand this complicated system.

3.2. Materials and methods

Several different types of extracellular signal shapes recorded both with planar microelectrodes and field effect transistors have been reported in literature. On the basis of the recorded shapes the neuron-sensor junctions have broadly been classified into three major types: (a) capacitive, (b) ohmic and (c) anti-capacitive junctions characterized by a leading positive transient, direct proportionality to the intracellular signal and a leading negative transient respectively [28, 53-55]. Of these, the ohmic junction represents a strong coupling between the neuron and the sensor and its occurrence is the least common while most of the recorded extracellular signals fall under either the capacitive or the anti-capacitive category. The capacitive coupling has been interpreted on the basis of the linear junction conductance alone but the interpretation of the anti-capacitive coupling has required assumptions of a difference in the ion-channel distributions or a variance in their conductivity in the attached membrane compared to the free membrane [56]. However, there exists no conclusive evidence of either selective accumulation-depletion of ion-channels in the attached membrane or a difference in their conductance with respect to the free membrane [52]. Therefore, to test the hypothesis of the passive linearity of the neuron-electrode interface, in this paper we exclusively focused our attention on the extracellularly recorded signals that conformed to the 'linear' capacitive coupling of the neuron-electrode interface as previously reported in the literature [28, 53-55].

3.2.1. Cell culture and electrophysiological recording protocols

Briefly, NG108-15 neurons were cultured on top of substrate embedded microelectrode arrays and three-way electrophysiological recordings (Figure 10 A and B) were performed on them in voltage and current clamp modes. The culture of the NG108-15 neurons and extracellular and intracellular electrophysiological recordings from the neuron-electrode interfaces were carried out according to protocols and techniques described in chapter 2. Whole-cell patch clamp recordings were performed using an intracellular electrode on neurons covering the microelectrodes completely while a second patch electrode filled with the extracellular solution was employed to form a seal with the neuronal membrane without breaking in to the cell.

NG108-15 cells are a cross between mouse neuroblastoma and rat glioma cells that unlike neurons do not form synapses among themselves but at the same time retain fully functional neuron-like ion-channels. The non-synapsing feature of the NG108-15 cells makes them ideally suited for use as whole-cell biosensors in high-throughput drug screening and toxin detection wherein an undesirable component of independent network-like behavior of neurons can be avoided while retaining the sensitivity advantage of neurons.

3.2.2. Mathematical models

3.2.2.1. NG108-15 neurons

A Hodgkin-Huxley type mathematical model of NG108-15 cells, based on the thermodynamic rate constant approach developed previously [57-59], was employed to extract the ion-channel parameters for the sodium, calcium and potassium ion channels. The dynamic membrane potential V_m in the mathematical model for the NG108-15 neuron was computed using

$$C_m \frac{dV_m}{dt} = I_{inj} - I_{ionic} \tag{9}$$

where I_{inj} is the external current injected into the neuron through the intracellular patch electrode and C_m the membrane capacitance. The total ionic membrane current I_{ionic} and the leakage current I_L were described in terms of the membrane potential V_m as

$$I_{ionic} = I_{Na} + I_K + I_{Ca} + I_L \tag{10}$$

$$I_{Na} = g_{Na} m^3 h (V_m - V_{Na}) \tag{11}$$

$$I_K = g_K n^4 (V_m - V_K) \tag{12}$$

$$I_{Ca} = g_{Ca} e^3 (V_m - V_{Ca}) \tag{13}$$

$$I_L = g_L (V_m - V_L) \tag{14}$$

while the dynamics of the state variables for the ion-channels were given by

$$\frac{dm}{dt} = \frac{m_\infty - m}{\tau_m} \tag{15}$$

where g_{Na}, g_K, g_{Ca}, V_{Na}, V_K and V_{Ca} are maximum ion channel conductances followed by corresponding reversal potentials (sodium, potassium and calcium in that order); g_L and V_L are the leakage conductance and leakage reversal potentials respectively; m, h, n, and e are the state variables with m_∞, h_∞, n_∞, and e_∞ as their steady state values and the τ's their voltage dependent time constants. The maximum conductance g_L of the leakage current across the cell membrane was computed using

$$g_L = \frac{1}{R_m} - \frac{I_{2h}^{ionic} - I_{1h}^{ionic}}{V_{2h} - V_{1h}} \tag{16}$$

where I_{1h}^{ionic} and I_{2h}^{ionic} are the membrane ionic currents at the holding potentials V_{1h} and V_{2h} respectively and R_m is the experimentally obtained membrane resistance. Membrane holding potentials V_{1h} (-85 mV) and V_{2h} (-80 mV) were chosen such that there was no significant contribution from the opening of the voltage-gated sodium, potassium and calcium ion channels at these potentials i.e. the membrane was in a hyperpolarized state. The leakage reversal potential V_L was then computed using

$$V_L = \frac{I_{Na}^r + I_K^r + I_{Ca}^r}{g_L} + V^r \tag{17}$$

This made use of the fact that the net membrane current at the resting membrane potential V_m^r is zero. The superscript $'r'$ on the ion channel mediated currents represents the currents computed at the resting membrane potential. The voltage dependent steady state parameters and the time constants were computed using the general formulae

$$m_\infty = \frac{1}{1 + e^{-zF(V_m - V_{1/2})/RT}} \tag{18}$$

and

$$\tau_m = \frac{A}{e^{(zF\xi/RT)(V_m - V_{1/2})} \cosh\left(zF(V_m - V_{1/2})/2RT\right)} \tag{19}$$

where the fitting parameters were: z, related to the number of moving charges during the opening and closing of the ion channels; $V_{1/2}$, to the half activation/inactivation potential of the ion channel; A, related linearly to the activation or the inactivation time constant; and ξ, to the asymmetric position of the moving charge in the cell membrane. F, is the usual Faraday's constant. The experimentally obtained parameters used in the model were: R_m, the membrane resistance; V_m^r, the resting membrane potential; C_m, the membrane capacitance; and I_{inj}, the injected current.

3.2.2.2. 'On-cell' neuron patch-electrode interface

The neuron-patch electrode interface was modeled using a two compartment system as depicted in Figure 11 A. The physical significance of the equivalent circuit elements used in the model of the 'on-cell' neuron patch electrode interface was as follows: R_{ext}, the resistance of the extracellular medium between the free membrane of the neuron and the ground electrode; C_{fm}, the free membrane capacitance; R_{int}, the internal cytoplasmic resistance to ionic current flow as seen by the 'on-cell' extracellular patch electrode; C_{am}, the capacitance of the portion of neuronal membrane interfaced to the extracellular patch electrode; R_s, the seal resistance between the inside of the 'on-cell' patch electrode and the bulk extracellular medium; R_{sp}, the spreading resistance between the cell and the extracellular patch electrode; R_e and C_e, the resistance and the capacitance of the extracellular patch electrode respectively with C_e representing the capacitive coupling between the glass micropipette tip and the extracellular medium; and, R_A, the input impedance of the recording amplifier. The attached and free membrane capacitances, C_{fm} and C_{am}, being in parallel, are directly proportional to the fractional surface areas of the attached and free membranes respectively and were computed based on the experimentally determined values for the membrane capacitance C_m using equations (20) and (21)

$$C_{am} = a_j C_m \tag{20}$$

$$C_{fm} = (1 - a_j) C_m \tag{21}$$

where a_j is the fractional surface area of the attached membrane.

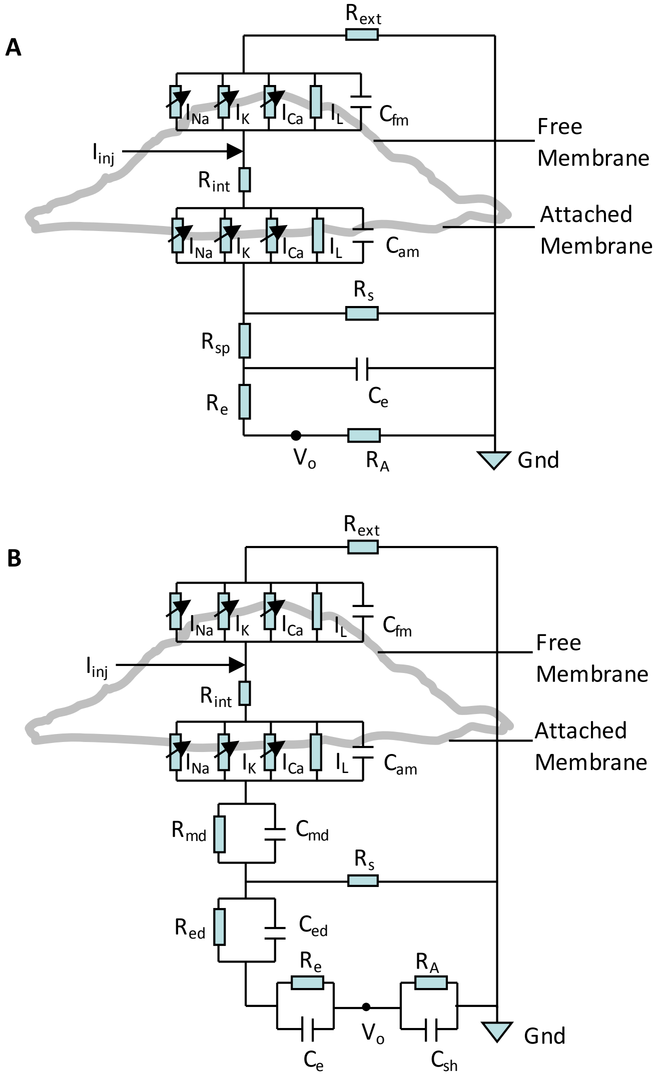
A
R_ext
I_Na
I_K
I_Ca
I_L
C_fm
Free Membrane
I_inj
R_int
Attached Membrane
I_Na
I_K
I_Ca
I_L
C_am
R_s
R_sp
C_e
R_e
V_o
R_A
Gnd
B
R_ext
I_Na
I_K
I_Ca
I_L
C_fm
Free Membrane
I_inj
R_int
Attached Membrane
I_Na
I_K
I_Ca
I_L
C_am
R_md
C_md
R_s
R_ed
C_ed
R_e
R_A
C_e
V_o
C_sh
Gnd

Figure 11. Schematics of the point contact equivalent circuit models for (A) the ‘on-cell’ neuron-patch electrode interface and (B) the neuron-microelectrode interface. V_o represents the extracellular output.

The extracellular potential recorded with the 'on-cell' patch electrode for the circuit model depicted in Figure 11 A was computed using Kirchoff's current and voltage law based set of time dependent linear first order ordinary differential equations that were coupled to the equations (15) for the Hodgkin-Huxley type linear thermodynamic model of the NG108-15 neuron.

3.2.2.3. Planar neuron-microelectrode interface

For modeling the neuron-microelectrode interface a more refined two compartment equivalent circuit model was employed (Figure 11 B) which included additional equivalent circuit elements to take into account the complexity arising from modeling the presence of EDL effects in the narrow 20-110 nm wide neuron-microelectrode cleft. The resistance and capacitance of the EDL associated with the protein-glycocalyx complex attached to the portion of the cell-membrane in contact with the microelectrode were modeled with circuit elements R_{md} and C_{md} respectively, while resistance R_{ed} and capacitance C_{ed} modeled the equivalent resistance and capacitance of the EDL associated with the extracellular matrix deposited on the microelectrode. Resistor R_e and capacitor C_e modeled the resistance and capacitance of the microelectrode and the parasitic shunt capacitance between the insulated connection leads (from the microelectrode to the amplifier) and the bulk electrolyte was modeled with the shunt capacitance C_{sh}. The sealing resistance R_s simulated the resistance to ionic current flow between the center of the neuron-microelectrode cleft and the bulk extracellular medium. The dynamics of the neuron-microelectrode interface for the equivalent circuit model shown in Figure 11 B were simulated using coupled differential equations for the linear interface combined with equations (15) that modeled the ion-channel kinetics of the NG108-15 neuron.

3.2.3. Optimization of the model parameters

3.2.3.1. NG108-15 neurons

Previously estimated average values of the ion-channel parameters for NG108-15 neurons were used as starting values for the ion-channel parameter fitting procedure [58]. The fitting procedure was customized using a graphical user interface. The parameters for the sodium, potassium and calcium channels were obtained by fitting the simulated ionic currents and membrane potentials to the experimentally recorded ion-channel mediated membrane currents and potentials obtained from the voltage and current clamp recordings of the neuron respectively. Initially, the sodium currents were fitted in the range -65 mV to -35 mV followed by a fitting of the potassium currents in the -15 mV to +15 mV range. After this a simultaneous fitting of the ion-channel parameters was carried out to obtain a first estimate of the parameters for the sodium, potassium and calcium channels. Further, to overcome the limitations of the parameter fitting procedure with regard to the uniqueness of the large number of fitted parameters and to obtain a quasi-unique set, a second optimization of the estimated ion channel parameters was performed by fitting the simulated action potentials to the experimental current clamp signals.

3.2.3.2. Neuron-electrode interface

Optimization of the equivalent circuit parameters for the neuron-electrode interface was carried out in two steps. In the first step, all circuit parameters, including the fractional surface area of the attached membrane but excluding the experimentally determined total membrane capacitance C_m, were optimized by fitting the simulated extracellular signals to the experimental sub-threshold stimulation records obtained from the neuron-electrode interfaces. It is accepted that sub-threshold stimulation of a hyper-polarized neuron is not accompanied by an opening of the voltage gated membrane ion-channels responsible for the generation of action potentials and as a result there is no corresponding contribution from ionic electrodiffusion to the extracellular signals recorded on the electrodes. A sub-threshold stimulation pulse leads to a depolarization of the neuronal membrane through intracellular current injection and a consequent electromigration of the ions under the influence of an electric field. In this regime, the membrane conductance stays ohmic and is characterized by an ohmic leakage current across the membrane. As the sub-threshold stimulation pulse is not accompanied by an opening of the voltage gated ion-channels it does not induce significant ionic concentration gradients between the neuron-electrode interface and the bulk extracellular medium. In the case of the supra-threshold stimulation of the neuron, however, the opening of the voltage gated ion-channels leads to a significant difference in the ionic concentrations at the neuron-electrode interface relative to the ionic concentrations in the bulk extracellular medium. Therefore, the second step in the optimization of the equivalent circuit parameters for the neuron-electrode interface involved fixing the optimized invariant parameters obtained in step one and a re-evaluation of the remaining parameters of the model for the neuron-electrode interface by a fitting of the simulated signals to the experimental signals obtained from the supra-threshold stimulation of the neuron. This, as hypothesized, would enable quantification of the changes in the equivalent circuit parameters affected by the physics of ionic electrodiffusion upon opening of the voltage-gated ion-channels as one transitioned from the sub- to the supra-threshold regime of neuronal stimulation.

3.2.4. Numerical methods

The coupled ordinary differential equations for the linear thermodynamic model of the neuron and the equivalent circuit representations of the neuron-electrode interfaces were numerically integrated in MATLAB (The MathWorks, Natick, MA) using its in-built differential equation solver *ode15s* for the solution of a set of stiff equations. The relative and absolute error tolerances of MATLAB's *ode15s* solver were set to 10^{-4} and 10^{-7} respectively.

An in-built MATLAB optimization routine *fmincon* (employed for computing a constrained minimum of a function dependent on several variables within specified bounds and/or linear or nonlinear constraints) was first used for the estimation of the ion-channel parameters for the NG108-15 neurons and subsequently for the estimation of the equivalent circuit parameters for the neuron-electrode interfaces by fitting the simulated signals to the experimentally recorded signals. All parameter optimizations were carried out by minimizing the sum of squared residuals as shown in equation (22)

$$ssr = \sum_{n} (S(t_n) - R(t_n))^2 \tag{22}$$

where $S(t_n)$ is the simulated data at time t_n and $R(t_n)$ is the recorded value at that instant of time. However, for a comparison of the quality of fitting of the simulated signals to the experimental signals of differing magnitudes recorded from the three electrodes, the normalized sum of squared residual ($nssr$) values are reported here.

The 'algorithm' option in MATLAB for the optimization routine *fmincon* was set to the sequential quadratic programming (SQP), quasi-Newton line-search algorithm for all optimizations. An optimization termination tolerance of 10^{-8} for the minimizing function and the parameters being optimized was employed while the tolerance on constraint violation for the optimized parameters was fixed at 10^{-12}. If a constraint violation on the upper or lower bounds for any parameter(s) was reported at the termination of the optimization routine then the limits were appropriately adjusted and the optimization procedure repeated for that case. The lower and upper bounds of the equivalent circuit model parameters were selected based on known typical values of the parameters from experiments and published literature [26, 60, 61]. The amplifier input impedance R_A was fixed at $12\ G\Omega$ for all simulations.

3.3. Results

3.3.1. Ion-channel parameters for the NG-108-15 neurons

The results from the ion-channel parameter fitting procedure for the voltage and current clamp recordings are shown for a set of representative NG108-15 neurons, indicated by Cell 1 (Figure 12, A1 and A2) and Cell 2 (Figure 12, B1 and B2), selected from a group of neuron-electrode interfaces examined experimentally $n = 10$. For the voltage clamp recordings an excellent fit to the experimental results was obtained for the potassium channel mediated ionic currents (Figure 12, A1 and B1 outward currents to the right of the dashed vertical black lines) but the fitted traces overestimated the sodium channel currents (Figure 12, A1 and B1*,* inward currents to the left of the dashed vertical black lines) due to space-clamping effects generated as a result of the large size of the NG108-15 neurons.

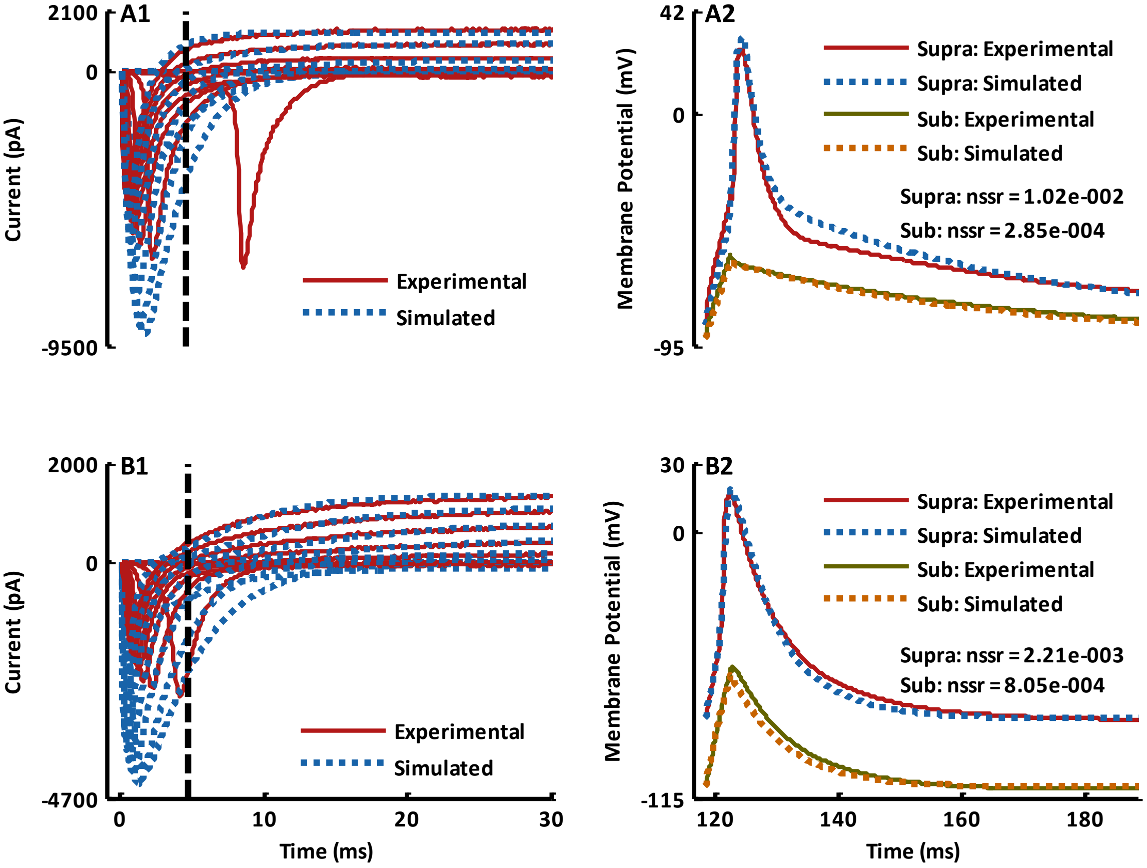

Figure 12. A comparison of the simulated results with the experimentally recorded intracellular signals after an optimization of the ion-channel parameters. (A1 and B1) Experimental voltage clamp signals recorded using 10mV potential steps starting from a holding potential of -85mV (solid line) and their corresponding simulated voltage clamp signals (dotted line) using optimized ion-channel parameters for Cell 1 and Cell 2 respectively (See Table I, A and B). Currents to the left of the dashed black vertical lines represent inward sodium currents while to the right of the lines outward potassium currents are shown. (A2 and B2) Experimental sub- (solid line) and supra-threshold (solid line) intracellularly recorded current clamp signals from Cell 1 (Sub-threshold current injection, $I_{inj} = 560\,pA$ and supra-threshold current injection, $I_{inj} = 760\,pA$, $\Delta t = 4\,ms$; membrane capacitance $C_m = 70pF$; and, resting membrane potential $V_m^r = -54.6\,mV$) and Cell 2 (Sub- and supra-threshold current injection, $I_{inj} = 1180\,pA$, $\Delta t = 4\,ms$; membrane capacitance $C_m = 80pF$; and, resting membrane potential $V_m^r = -40.0\,mV$) respectively. Simulated sub- (dotted line) and supra- threshold (dotted line) intracellular current clamp signals for Cell 1 and Cell 2 using optimized ion-channel parameters shown in Table I, A and B.

Table 1. Optimized ion channel parameters for (A) Cell 1 and (B) Cell 2 obtained by a fitting of the simulated current and voltage clamp intracellular signals to the experimentally recorded signals[a].

A.

			Activation				Inactivation			
Channel	g	V_{rev}	z	$V_{1/2}$	ξ	A	z	$V_{1/2}$	ξ	A
Sodium	157.67	120.0	7.10	-47.38	-0.43	0.42	-19.09	-63.72	0.46	2.79
Potassium	16.05	-80.0	3.16	-14.43	0.13	8.65	-	-	-	-
Calcium	3.82	32.0	2.59	-5.07	-0.59	0.91	-	-	-	-
Leakage	1.61	-54.6	-	-	-	-	-	-	-	-

B.

			Activation				Inactivation			
Channel	g	V_{rev}	z	$V_{1/2}$	ξ	A	z	$V_{1/2}$	ξ	A
Sodium	51.56	120.0	7.48	-56.00	-0.38	0.42	-20.25	-58.65	0.46	2.97
Potassium	16.02	-80.0	1.62	-42.64	0.03	14.28	-	-	-	-
Calcium	3.82	32.0	2.59	-5.11	-0.59	0.91	-	-	-	-
Leakage	9.09	-34.0	-	-	-	-	-	-	-	-

[a] The ion-channel conductances and the electric potentials are reported in nano-Siemens and mV respectively.

Table 2. Optimized parameters of the point contact equivalent circuit model for the ‘on-cell’ neuron-patch electrode interfaces for (A) Cell 1 and (B) Cell 2[b].

A.

	a_j	C_e	R_{ext}	R_{int}	R_s	R_{sp}	R_{sp}
Sub	0.62	6.00	4.25e-5	5.20e-3	1.56e-1	5.00e-3	6.25e-3
Sup	O	O	2.40e-6	1.65	5.39e-1	6.18e-2	O

B.

	a_j	C_e	R_{ext}	R_{int}	R_s	R_{sp}	R_{sp}
Sub	0.89	4.71e-1	1.28e-4	1.20e-1	6.75e-2	1.85e-1	3.31e-2
Sup	O	O	3.86e-4	1.17	1.28e-1	5.18e-3	O

[b] The symbol ‘O’ stands for the point contact equivalent circuit model parameters fixed at values obtained from sub-threshold optimization of the model parameters for the neuron-electrode interfaces. The fractional surface area of the attached membrane is reported as a percentage of the total membrane surface area; all resistances are in gigaohms $G\Omega$ and the capacitances are in picoFarads (pF) . ‘*Sub*’ and ‘*Sup*’ refer to sub- and supra-threshold stimulations respectively.

An excellent fit to the experimentally recorded signals was obtained for the current clamp recordings for both the sub- and supra-threshold stimulation cases (Figure 12, A2 and B2). Table I, A and B, shows the optimized ion-channel parameter values for the recording data from the NG108-15 neurons reported here. The estimated ion-channel parameters were then fixed and employed further in the determination of the parameters of the equivalent circuit models for the neuron-electrode interface. Also, in all subsequent simulations of the two compartment equivalent circuit models of the neuron-electrode interface, a uniform spatial distribution of the different types of ion-channels in the attached and the free neuronal membranes was assumed.

3.3.2. 'On-cell' neuron patch electrode interface

For the 'on-cell' neuron patch-electrode interface (Figure 11 A) the equivalent circuit parameters optimized using the extracellular signals recorded from sub-threshold stimulation of NG108-15 neurons included the internal cytoplasmic resistance R_{int}, the external resistance R_{ext}, the spreading resistance R_{sp}, the sealing resistance R_s, the patch electrode resistance R_e and capacitance C_e and a_j, the fractional area of the cell membrane in contact with the extracellular patch electrode. The 'on-cell' extracellular signals employed in the parameter optimization corresponded to the sub-threshold intracellular potentials shown in Figure 12 A2 (Cell 1) and B2 (Cell 2). An excellent fit was obtained for the extracellular signals recorded on the patch electrodes corresponding to the sub-threshold stimulation of the neuron in the case of both the NG108-15 neurons employed in the study (Figure 13, A1 and B1). Table II, A and B indicate the sub-threshold values of the optimized parameters for Cell 1 and Cell 2.

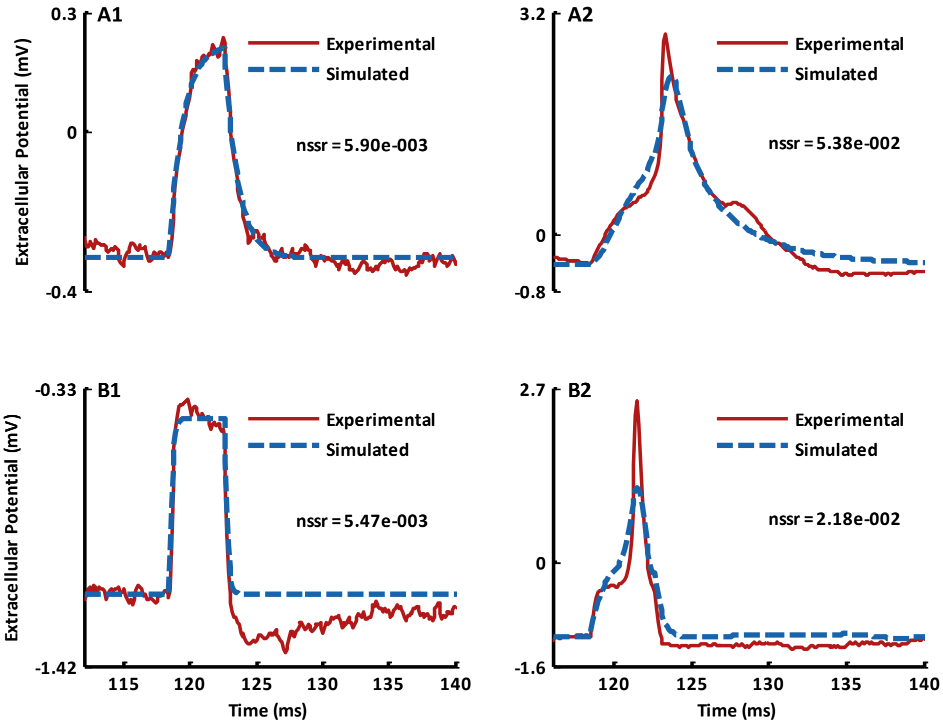

Figure 13. A comparison of the simulated and the experimental results for the extracellular signals recorded from the ‘on-cell’ neuron-patch electrode interfaces for Cell 1 and Cell 2 after optimization of the point contact equivalent circuit model (Figure 11 A) parameters. (A1 and B1) Sub-threshold stimulation for Cell 1 and Cell 2 respectively. (A2 and B2) Supra-threshold stimulation for Cell 1 and Cell 2 respectively. (See Table II, A and B, for values of optimized equivalent circuit parameters.)

Next, the optimized values of the invariant parameters - the ‘on-cell’ patch-electrode resistance R_e, capacitance C_e and the fractional area of contact between the cell membrane and the ‘on-cell’ patch electrode a_j obtained from the optimization of the sub-threshold signals were fixed while the rest of the parameters of the equivalent circuit model were then re-evaluated by fitting the simulated supra-threshold extracellular signals (corresponding to supra-threshold intracellular action potentials shown in Figure 12, A2 and B2) to experimental data from the neuron-electrode interface. For the two cells being reported here, the quality of the fitting of the simulated extracellular signal in the supra-threshold case to the corresponding experimentally recorded signal, although reasonably good, was not comparable to that obtained for the sub-threshold case and the optimized simulation results were observed to underestimate the amplitude of the extracellular signal when compared to the experimentally recorded signals as shown in Figure 13, A2 and B2. In the two NG108-15 neuron patch electrode interfaces considered it was observed that the internal cytoplasmic resistance, R_{int}, and the seal resistance, R_s (Table II, A and B) both increased in transitioning from the sub- to the supra-threshold stimulation of NG108-15 neurons indicating a change in these circuit parameters while no clear trend was discernible for the spreading resistance, R_{sp}, and the external resistance, R_{ext}. This increase in the values of the internal cytoplasmic resistance, R_{int}, (as seen by the 'on-cell' patch electrode) and the seal resistance, R_s, in the supra-threshold case pointed to the presence of diffusion dominated ionic transport across the seal resistance formed by the 'on-cell' patch electrode with the neuronal membrane. Also, the high values of the seal resistance, R_s, $> 1\ G\Omega$ obtained through the optimization procedure in the supra-threshold stimulation were consistent with the formation of a gigaseal for the extracellular patch electrodes as normally observed during conventional patch clamp electrophysiology.

Further, the impact of ionic electrodiffusion on the individual values of the equivalent circuit parameters employed for the supra-threshold optimization was systematically investigated by selectively fixing the equivalent circuit parameters at their sub-threshold values and optimizing the rest of the parameters to compare the normalized sum of squared residuals obtained for Cell 1 and Cell 2 (Table III, figures not shown here). It was determined that a selective elimination of the sealing resistance, R_s, and the internal cytoplasmic resistance, R_{int}, from the optimization procedure resulted in the highest normalized sum of squared residuals $nssr$ (in that order) indicating that these two resistances were the most affected as a result of the ionic electrodiffusion induced by an opening of the voltage gated ion-channels in the supra-threshold regime of neuronal stimulation.

Table 3. nssr values for fitting of the simulated supra-threshold signal to experimental recordings after selective fixation of equivalent circuit parameter values at the sub-threshold level for the 'on-cell' patch electrode

Circuit element	R_s	R_{int}	R_{ext}	R_{sp}
Cell 1	4.92e-1	1.64e-1	5.39e-2	5.82e-2
Cell 2	6.89e-2	4.25e-2	2.35e-2	2.43e-2

It must be mentioned here that diffusion, within the framework of the point-contact equivalent circuit models, can only be simulated using a frequency dependent Warburg impedance [62] and thus, although the cytoplasmic internal resistance, R_{int}, and the seal resistance, R_s, did not simulate the Warburg impedance in this case, an increase in their values indicated the presence of ion transport mediated primarily by diffusion. Unlike linear impedance spectroscopy analyses, in this study, we employ a time domain composite model of the neuron-electrode interface that precludes the use of frequency dependent equivalent circuit elements for simulating interface dynamics.

3.3.3. Planar neuron-microelectrode interface

In the sub-threshold stimulation regime, capacitive type responses observed in the planar neuron-microelectrode interface for Cell 1 were analyzed. The equivalent circuit parameters of the neuron-microelectrode interface (Figure 11 B) included in the optimization for the sub-threshold stimulation were: resistor R_{md} and capacitor C_{md}, modeling the EDL associated with the protein-glycocalyx complex attached to the cell membrane, EDL resistance R_{ed} and capacitance C_{ed}, associated with the microelectrode, resistance R_e and capacitance C_e of the microelectrode, the parasitic shunt capacitance C_{sh}, seal resistance R_s and the fractional area of the attached membrane in contact with the microelectrode a_j. After an optimization of the equivalent circuit model parameters a reasonably good fit to the noisy extracellular signal corresponding to the sub-threshold stimulation of the neuron was obtained (Figure 14 A and Table IV). The related intracellular sub-threshold potential for the optimized extracellular signal is shown in Figure 12 A2.

Again, as in the case of the 'on-cell' patch electrode interface, invariant parameters – the shunt capacitance C_{sh}, the microelectrode resistance R_e and capacitance C_e, and the area of the attached membrane in contact with the microelectrode a_j, obtained from the sub-threshold optimization of the model parameters for the neuron-microelectrode interface, were fixed. The fitting of the simulated extracellular signals for the supra-threshold stimulation of the cell was performed by optimizing the values of the rest of the circuit elements in the equivalent circuit model of the neuron-microelectrode interface. Figure 14 B shows a good fit of the simulated signal to the experimental signal recorded through the microelectrode (See Figure 12 A2 for the corresponding supra-threshold intracellular potential). In the case of the neuron-microelectrode interface, as also for the 'on-cell' neuron-patch electrode interface, the optimized signals underestimated the amplitude of the extracellular signals compared to the experimentally recorded signals from the planar microelectrode. But, unlike the neuron-patch electrode interface, R_s decreased in transitioning from the sub- to the supra-threshold regime of neural stimulation. A decrease in R_s in transitioning from the sub- to the supra-threshold stimulation was consistent with the enhanced conductivity of the overlapping EDLs in the neuron-microelectrode cleft region as a consequence of the increased ionic concentrations caused by an opening of the ion-channels during the supra-threshold stimulation of the neuron. A similar enhancement in the conductivity of the cell-sensor junction for HEK 293 cells interfaced to field effect transistors was also reported by Brittinger et al [50].

A further investigation of the impact of the change in circuit parameters due to ionic electrodiffusion on the fitting of the supra-threshold simulated signals to the experimental extracellular recordings was done by selectively fixing the circuit parameters at their sub-threshold values and optimizing the rest of the parameters to study its effect on the normalized sum of squared residuals. It was observed that selective fixation at sub-threshold values of all the parameters under consideration gave comparable $nssr$ values ($nssr_{avg} = (4.48 \pm 0.03) \times 10^{-1}$) except in the case of the seal resistance, $R_s(nssr = 4.63 \times 10^{-1})$, and external resistance, $R_{ext}(nssr = 5.16 \times 10^{-1})$, where it was noticeably higher than the rest. In the case of R_s, the increase in $nssr$ value upon selective elimination was along expected lines for the reasons discussed in the preceding paragraph while for R_{ext} it appeared that the optimization of the sub-threshold extracellular signal overestimated the value for the external resistance resulting in a high normalized sum of squared residuals. However, as R_{ext} must not change between the 'on-cell' patch-electrode and the neuron-microelectrode interfaces (being a property of the bulk extracellular solution), the value of the external resistance ($R_{ext} = 2.53 \times 10^{-5}\ G\Omega$, Table IV) obtained from the supra-threshold optimization for the planar neuron-microelectrode interface compared well with the average value ($R_{ext}^{avg} = 2.24 \times 10^{-5}\ G\Omega$) obtained from an optimization of the equivalent circuit parameters for the corresponding 'on-cell' neuron-patch electrode interface (Table II *A*).

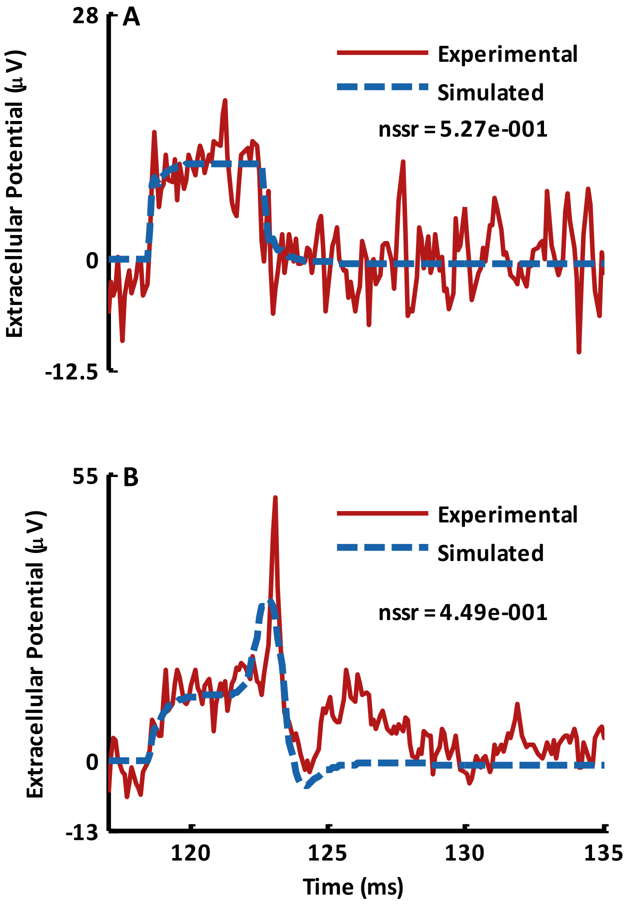

Figure 14. A comparison of the simulated and the experimental extracellular signals recorded from the neuron-microelectrode interface corresponding to the stimulation of Cell 1 (Figure 12 A2) after optimization of the point contact equivalent circuit model (Figure 11 B) parameters. (A) Sub-threshold stimulation and (B) Supra-threshold stimulation. (See Table IV for the corresponding values of the equivalent circuit parameters.)

Table 4. Optimized parameters of the point contact equivalent circuit model of the neuron-microelectrode interface for Cell 1[b].

	a_j	C_{md}	C_{ed}	C_e	C_{sh}	R_{ext}	R_{int}	R_{md}	R_s	R_{ed}	R_e
Sub	12.6	3.39	2.32e-1	5.00e+3	5.80e-3	4.91e-3	3.14e-2	2.82e-2	1.60e-4	4.44e-3	2.71e-4
Sup	O	3.37	2.22e-1	O	O	2.53e-5	2.95e-2	3.08e-2	1.38e-4	3.57e-3	O

[b] The symbol 'O' stands for the point contact equivalent circuit model parameters fixed at values obtained from sub-threshold optimization of the model parameters for the neuron-electrode interfaces. The fractional surface area of the attached membrane is reported as a percentage of the total membrane surface area; all resistances are in gigaohms $(G\Omega)$ and the capacitances are in picoFarads (pF). '*Sub*' and '*Sup*' refer to sub- and supra-threshold stimulations respectively.

3.4. Discussion

Based on the optimization analysis presented here, it was observed that for the 'on-cell' neuron patch electrode and the neuron-microelectrode interfaces the simulated post-optimization extracellular signals for the supra-threshold stimulations consistently underestimated the amplitude of the extracellular signal compared to the experimentally recorded signals. Since the current that flows through a microelectrode is negligible because of the high input impedance of the extracellular recording amplifier, a comparison can also be made with studies employing electrogenic cells interfaced to field effect devices that have comparable current flowing through the gate oxide. Earlier studies, by Wrobel et al and Brittinger et al [50, 52], that used field effect transistors had also reported similar observations related to point contact equivalent circuit models of the cell-biosensor interface. Both studies attributed the underestimation of the amplitude of the simulated extracellular signal to the mechanism of ion-binding to the gate-oxide of the field effect transistor and concluded that diffusion or electrodiffusion alone could not explain the amplitude of the experimentally recorded extracellular signals.

Wrobel et al employed the Nernst-Planck equation reduced to a pure diffusion equation under assumptions of electroneutrality and thin EDLs to simulate the ion-accumulation in the cleft region which was then combined with the ion-sensitivity of the field effect transistor to reproduce the experimental signals by a fitting of the radius, R, of the attached membrane and the cleft height, h. Brittinger et al modeled electrodiffusion in the interfacial cleft by considering the Nernst potential arising from the ionic concentration difference between the bulk extracellular medium and the interfacial medium. But they could account for the total signal recorded on the transistor only after a superposition of the experimentally determined surface potential changes associated with the Gouy-Chapman-Grahame diffuse EDL on the silanized gate-oxide (arising due to a competitive binding of sodium and potassium ions) and the potential difference generated in the cleft region due to electrodiffusion of ions.

It is worth noting here that, despite the Debye length being much smaller than the width or height of the cleft (~ 20-110 nm), at the given ionic concentrations in the extracellular medium the electric double layer actually extends across the entire interface to the sensor surface due to the presence of fixed charges associated with the porous-protein glycocalyx matrix responsible for cellular adhesion on the sensor surface. The presence of overlapping EDLs in the cell-sensor interfacial cleft therefore renders the assumption of electroneutrality in the interfacial cleft incorrect. Also, the region within the overlapping EDLs is characterized by a nonlinear dependence of the electric potential on the ionic concentration profile accompanied by a presence of high electric fields. These studies thus indirectly pointed to the presence of nonlinear EDL effects in the process of signal transduction across the volume of the thin cell-sensor interfacial cleft.

Both these studies, however, considered a simplified system of recombinant K^+ channels expressed in HEK 293 cells interfaced to the FETs and did not explicitly simulate the gating kinetics of the ion-channels coupled to their model for the cell-biosensor interface. In contrast, the coupled dynamics of the neuron and the linear equivalent circuit model for the interface were explicitly simulated in the study presented here. Additionally, in our model for the NG108-

15 neuron we estimated gating parameters of the ion-channel kinetics for sodium, potassium and calcium channels from the experimental current and voltage clamp recordings that realistically and uniquely accounted for the dynamics of the cells included in our study.

In the previous chapter, an experimental characterization of the neuron-microelectrode junction by an intracellular stimulation of the neuroelectronic interface with band-limited Gaussian white noise spanning the entire natural frequency and amplitude range of action potentials was presented. This approach of non-parametric 'data-true' nonlinear dynamic characterization of the neuroelectronic junction using Volterra-Wiener modeling helped take into account all possible linear and second order nonlinear physicochemical processes, including ionic electrodiffusion, occurring at the neuron-microelectrode interface during the process of signal transduction. Further, these results indicated that the linear part of the predicted output from the Volterra-Wiener model underestimated the extracellular signal but a summation of the linear and the nonlinear outputs accurately predicted the amplitude and shape of the experimentally recorded signal from the planar microelectrode.

It is notable that Buitenweg et al had also observed nonlinear components in the extracellular potentials recorded in their stimulation experiments with the neuron-electrode interface which could not be attributed entirely to the active neuronal contributions [43]. Their approach had focused on isolating the nonlinear component of the experimentally recorded response by a subtraction of the linear component from the total extracellular signal. For this purpose, the linear component of the extracellular response was simulated by employing an impedance model of the interface estimated earlier using linear impedance spectroscopy.

However, they had not isolated the neuronal contribution from the interfacial contribution in the total nonlinear response detected in the extracellular signal. The results presented here, go a step further and systematically isolate the neuronal contribution to the nonlinearity in the extracellular response recorded through the microelectrodes using a prior independent estimation of the neuronal ion-channel parameters unique to the neuron-electrode interface under study.

3.5. Conclusions

In this chapter, concurrent electrophysiological recordings from a single neuron simultaneously interfaced to three distinct electrode configurations (intracellular, 'on-cell' patch and planar microelectrode) allowed novel insights into the mechanism of signal transduction at the neuron-electrode interface. Through an advanced optimization based analysis of the extracellular signals, results presented here clearly established the role of ionic electrodiffusion in the process of signal transduction across the neuron-electrode interface and identified the parameters of the point contact equivalent circuit models most affected. These results, for the first time conclusively demonstrated that the mechanism of signal transduction across the neuron-electrode interface was nonlinear. Further, within the framework of a passively linear point or area contact equivalent circuit model of the neuron-electrode interface, it is therefore not possible to simulate and recover the correct amplitude and shape of the experimentally recorded extracellular outputs from supra-threshold stimulation of the neuron-electrode interfaces. This is especially significant because these models are now being actively extended to neural interfaces with nanoelectronic devices characterized, presumably, by still higher electric fields and the consequent nonlinear dynamics of the interfacial medium [63-65].

Engineering of neuroelectronic interfaces using surface-chemical modification of sensor surface, improved design or novel materials for device fabrication requires an understanding of the mechanism of signal transduction with its accompanying physicochemical changes at the cell-sensor interface and thus necessitates a further development of models based on the nonlinear physics of electrodiffusion of ions or unconventional techniques like the 'data-true' Volterra-Wiener characterization. However, equivalent circuit models with their simplicity of concept and ease of implementation will continue to be useful tools for the study and characterization of cell-sensor interfaces for applications in high-throughput drug screening and toxin detection, biological computation and neuroprosthetic devices.

CHAPTER-4: THEORETICAL FRAMEWORK FOR EXTRACTION OF INTERFACE PARAMETERS USING NONLINEAR IMPEDANCE SPECTROSCOPY

4.1. Introduction

Impedance spectroscopy or I-V characterization is a technique employed for the characterization of electrical properties of bulk materials or their interfaces with conducting electrodes with the aim of investigating the dynamics of bound or mobile charges present in them. Conventional linear impedance spectroscopy involves stimulating a system with small amplitude ac voltages superposed on a dc bias that scan a frequency range to generate an impedance spectrum [66, 67]. The total current (a sum of conduction and polarization currents) flowing through the material in between the two conducting electrodes forms the system response. The ratio of the stimulus potential to the response current gives the frequency dependent impedance spectrum or the 'data-true' transfer function of the system. This transfer function is analyzed further by comparing results from a plausible physical model of the system or, more commonly, by fitting the impedance spectrum to an equivalent circuit representation of the system dynamics using complex nonlinear least squares fitting. The complex dielectric permittivity for the material between the electrodes is computed using the relation $\varepsilon(\omega) = \varepsilon'(\omega) - j\varepsilon''(\omega) = 1/(j\omega C_c Z(\omega))$ where ω is the frequency of the applied ac signal, $C_c = \varepsilon_0 A/d$ is the capacitance of the measurement cell with electrode area A and separation d, and ε' and ε'' are the real and imaginary parts of the complex permittivity [66].

4.1.1. Impedance spectroscopy – Linear Vs Nonlinear

An accepted definition of impedance ($Z = V/I$) as a concept is valid only for linear systems wherein the output response of the system is exactly at the frequency of the input stimulus. For nonlinear systems, there is no such accepted definition of impedance and I-V characterization is loosely referred to here in this chapter as nonlinear impedance spectroscopy. Linear systems follow the principle of superposition, i.e. if $x_i(t_i)$ are the input stimuli applied at differing times t_i, a_i their amplitude and $y_i(t_i)$ their respective system responses then for a superposed input stimuli comprising all of $x_i(t_i)$, the system output can be written as a summation of the individual outputs in the form given below [41]

$$y\left(\sum_i a_i x_i(t_i)\right) = \sum_i a_i y_i(t_i) \tag{23}$$

The same, however, is not true of a nonlinear system in general. As such, faced with a nonlinear system the only recourse, therefore, is to characterize the system by studying its harmonic response to each individual input sinusoid. This approach to I-V characterization of a nonlinear system does not offer any information about system response with regard to the interaction of individual sinusoids with each other when presented to the system as superposed input stimuli. Also, therefore there currently exists no straight forward way to efficiently estimate the nonlinear material parameters of the system like its complex dielectric permittivity and conductivity that would influence its electrical behavior.

4.1.2. Neuron-microelectrode interface

Chapters 2 and 3 showed that the process of signal transduction at the neuron-microelectrode interface is nonlinear. Computation of material properties of the interfacial medium using impedance spectroscopy requires peering into the underlying system dynamics in contrast with the black-box approach to computation of the Wiener kernels using bandlimited Gaussian white noise in Chapter 2. Is it possible therefore to leverage non-parametric Volterra-Wiener modeling to estimate the material properties of the interfacial medium in the neuron-electrode cleft? The fact that the computation of the material parameters like dielectric permittivity and conductivity for a linear system can be accomplished directly using the ‘data-true’ impedance spectrum as pointed out in the introduction above offers hope. Computation of the material parameters itself does not require any assumption of an underlying structure for the system or a parametric representation of its dynamics in the form of a linear equivalent circuit model. Therefore, one can employ the mathematical machinery of Volterra-Wiener modeling for an estimation of the nonlinear dielectric permittivity and conductivity tensors.

Lee-Schetzen technique of cross-correlation [45], described in chapter 2, exploits the exclusive existence of even order moments of a specialized input stimulus, which is bandlimited Gaussian white noise, for the computation of Wiener kernels. Additionally, the use of bandlimited Gaussian white noise as a stimulus for computing material properties of a nonlinear system through impedance spectroscopy offers certain distinct advantages over the use of sinusoidal stimulus. Bandlimited Gaussian white noise by virtue of its flat power spectral density and a random Gaussian distribution of amplitudes spanning the entire frequency and amplitude range of system operation completely characterizes the nonlinear interactions of different frequencies as opposed to the prevalent practice of characterizing the system nonlinearity with a single sinusoid input and analyzing its harmonic response in the output signal. Therefore, employing the same experimental configuration as is used in linear impedance spectroscopy but replacing the sinusoid input with a bandlimited Gaussian white noise stimulus (as shown in Figure 15), this chapter outlines a theoretical framework based on Volterra-Wiener modeling for the estimation of the nonlinear dielectric permittivity and conductivity of the interfacial medium present in the cleft of the neuroelectronic junction.

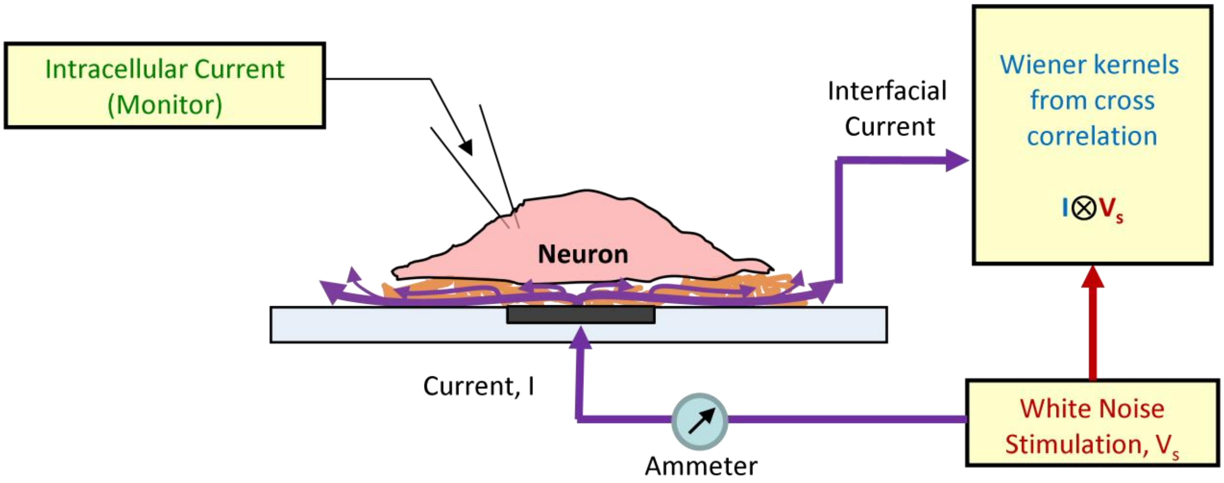

Intracellular Current (Monitor)
Interfacial Current
Wiener kernels from cross correlation
I⊗V$_s$
Neuron
Current, I
Ammeter
White Noise Stimulation, V$_s$

Figure 15. A schematic of the experimental arrangement for the extraction of nonlinear dielectric permittivity and conductivity of the interfacial medium using impedance spectroscopy based on Volterra-Wiener modeling. An intracellular current monitor is employed through use of patch-clamp electrophysiology to ensure that all of output response current flows through the interfacial medium to the ground electrode and there is little or no current flowing through the neural membrane during impedance characterization.

4.2. Theoretical framework

4.2.1. Nonlinear dielectric medium

The electric displacement D in terms of polarization P in the presence of an electric field E is given by

$$D = \varepsilon_0 E + P \tag{24}$$

where ε_0 is the permittivity of the free space. For a nonlinear dielectric the polarization can be extended into a power series in the electric field as [68]

$$P = P_0 + P_1(t) + P_2(t) + \ldots + P_n(t) + \ldots \tag{25}$$

$$\begin{gathered} = P_0(t) + \varepsilon_0 \int_{-\infty}^{\infty} R_1(\tau) E(t-\tau) d\tau + \varepsilon_0 \iint_{-\infty}^{\infty} R_2(\tau_1, \tau_2) E(t-\tau_1) E(t-\tau_2) d\tau_1 d\tau_2 \\ + \ldots + \varepsilon_0 \int \ldots \int_{-\infty}^{\infty} R_n(\tau_1, \ldots, \tau_n) E(t-\tau_1) \ldots E(t-\tau_n) d\tau_1 \ldots d\tau_n + \ldots \end{gathered} \tag{26}$$

where P_0 is the static polarization that is independent of the applied electric field, R_i are the ith order polarization response functions dependent on the time lag variables τ_i. The polarization response functions are zero for any one of τ_is less than zero to ensure causality of the system response. As such, equation (26) bears a striking resemblance to the terms of the Volterra series in equation (1) (chapter 2). Now expressing $E(t)$ in terms of its Fourier transform $E(\omega)$ using the Fourier integral identity

$$E(t) = \int_{-\infty}^{\infty} d\omega E(\omega) e^{-i\omega t} \tag{27}$$

where

$$E(\omega) = \frac{1}{2\pi} \int_{-\infty}^{\infty} dt E(t) e^{i\omega t} \tag{28}$$

And substituting in the second term corresponding to the linear polarization in equation (26) one gets

$$P_1(t) = \varepsilon_0 \int_{-\infty}^{\infty} d\omega \int_{-\infty}^{\infty} d\tau R_1(\tau) E(\omega)\, e^{-i\omega(t-\tau)} \tag{29}$$

$$= \varepsilon_0 \int_{-\infty}^{\infty} d\omega \chi_1(-\omega_\sigma; \omega) E(\omega)\, e^{-i\omega t}$$

where

$$\chi_1(-\omega_\sigma; \omega) = \int_{-\infty}^{\infty} d\tau R_1(\tau)\, e^{i\omega\tau} \tag{30}$$

is the linear susceptibility tensor and $\omega_\sigma = \omega$. Substituting the Fourier transform for $E(t)$ now in the third term of equation (26) one gets

$$P_2(t)$$
$$= \varepsilon_0 \int_{-\infty}^{\infty} d\omega_1 \int_{-\infty}^{\infty} d\omega_2 \int_{-\infty}^{\infty} d\tau_1 \int_{-\infty}^{\infty} d\tau_2 R_2(\tau_1, \tau_2) E(\omega_1) E(\omega_2) \mathrm{e}^{-i[\omega_1(t-\tau_1) + \omega_2(t-\tau_2)]} \tag{31}$$

$$= \varepsilon_0 \int_{-\infty}^{\infty} d\omega_2 \chi_2(-\omega_\sigma; \omega_1, \omega_2) E(\omega_1) E(\omega_2)\, e^{-i\omega_\sigma t}$$

where

$$\chi_2(-\omega_\sigma; \omega_1, \omega_2) = \int_{-\infty}^{\infty} d\tau_1 \int_{-\infty}^{\infty} d\tau_2 R_2(\tau_1, \tau_2)\, e^{i[\omega_1\tau_1 + \omega_2\tau_2]} \tag{32}$$

is the second order dielectric susceptibility tensor and $\omega_\sigma = \omega_1 + \omega_2$. Similarly the nth order polarization is given by

$$P_n(t) = \varepsilon_0 \int_{-\infty}^{\infty} d\omega_1 \ldots \int_{-\infty}^{\infty} d\omega_n \int_{-\infty}^{\infty} d\tau_1 \ldots \int_{-\infty}^{\infty} d\tau_n\, R_n(\tau_1, \ldots, \tau_n)$$
$$E(\omega_1) \ldots E(\omega_n) e^{-i[\omega_1(t-\tau_1) + \cdots + \omega_n(t-\tau_n)]} \tag{33}$$

$$= \varepsilon_0 \int_{-\infty}^{\infty} d\omega_1 \dots \int_{-\infty}^{\infty} d\omega_n \chi_n(-\omega_\sigma; \omega_1, \dots, \omega_n) E(\omega_1) \dots E(\omega_n)\, e^{-i\omega_\sigma t}$$

where

$$\chi_n(-\omega_\sigma; \omega_1, .. \omega_n) = \int_{-\infty}^{\infty} d\tau_1 \dots \int_{-\infty}^{\infty} d\tau_n R_n(\tau_1, \dots \tau_n)\, e^{i[\omega_1\tau_1 + \dots + \omega_n\tau_n]} \tag{34}$$

is the nth order dielectric susceptibility tensor and $\omega_\sigma = \omega_1 + \dots + \omega_n$. Substituting equations (27), (29), (31) and (33) in equation (24), the electric displacement can be written as

$$\begin{aligned} D(t) &= \varepsilon_0 \int_{-\infty}^{\infty} d\omega E(\omega) e^{-i\omega t} \\ &\quad + \varepsilon_0 \sum_n \int_{-\infty}^{\infty} d\omega_1 \dots \int_{-\infty}^{\infty} d\omega_n \chi_n(-\omega_\sigma; \omega_1, \dots, \omega_n) E(\omega_1) \dots E(\omega_n)\, e^{-i\omega_\sigma t} \end{aligned} \tag{35}$$

The total current density is thus given by

$$J(t) = \frac{\partial D}{\partial t} \tag{36}$$

Substituting equation (35) in equation (36), the time dependent nonlinear current density can be obtained as

$$\begin{aligned} J(t) &= -i\omega\varepsilon_0 \int_{-\infty}^{\infty} d\omega E(\omega) e^{-i\omega t} \\ &\quad - i\omega_\sigma \varepsilon_0 \sum_n \int_{-\infty}^{\infty} d\omega_1 \dots \int_{-\infty}^{\infty} d\omega_n \chi_n(-\omega_\sigma; \omega_1, \dots, \omega_n) E(\omega_1) \dots E(\omega_n)\, e^{-i\omega_\sigma t} \end{aligned} \tag{37}$$

4.2.2. Connection to the impedance spectrum

In terms of the stimulus-response data-records corresponding to the bandlimited Gaussian white noise stimulus $V(t)$ and its corresponding output response $I(t)$ from the impedance spectroscopy experiment (Figure 15) equation (1) for the Volterra series can be rewritten as

$$\begin{aligned} I(t) = k_0 + \int_{-\infty}^{\infty} k_1(\tau)V(t-\tau)d\tau + \iint_{-\infty}^{\infty} k_2(\tau_1,\tau_2)V(t-\tau_1)V(t-\tau_2)d\tau_1 d\tau_2 \\ + \ldots + \int \ldots \int_{-\infty}^{\infty} k_n(\tau_1,\ldots,\tau_n)V(t-\tau_1)\ldots V(t-\tau_n)d\tau_1 \ldots d\tau_n + \ldots \end{aligned} \tag{38}$$

where the Volterra kernels k_i are zero for any τ_i less than zero. Now, substituting the Fourier transform for $V(t)$

$$V(t) = \int_{-\infty}^{\infty} d\omega V(\omega) e^{-i\omega t} \tag{39}$$

where

$$V(\omega) = \frac{1}{2\pi} \int_{-\infty}^{\infty} dt V(t) e^{i\omega t} \tag{40}$$

in equation (38) and employing a transformation similar to equations (29), (31) and (33) one gets

$$I(t) = \int_{-\infty}^{\infty} d\omega V(\omega) e^{-i\omega t} + \sum_n \int_{-\infty}^{\infty} d\omega_1 \dots \int_{-\infty}^{\infty} d\omega_n K_n(-\omega_\sigma; \omega_1, \dots, \omega_n) V(\omega_1) \dots V(\omega_n)\, e^{-i\omega_\sigma t} \tag{41}$$

where K_n are the Fourier transforms of the Volterra kernels k_n given by

$$K_n(-\omega_\sigma; \omega_1, .. \omega_n) = \int_{-\infty}^{\infty} d\tau_1 \dots \int_{-\infty}^{\infty} d\tau_n k_n(\tau_1, \dots \tau_n)\, e^{i[\omega_1\tau_1 + \dots + \omega_n\tau_n]} \tag{42}$$

Now, the output response current and the input stimulus bandlimited Gaussian white noise can be expressed in terms of current density $J(\omega)$ and electric field $E(\omega)$ as

$$J(\omega) = I(\omega)/A_e \tag{43}$$

$$E(\omega) = V(\omega)/d_{eg} \tag{44}$$

where A_e and $d_{eg}$are the effective area of the microelectrode and the distance between the center of the microelectrode and the ground electrode respectively. d_{eg} effectively reduces to the radius of the microelectrode because of the presence of the ground electrode in a highly conducting extracellular medium outside of the neuron-electrode cleft. Thus, substituting equations (43) and (44) in equation (41) we get

$$J(t) = \frac{d_{eg}}{A_e}\int_{-\infty}^{\infty} d\omega E(\omega) e^{-i\omega t} + \frac{{d_{eg}}^n}{A_e}\sum_n \int_{-\infty}^{\infty} d\omega_1 \dots \int_{-\infty}^{\infty} d\omega_n K_n(-\omega_\sigma;\omega_1,\dots,\omega_n) E(\omega_1)\dots E(\omega_n)\, e^{-i\omega_\sigma t} \tag{45}$$

Now, comparing the expressions for the current density $J(t)$ in equations (37) and (45) we get

$$-i\omega_\sigma \varepsilon_0 \chi_n(-\omega_\sigma;\omega_1,\dots,\omega_n) = \frac{{d_{eg}}^n}{A_e} K_n(-\omega_\sigma;\omega_1,\dots,\omega_n) \tag{46}$$

$$\chi_n(-\omega_\sigma;\omega_1,\dots,\omega_n) = \frac{i{d_{eg}}^n}{\omega_\sigma \varepsilon_0 A_e} K_n(-\omega_\sigma;\omega_1,\dots,\omega_n) \tag{47}$$

which gives the nth order dielectric susceptibility tensor χ_n in terms of the nth order Volterra kernels K_n. The only remaining task now is to connect the Volterra kernels to the experimentally estimated Wiener kernels. For a time-domain complete set of Wiener kernels this can be accomplished using the following relation [41]

$$k_n(\tau_1,..\tau_n) = \sum_{m=0}^{\infty} \frac{(-1)^m (n+2m)!\, P^m}{n!\, m!\, 2^m} \int_0^{\infty} d\lambda_1 \dots \int_0^{\infty} d\lambda_m h_{n+2m}(\tau_1,\dots\tau_n,\lambda_1,\lambda_1,\dots,\lambda_m\lambda_m) \tag{48}$$

where P is the input power level of the white noise stimulus. Substituting the nth order Fourier transforms of the Volterra kernels thus obtained from the impedance spectroscopy data-records into equation (47) would then give an estimate of the experimentally determined n^{th} order dielectric susceptibility tensor. It is important to note here, that while Wiener kernels depend on the power P of the input bandlimited Gaussian white noise with P figuring in the denominator in equations (6), (7) and (8), the Volterra kernels are independent of the power of the input stimulus as P figures in the numerator of equation (48). As a result, the material parameters estimated using Volterra kernels are also independent of the power of the input stimulus as they ought to be.

The nth order complex dielectric permittivity tensor ε_n for a nonlinear system is given by

$$\varepsilon_n(-\omega_\sigma;\omega_1,\dots,\omega_n)=\varepsilon_0(\delta_{1,n}+\chi_n(-\omega_\sigma;\omega_1,\dots,\omega_n)) \tag{49}$$

where $\delta_{1,n}$ is the Kronecker delta, and,

Separating into real and imaginary parts equation (49) can be written as

$$\begin{aligned}&\varepsilon_n{}'(-\omega_\sigma;\omega_1,\dots,\omega_n)+i\varepsilon_n{}''(-\omega_\sigma;\omega_1,\dots,\omega_n)\\&\qquad=\varepsilon_0(\delta_{1,n}+\chi_n{}'(-\omega_\sigma;\omega_1,\dots,\omega_n)+i\chi_n{}''(-\omega_\sigma;\omega_1,\dots,\omega_n))\end{aligned} \tag{50}$$

Using equation (47), one can now write

$$\begin{aligned}&\varepsilon_n{}'(-\omega_\sigma;\omega_1,\dots,\omega_n)+i\varepsilon_n{}''(-\omega_\sigma;\omega_1,\dots,\omega_n)\\&\qquad=\frac{d_{eg}{}^n}{\omega_\sigma A_e}(\delta_{1,n}+iK_n{}'(-\omega_\sigma;\omega_1,\dots,\omega_n)-K_n{}''(-\omega_\sigma;\omega_1,\dots,\omega_n))\end{aligned} \tag{51}$$

Since the imaginary part of the nth order dielectric permittivity tensor is related to the nth order conductivity tensor through the relation $\varepsilon_n''=\sigma_n/\omega_\sigma$, the nth order conductivity tensor in terms of the experimentally estimated n^{th} order Volterra kernel can be written as

$$\sigma_n(-\omega_\sigma;\omega_1,\dots,\omega_n) = \frac{{d_{eg}}^n}{A_e} {K_n}'(-\omega_\sigma;\omega_1,\dots,\omega_n) \tag{52}$$

Using the generalized Einstein's relation the diffusivity tensor for ionic transport can be written as

$$D_n(-\omega_\sigma;\omega_1,\dots,\omega_n) = \frac{kT}{\sum_i z_i^2 e^2 n_i} \frac{{d_{eg}}^n}{A_e} {K_n}'(-\omega_\sigma;\omega_1,\dots,\omega_n) \tag{53}$$

where z_i and n_i are the valence and number density of the ith species of ions, k is the Boltzmann's constant and T is the temperature in Kelvin.

Thus, equations (51), (52) and (53) give us the material parameters that we were interested in estimating through Volterra-Wiener characterization.

4.3. Discussion

That electrode-electrolyte interfaces behave nonlinearly has been well known for a very long time now. But it had been possible to ignore this fact until recently because in most macroscopic systems studied it was possible to completely neglect the nonlinear electric double layer effects as the dominant characteristic had been the system linearity. However, as system and device sizes have shrunk over the past decade and a half with the advent of nanotechnology, experimentally observed nonlinear behavior of electrolytic interfaces in mesoporous electrode materials and in the study of biomolecular and bioelectrical interfaces has become the more accepted norm [69-72]. As much as the detection and understanding of these nonlinear effects at electrical interfaces have gained in importance for the design and development of nanoscale devices, the development of impedance characterization techniques to study these effects has failed to keep pace with it. The practice of employing sinusoidal inputs with linear impedance spectroscopy has now been extended to include the detection and analysis of higher order harmonics generated by the nonlinear system under study [69-76]. But as mentioned earlier, inputs to nonlinear systems do not follow the principle of superposition and hence such an approach to study of nonlinear electrochemical systems is inefficient because it does not allow one to understand the nonlinear interactions in the system for a real life stimulus signal with a finite spectral spread and varying amplitude in time. Also, within the theoretical framework of linear impedance spectroscopy, as a result, it is not possible to estimate the nonlinear material properties that influence the electrical behavior of the system under study. Specialized inputs, other than sinusoids, such as steps, impulses, multiple sinusoids and random white noise have also been employed for characterizing electrochemical systems but special care is always taken to operate in the linear regime to allow for a Fast Fourier Transform (FFT) analysis of the system output [66, 67]. Again, either the nonlinear regime of system behavior is completely avoided or is limited to a harmonic analysis. In this context, the theoretical framework presented in this chapter shows that the mathematical machinery of non-parametric Volterra-Wiener modeling can be successfully employed using bandlimited Gaussian white noise stimulus to efficiently extract material parameters for a nonlinear conducting dielectric and completely characterize its behavior through nonlinear impedance spectroscopy.

4.4. Conclusions

To be able to engineer the neuron-microelectrode interface, it requires an understanding of the nonlinear material properties of the interfacial medium and its response to electrical stimuli in the frequency range of the spectral composition of the action potentials generated by neurons that constitute its natural input. Such an understanding can then facilitate a tailoring of the properties of the interfacial medium and the recording electrode by affecting a change in the surface chemical properties and microstructure of the recording electrode or rheological properties of the interfacial medium that affect electrokinetic transport of ions at the neuron-microelectrode junction. The method of nonlinear impedance spectroscopy presented in this chapter can thus help apply these strategies towards a successful engineering of the neuroelectronic interface.

CHAPTER-5: DEVELOPMENT OF A LATTICE BOLTZMANN METHOD BASED MULTIPHYSICS SOLVER

5.1. Introduction

At the neuroelectronic interface, an ionic concentration gradient produced from an efflux (K^+) or influx (Na^+) of ions due to opening and closing of the voltage gated ion-channels in the neural membrane leads to the flow of an ionic diffusion current through the interfacial medium. This concentration gradient in turn results in a potential gradient between the interfacial cleft and the bulk extracellular medium leading to electromigration or electrophoresis of the ions. The electromigration of ions under this concentration gradient generated electric field exerts a drag force on the solvent molecules in the interfacial medium giving rise to an electroosmotic flow which by itself can again give rise to an ionic concentration gradient through convection. Thus, the electrodiffusion of ions in the interfacial medium at the neuron-microelectrode junction is a multiphysics problem (Figure 16). A rational approach towards an engineering of the neuron-microelectrode interface, therefore, must make use of multiphysics simulations that allow one to systematically tune the material and geometric parameters of the neuroelectronic interface that affect signal transduction for maximal signal to noise ratio.

Traditionally, electrokinetic phenomena are simulated using multiphysics solvers based on the Poisson-Nernst-Planck system of equations (54) and (55) coupled to the Navier-Stokes equation (56) through the body force term as given below [77]

$$\nabla^2\psi = -\frac{\sum_i z_i e n_i^b \exp\left(\frac{-z_i e\psi}{kT}\right)}{\varepsilon} \tag{54}$$

$$\frac{\partial n_i}{\partial t} + (\boldsymbol{u}\cdot\boldsymbol{\nabla})n_i = \boldsymbol{\nabla}(D_i n_i) + \boldsymbol{\nabla}\cdot\left[\frac{z_i D_i n_i}{kT}\boldsymbol{\nabla}\psi\right] \tag{55}$$

$$\rho\left[\frac{\partial \boldsymbol{u}}{\partial t} + (\boldsymbol{u}\cdot\boldsymbol{\nabla})\boldsymbol{u}\right] = \rho\nu\nabla^2\boldsymbol{u} + \rho\boldsymbol{F} \tag{56}$$

where ψ is the electric potential; z_i, D_i and n_i^b the ionic valence, diffusivity and bulk number density of the ith ionic specie; e the magnitude of the charge on an electron; k the Boltzmann constant; T the temperature; ε the dielectric permittivity of the solvent medium; ρ, ν and $\boldsymbol{u}$ the density, viscosity and the macroscopic velocity of the solvent; and, $\boldsymbol{F}$ is the external body force term given in general by $\rho\boldsymbol{F} = -\boldsymbol{\nabla p} + \rho_e\boldsymbol{F}$ with $\rho_e$as the net charge density.

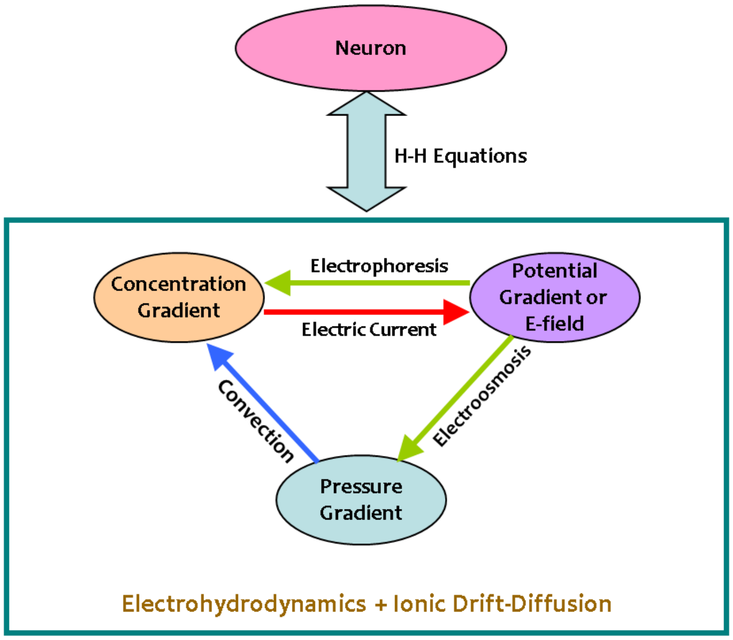
Neuron
H-H Equations
Concentration Gradient
Electrophoresis
Electric Current
Potential Gradient or E-field
Convection
Electroosmosis
Pressure Gradient
Electrohydrodynamics + Ionic Drift-Diffusion

Figure 16. A schematic of the inter-relationship between different electrokinetic processes and their coupling with the neuronal dynamics using Hodgkin-Huxley equations

The Nernst-Planck equation (Eq. (55)) and the Navier-Stokes equation (Eq. (56)) assume continuum dynamics. However, for the neuron-microelectrode interface cleft with a width of about 20-110 nm corresponding to Knudsen numbers (Kn, ratio of mean free path to the characteristic system length scale) between 0.015-0.003 for aqueous solutions, the assumption of continuum dynamics does not hold [77]. Besides assuming continuum dynamics, most commercially available multiphysics solvers linearize the Poisson-Boltzmann equation using the Debye-Huckel approximation ($exp\left(-\frac{e\psi}{kT}\right) \sim 1 - \frac{e\psi}{kT}$ for small ψ) and artificially extend out electric double layers by up to four orders of magnitude [78]. Therefore, for simulating ionic electrodiffusion at the neuron-microelectrode interface a multiphysics solver based on equations (55) and (56) would not be appropriate.

On the other hand, a molecular dynamics based simulation approach that requires tracking large number of entities accompanied by extremely small time steps would also be infeasible given the need to simulate action potentials on a time scale of few hundred microseconds to tens of milliseconds and the dimensions of the neuron-microelectrode interface (length on the scale of 30-40 μm and width between 20-110 nm). Under such a scenario, the Lattice Boltzmann Method (LBM) based on a statistical approach to time evolution of probability distribution functions for particles on a lattice offers a suitable alternative.

5.2. Lattice Boltzmann method - Background and a brief history of development

Lattice Boltzmann method is based on the Boltzmann transport equation and interestingly evolved as an improvisation of the Lattice Gas Cellular Automaton (LGCA) technique that was being employed to simulate fluid dynamics as an alternative to the continuum simulations using Navier-Stokes equation [79]. A cellular automaton is a collection of cells on a lattice that evolves in time through discrete time steps according to a set of rules dictated by the states of the neighboring cells on the lattice. Cellular automatons with their simple rules for time evolution on a lattice were an attractive proposition for simulation of fluid dynamics on a massively parallel scale using supercomputers. In 1986, Frisch, Hasschler and Pomeau showed that a simple cellular automaton that conformed to the microscopic laws of conservation could be employed to simulate fluid dynamics [79]. However, the LGCA approach to simulating fluid flows suffered from problems of lack of Galilean invariance and statistical noise [80, 81]. These problems were overcome over the years by the use of ensemble averaged populations of particles and choice of an appropriate lattice [82, 83]. Higuera and Jimenez [84] latter linearized the LGCA collision operator and employed the lattice Boltzmann equation (LBE) as a numerical tool which was subsequently replaced with the single relaxation time Bhatnagar-Gross-Krook (BGK) approximation [85]. Also, quite remarkably, a proper theoretical connection of the lattice Boltzmann equation to the Boltzmann transport equation was not made until 1997 when He and Luo showed the LBE to be a specially discretized form of the continuous Boltzmann transport equation [86, 87]. Ever since then, as more and more researchers have embraced the field in the past decade and a half, LBM has emerged as a promising new technique for the simulation of a host of multiphysics problems involving hydrodynamics and electrohydrodynamics in mesoscale systems due to the applicability of the Boltzmann transport equation at relatively large Knudsen numbers.

Since LBM based modeling as a field has not matured sufficiently yet and is still in a state of flux there are no commercially available multiphysics solvers that would allow for a simulation of the electrodiffusion of ions at the neuron-microelectrode interface. This, thus, necessitated the development of a multiphysics solver that could be employed for simulating electrokinetics in a mesoscale system. For the development of the multiphysics solver, the problem of simulating electrokinetics was divided into the following tractable parts:

- Simulation of hydrodynamic fluid flows
- Development of a solver for the Poisson-Boltzmann equation to solve for electric potential and field in response to spatial changes in ionic concentrations, and,
- Simulation of advection-diffusion of particles.

Each of these parts were validated using appropriate simple test problems and then coupled together in hierarchical steps of complexity to simulate the more complex problems of electroosmotic flow in a channel and charge relaxation dynamics in a mesoscale system.

5.3. Lattice Boltzmann algorithm

The non-dimensionalized Boltzmann equation in the BGK approximation can be written as [86]

$$\frac{\partial f}{\partial t} + \boldsymbol{\xi} \cdot \boldsymbol{\nabla} f + \boldsymbol{F} \cdot \boldsymbol{\nabla}_{\xi} f = -\frac{f - f^{eq}}{\tau} \tag{57}$$

where $\boldsymbol{F}$ is the external body force, $f \equiv f(\boldsymbol{r}, \boldsymbol{\xi}, t)$ is the phase space single particle distribution function, τ is the relaxation time due to collision, t the time, $\boldsymbol{\xi}$ the microscopic velocity, $\boldsymbol{r}$ the space coordinate and $f^{eq}$is the equilibrium distribution function for the Maxwell distribution.

The Maxwell's equilibrium distribution function is given by

$$f^{eq} = \frac{\rho}{(2\pi RT)^{m/2}} \exp\left[-\frac{(\boldsymbol{\xi} - \boldsymbol{u})^2}{2RT}\right] \tag{58}$$

where R is the gas constant and m is the number of dimensions of the configuration space. Realizing that f^{eq} is the leading term in a Taylor series expansion of f and that gradient of f^{eq} contributes most significantly to the gradient of f one can write

$$\boldsymbol{\nabla}_{\xi} f \approx \boldsymbol{\nabla}_{\xi} f^{eq} = -\frac{(\boldsymbol{\xi} - \boldsymbol{u})}{RT} f^{eq} \tag{59}$$

Substituting equation (59) in equation (57) one obtains

$$\frac{\partial f}{\partial t} + \boldsymbol{\xi} \cdot \boldsymbol{\nabla} f = -\frac{f - f^{eq}}{\tau} + \frac{\boldsymbol{F} \cdot (\boldsymbol{\xi} - \boldsymbol{u})}{RT} f^{eq} \tag{60}$$

Further it can be shown that equation (60) after discretization in time and integration over the time step Δt can be used to obtain the discrete lattice Boltzmann equation (LBE) as

$$f_\alpha(\boldsymbol{r} + \boldsymbol{e}_\alpha \Delta t, t + \Delta t) = f_\alpha(\boldsymbol{r}, t) - \frac{f_\alpha(\boldsymbol{r}, t) - f_\alpha{}^{eq}(\boldsymbol{r}, t)}{\tau_{\mathrm{v}}} + \Delta t \frac{\boldsymbol{F} \cdot (\boldsymbol{e}_\alpha - \boldsymbol{u})}{RT} f_\alpha{}^{eq}(\boldsymbol{r}, t) \tag{61}$$

where τ_{v} is the non-dimensional relaxation time, $\boldsymbol{e}_\alpha$ is the discrete particle velocity. The macroscopic density and the momentum density are then given by

$$\rho = \sum_\alpha f_\alpha = \sum_\alpha f_\alpha^{eq} \tag{62}$$

$$\rho \boldsymbol{u} = \sum_\alpha \boldsymbol{e}_\alpha f_\alpha \tag{63}$$

An expansion of equation (58) in the small velocity approximation yields the equilibrium distribution function, the discretized form of which is given by

$$f_\alpha^{eq} = w_\alpha \rho \left[1 + \frac{\boldsymbol{e}_\alpha \cdot \boldsymbol{u}}{RT} + \frac{(\boldsymbol{e}_\alpha \cdot \boldsymbol{u})^2}{2(RT)^2} - \frac{\boldsymbol{u}^2}{2RT} \right] \tag{64}$$

where w_α are weights computed using the Gauss-Hermite quadrature employed to accurately compute the hydrodynamic moments of the distribution function f [86]

$$\int \boldsymbol{\xi}^p f^{eq} d\boldsymbol{\xi} \tag{65}$$

through a discretization of the momentum space in terms of the discrete particle velocities $\boldsymbol{e}_\alpha$. Here $0 \leq p \leq 3$ for isothermal models. For a two dimensional D2Q9 LBM model (Figure 17), employed in the present work for the development of an LBM based multiphysics solver, with three speeds and nine discrete particle velocities the weights w_α are given by

$$w_1 = \frac{4}{9}, w_{2-5} = \frac{1}{9}, \text{and } w_{6-9} = \frac{1}{36} \tag{66}$$

The discrete particle velocities $\boldsymbol{e}_\alpha$ are given by

$$\boldsymbol{e_1} = [0,0], \boldsymbol{e_{2,4}} = [\pm c, 0], \boldsymbol{e_{3,5}} = [0, \pm c] \text{ and } \boldsymbol{e_{6-9}} = [\pm c, \pm c] \tag{67}$$

where $c = \frac{\Delta x}{\Delta t} = \sqrt{3} c_s$ is the lattice speed of sound and c_s the speed of sound in the fluid medium given by $c_s = \sqrt{RT}$.

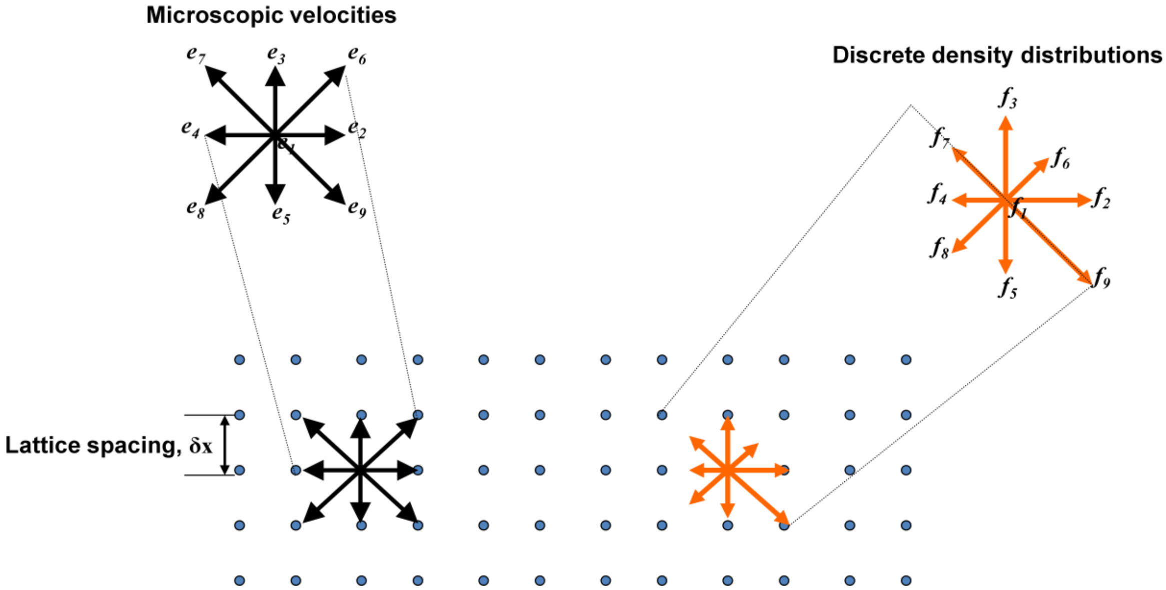
Microscopic velocities
e_7
e_3
e_6
e_4
e_1
e_2
e_8
e_5
e_9
Discrete density distributions
f_3
f_7
f_6
f_4
f_1
f_2
f_8
f_5
f_9
Lattice spacing, δx

Figure 17. A schematic showing the nine directional density distributions and the discrete particle velocities for the two dimensional D2Q9 lattice

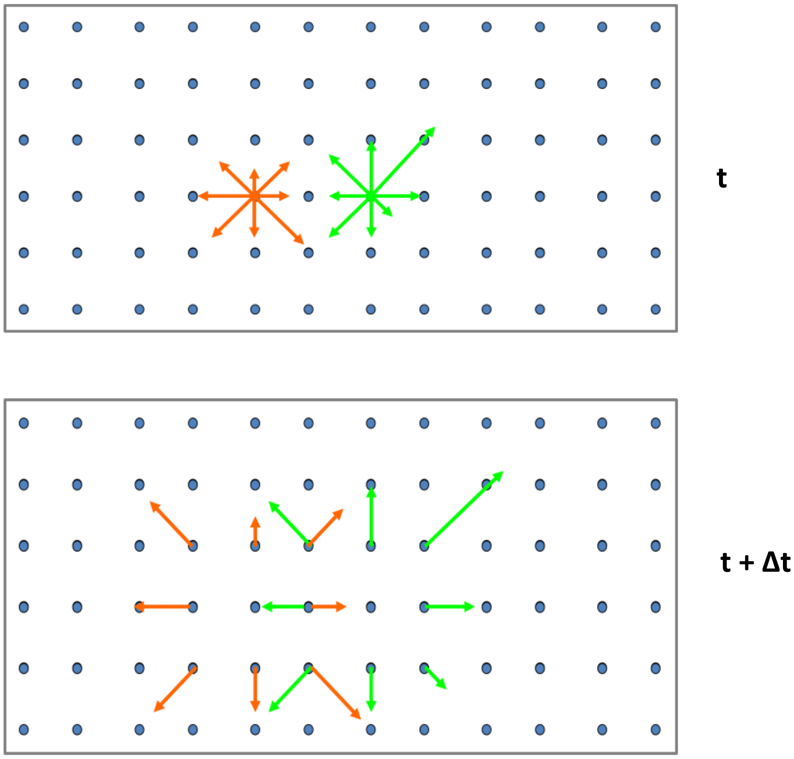

Figure 18. A schematic showing the streaming of the density distribution functions on the lattice defining the simulation domain from time t to $t + \Delta t$.

Thus, beginning with the Boltzmann transport equation (Eq. 57) in the continuous phase space one obtains the discrete lattice Boltzmann equation (Eq. (61)) in a reduced phase space that greatly diminishes the computational requirements associated with the computation of the moments of the continuous distribution functions and at the same time allows one to retain the simplicity of the LGCA models with their characteristic ease of parallelization.

In a typical implementation, the LBM algorithm follows the simple sequence of boundary, collide and stream for the time evolution of directional distribution functions f_α on the lattice. The streaming operation is represented by the term $f_\alpha(\boldsymbol{r} + \boldsymbol{e}_\alpha \Delta t, t + \Delta t)$ on the LHS of the lattice Boltzmann equation (Eq. (61)) and is pictorially depicted in Figure 18 for population densities on two lattice nodes represented in two different colors. All codes for the multiphysics solver were implemented in FORTRAN and parallelized using message passing interface (MPI) subroutines in MPICH2.0 developed by the Los Alamos National Lab.

5.4. Hydrodynamics – Simulating fluid flows

Hydrodynamic fluid flows were simulated using the lattice Boltzmann equation (Eq. (61)) minus the external body force term. It can be shown using a Chapman-Enskog or multiscale expansion that in the regime of small Knudsen numbers the Navier-Stokes equation (Eq. (56)) can be recovered from the LBE (Eq. (61)). In the case of fluid flows, the non-dimensional BGK relaxation time τ_v is given in terms of the viscosity ν by

$$\tau_\mathrm{v} = 3\nu \frac{\Delta t}{\Delta x^2} + 0.5 \qquad (68)$$

The LBM code for simulating hydrodynamic fluid flows was validated using the entrance flow problem.

5.4.1. Entrance flow problem

The entrance flow problem is a classic fluid flow problem in which the development of an incompressible fluid flow is simulated in a channel that connects two reservoirs placed at different elevations causing a pressure difference to exist between the inlet and the outlet of the channel [88]. It is assumed that as the fluid flows between the two reservoirs over time, there is no change in the pressures at the inlet or the outlet of the channel. In the steady state, the entrance profile for the pressure is flat in the free slip region followed by a rapid drop-off close to the mouth of the channel walls with no-slip boundaries (Figure 19). Once a parabolic velocity flow profile corresponding to Poiseuille flow develops in the channel, the pressure drops off linearly to the pressure at the outlet.

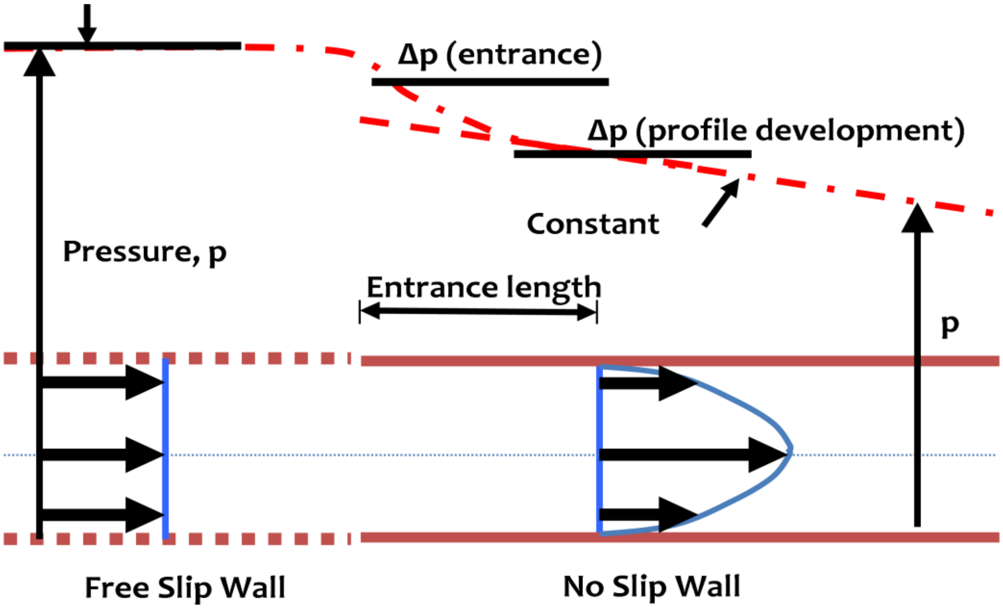
Δp (entrance)
Δp (profile development)
Constant
Pressure, p
Entrance length
p
Free Slip Wall
No Slip Wall

Figure 19. Pressure driven flow in a channel connecting two reservoirs

5.4.2. Boundary conditions

The effect of the reservoir at the inlet was simulated using the free slip boundary condition on the boundaries of the simulation domain parallel to the flow direction (Figure 19). The free-slip boundary condition makes use of specular reflection of the density distribution functions f_α such that there is negligible friction exerted on the fluid flow and the tangential component of the momentum remains unchanged. For example on the upper free-slip wall of the channel these boundary conditions can be implemented as [81]

$$f_9 = f_6;\ f_8 = f_7 \text{ and } f_5 = f_3 \tag{69}$$

After streaming, the density distributions pointing out of the simulation domain are known (in the above case, $f_{3,6,7}$) while the distributions pointing into the simulation domain ($f_{5,8,9}$) are unknown (Figure 17). The no-slip boundary condition designed to implement no tangential flux along the channel walls was implemented using bounce-back of the distribution functions. The bounce-back boundary conditions for the upper no-slip channel wall are given by

$$f_9 = f_7;\ f_8 = f_6 \text{ and } f_5 = f_3 \tag{70}$$

Similar to equations (69) and (70) the free-slip and no-slip boundary conditions can also be implemented on the lower boundary walls of the simulation domain.

At the free-slip inlet, a velocity boundary condition of $\boldsymbol{u} = [u_{in}, 0]$ was imposed while at the outlet a pressure boundary condition was imposed by fixing the fluid density at $\rho_{out} = 1$ and assuming that the y-component of the fluid velocity at the outlet is zero. These boundary conditions were implemented using Zou-He velocity and pressure boundary conditions [89] that make use of non-equilibrium bounce-back of density distribution functions normal to the inlet and outlet boundaries such that

$$f_2 - f_2^{eq} = f_4 - f_4^{eq} \tag{71}$$

Employing equations (62) and (63) in conjunction with equation (71), the unknown distribution functions at the inlet can be computed as

$$f_2 = f_4 + \frac{2}{3}\rho u_{in} \tag{72}$$

$$f_6 = f_8 + \frac{f_5 - f_3}{2} + \frac{1}{6}\rho u_{in} \tag{73}$$

$$f_9 = f_7 - \frac{f_5 - f_3}{2} + \frac{1}{6}\rho u_{in} \tag{74}$$

while for the outlet the unknown distribution functions are as given below

$$f_4 = f_2 - \frac{2}{3}\rho_{out} u_x \tag{75}$$

$$f_8 = f_6 - \frac{f_5 - f_3}{2} - \frac{1}{6}\rho_{out} u_x \tag{76}$$

$$f_7 = f_9 + \frac{f_5 - f_3}{2} - \frac{1}{6}\rho_{out} u_x \tag{77}$$

5.4.3. Validation results

The entrance flow problem was simulated for a Reynolds number of $Re = 56$ and a non-dimensional inlet velocity of $\boldsymbol{u_{in}} = [0.05\ 0]$. A constant relaxation time of $\tau_{\mathrm{v}} = 1.3$ was employed for the simulations. Figure 20 and Figure 21 show excellent agreement between the theoretical predictions and the simulation results obtained from the LBM flow solver. The fluid, as it enters the channel, experiences a higher pressure close to the channel walls translating to lower flow velocities closer to the no-slip walls (Figure 20 A and B). Conversely, lower pressure in the center of the channel at the entrance translates to higher velocities as expected from the Bernoulli's equation. The pressure in the entrance length region of the flow drops off nonlinearly and then as the flow becomes laminar, with streamlines parallel to the channel wall, it drops off linearly (Figure 20 A and Figure 21 B).

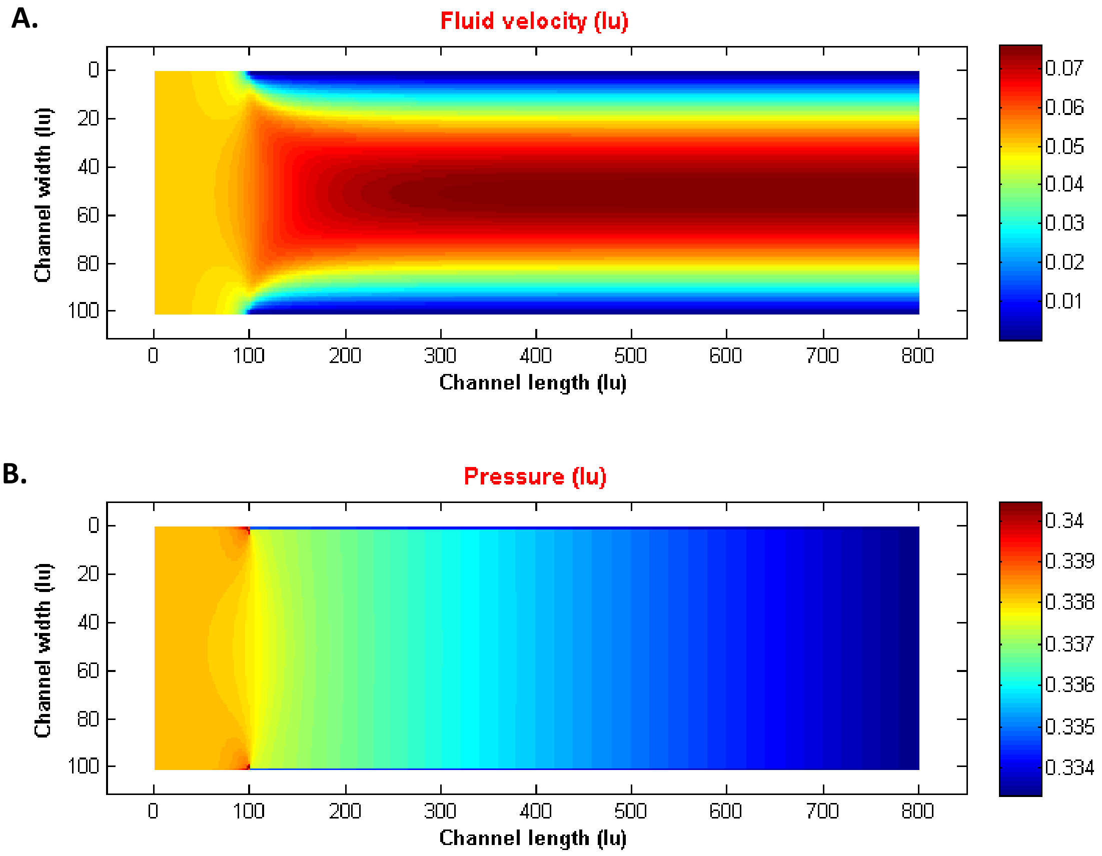

Figure 20. Fully developed Poiseuille flow in a microfluidic channel (A) velocity profile and (B) Pressure gradient along the length of the channel.

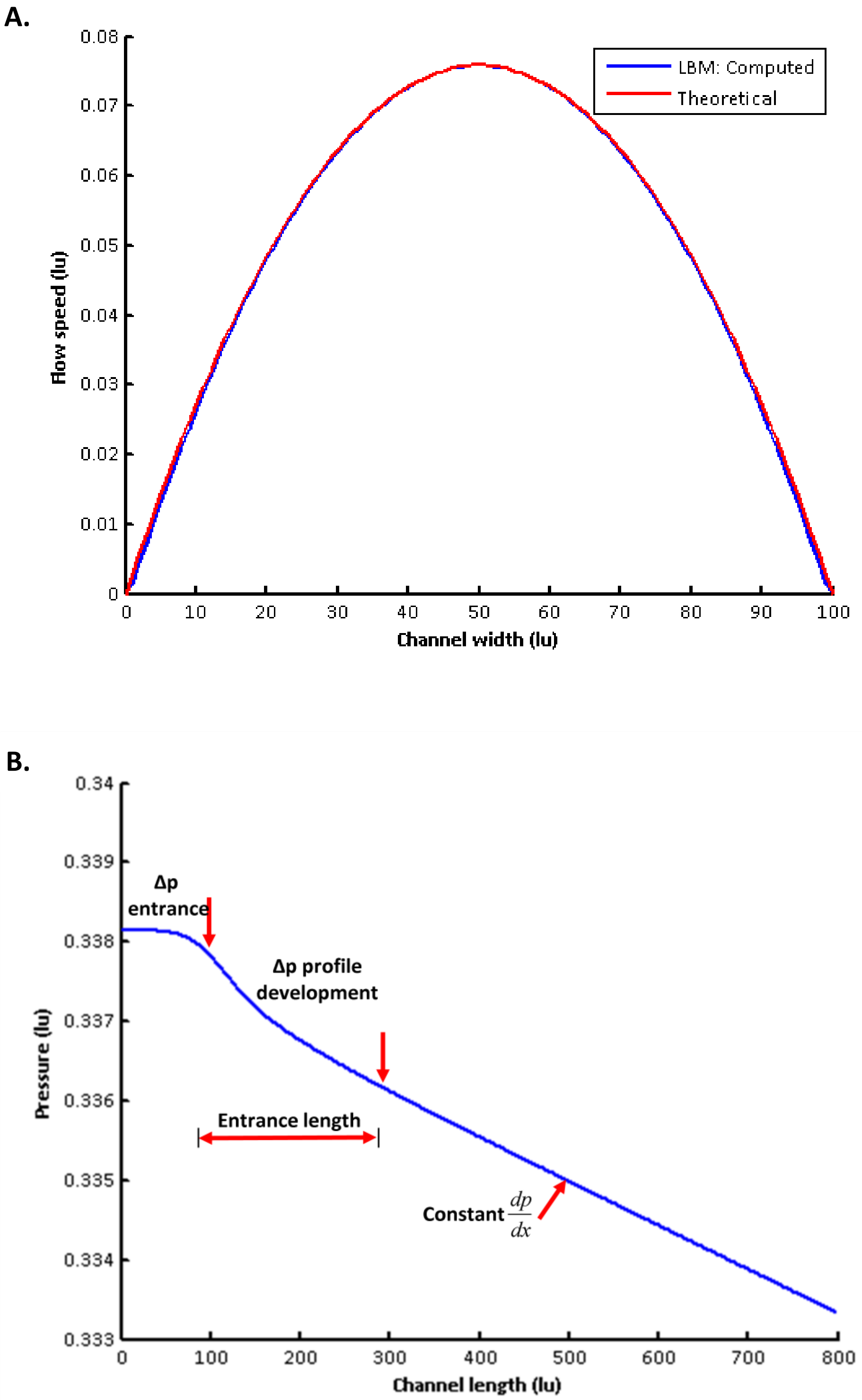

Figure 21. (A) Steady state parabolic flow profile across the width of the channel. (B) Pressure gradient along the length of the channel for a fully developed Poiseuille flow

As expected, the parabolic flow profile at the outlet of the channel matches very closely the theoretically computed parabolic flow profile characteristic of a Poiseuille flow (shown in Figure 21 A). These results, thus, validate the LBM based hydrodynamic fluid flow solver.

5.5. Lattice Poisson-Boltzmann Method - Computing electric potential and field

The next step in the development of the multiphysics solver was to develop an LBE based solver for the Poisson-Boltzmann equation (Eq. (54)) which could then be employed later to simulate electroosmotic flows or ionic drift-diffusion at the neuroelectronic interface. For accomplishing this, a lattice Poisson-Boltzmann method (LPBM) based solver developed by Wang et al was implemented [90].

5.5.1. Theory

The Poisson-Boltzmann equation (Eq. (54)) can be recast into a diffusion equation with pseudo time steps as

$$\frac{\partial \psi}{\partial \mathrm{t}} = \nabla^2 \psi + g_{rhs}(\boldsymbol{r}, \psi, t) \tag{78}$$

where

$$g_{rhs}(\boldsymbol{r}, \psi, t) = \frac{1}{\varepsilon} \sum_i z_i e n_i^b \exp\left(\frac{-z_i e \psi}{kT}\right) \tag{79}$$

is the RHS term of the Poisson-Boltzmann equation (Eq. (54)). The solution of the Poisson-Boltzmann equation is then the steady state solution of equation (78). Corresponding to equation (78), for a D2Q9 lattice, the pseudo-time evolution of the electric potential can be written in terms of a lattice Boltzmann like equation as

$$\begin{aligned} g_\alpha\left(\boldsymbol{r}+\boldsymbol{e}_\alpha\Delta t_g, t_g+\Delta t_g\right) \\ = g_\alpha\left(\boldsymbol{r}, t_g\right) - \frac{g_\alpha\left(\boldsymbol{r}, t_g\right) - g_\alpha^{eq}\left(\boldsymbol{r}, t_g\right)}{\tau_g} + \left(1-\frac{0.5}{\tau_g}\right)\Delta t_g w_\alpha g_{rhs}(\boldsymbol{r}, \psi, t) \end{aligned} \tag{80}$$

where Δt_g is the discrete pseudo-time step, τ_g the equivalent of the BGK relaxation time in LBE and the equilibrium distribution is given by

$$g_\alpha^{eq}\left(\boldsymbol{r}, t_g\right) = w_\alpha \psi\left(\boldsymbol{r}, t_g\right) \tag{81}$$

with

$$w_1 = 0;\ w_{2-5} = \frac{1}{6} \text{ and } w_{6-9} = \frac{1}{12} \tag{82}$$

$$\Delta t_g = \frac{\Delta x}{c_g} \tag{83}$$

where Δx is the lattice spacing and c_g is the pseudo-speed of sound for the electric potential on the lattice which can be employed to tune convergence rates of the LPBM solver to a steady state solution for the electric potential ψ. The electric potential itself in terms of the density distributions g_α is given by

$$\psi = \sum_\alpha g_\alpha + 0.5 w_\alpha \Delta t_g g_{rhs} \tag{84}$$

The relaxation time τ_g is given by

$$\tau_g = \frac{3\chi\Delta t_g}{2\Delta x^2} + 0.5 \tag{85}$$

where χ is referred to as the potential diffusivity on the lattice and is taken as unity for simulation purposes. The electric field can also be computed from the distribution functions g_α using the following relation

$$\boldsymbol{E} = \frac{c_g}{\chi} \sum_\alpha \boldsymbol{e}_\alpha g_\alpha = -\boldsymbol{\nabla}\psi \tag{86}$$

5.5.2. Electrode-electrolyte interface

The LPBM solver for the Poisson-Boltzmann equation (Eq. (54)) was then employed to solve for the electric potential and field in the electric double layer associated with an electrode-electrolyte interface when the electrode is held at a constant potential ψ_0.

5.5.2.1. Boundary conditions

A Dirichlet boundary condition with $\psi = \psi_0$ was applied on the electrode surface using equation (84) by using the assumption that the unknown distribution functions on the simulation domain boundary relax to an equilibrium potential ψ_N on the electrode surface. For example, if the electrode is placed at the upper boundary of the simulation domain then the unknown distribution functions $g_{5,8,9}$ can be computed using

$$g_5 = \frac{1}{6}\psi_N;\ g_8 = g_9 = \frac{1}{12}\psi_N \tag{87}$$

where, using equation (84), ψ_N is given by

$$\psi_N = 3\psi_0 - (g_1 + g_2 + g_3 + g_4 + g_6 + g_7) - 1.5 w_\alpha \Delta t_g g_{rhs} \tag{88}$$

A Neumann boundary condition of $E_y = 0$ was implemented on the wall opposite to the electrode surface using the y-component of equation (86).

5.5.2.2. Validation results

The electric potential profile in the electric double layer at the electrode-electrolyte interface was simulated on a 101×151 rectangular simulation domain with a lattice spacing of $\Delta x = 10\, nm$ for electrode surface potentials of 10, 30, 50, 100 and 150 mV and a bulk electrolyte concentration of $c_b = 0.1\, mM$. A value of $c_g = 18.2$ was employed for the pseudo-speed of sound for the electric potential on the lattice. The simulated results were then compared with the theoretical results from the solution of the linearized Poisson-Boltzmann equation under Debye-Huckel approximation given by

$$\psi = \psi_0 e^{-\kappa y} \tag{89}$$

$$E_y = \kappa \psi_0 e^{-\kappa y} \tag{90}$$

where κ^{-1} is the Debye length λ_D for a $1:1$ symmetric electrolyte given by

$$\lambda_D = \kappa^{-1} = \sqrt{\frac{\varepsilon k T}{2 n_i^b z_i^2 e^2}} \tag{91}$$

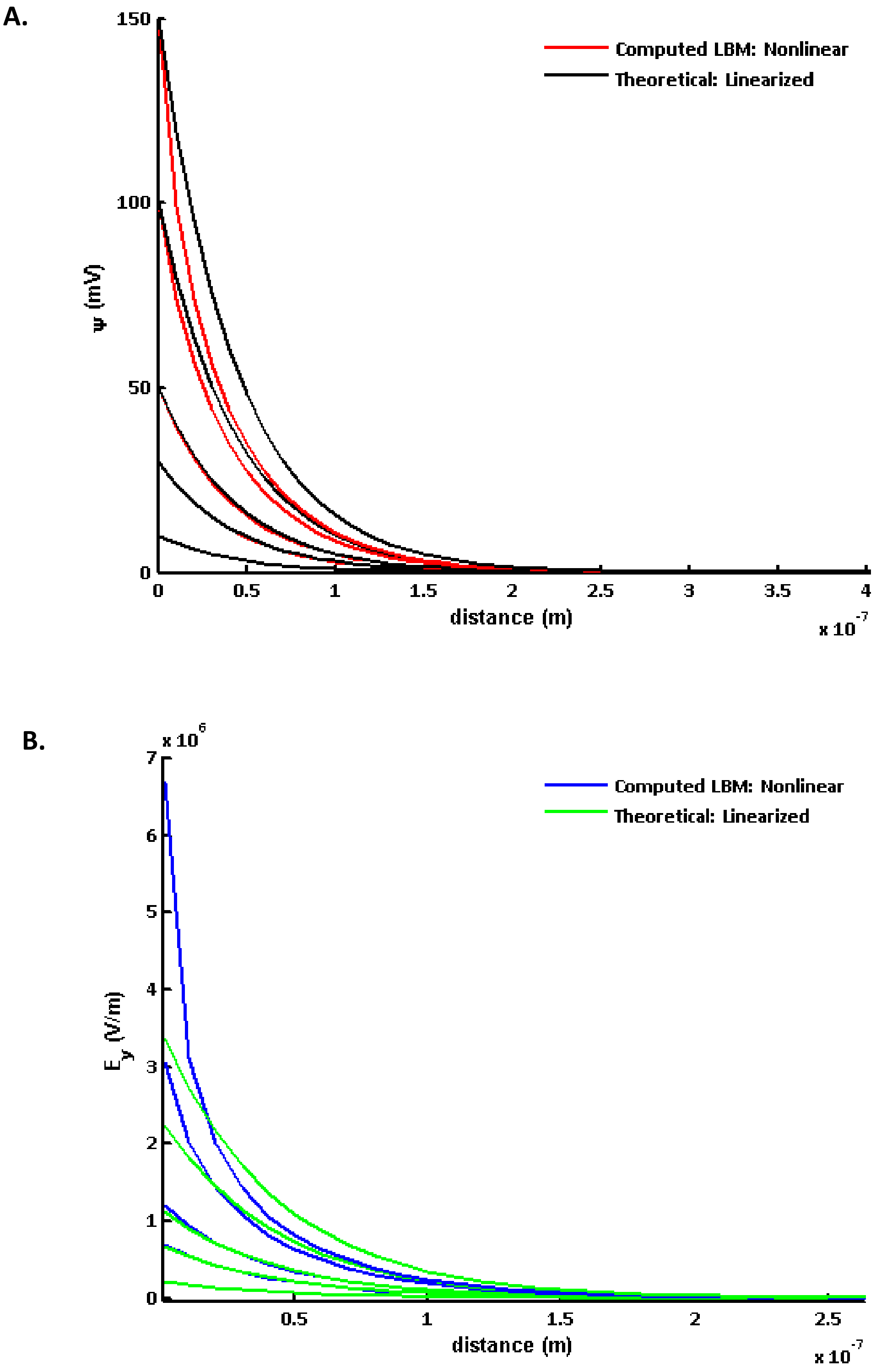

Figure 22. Results for electric (A) potential and (B) electric field profiles computed using Lattice Poisson Boltzmann Method compared with results obtained from Poisson's equation linearized using Debye-Huckel approximation for various electrode surface potentials (150, 100, 50, 30 and 10 mV) in a 0.1 mM 1:1 electrolyte solution.

The results showed excellent agreement with the theoretical results for electrode surface potentials of $\psi_0 < 30\,mV$ the regime for linear behavior but for $\psi_0 > 30\,mV$ the Debye shielding was stronger for the results obtained using the nonlinear LPBM solver (Figure 22).

5.6. Electroosmotic flow in a nanochannel

Electroosmotic flow in a nanochannel filled with an electrolytic solution results from an external electric field applied along the length of the channel. The walls of an electrolyte filled channel, because of their surface physicochemical properties, acquire a zeta-potential resulting in the formation of a static electric double layer associated with the channel walls. As a result, there exists a build-up of higher net charge density closer to the channel wall surfaces than at the center of the channel. Now, when an external electric field is applied parallel to the channel walls along its length the ions in the channel experience a force and start moving along the direction of the applied electric field. The movement of ions in response to the external electric field, in turn, exerts a drag force on the solvent molecules in the channel. As a result, the solvent or fluid molecules also start to move in the direction of the applied electric field. This movement of fluid that results because of an external electric field applied along the length of the channel is referred to as an electroosmotic flow. Since the direction of the applied electric field is parallel to the channel walls and the ions do not experience any force in a direction perpendicular to the channel walls, the equilibrium charge density profile across the width of the channel remains unchanged during the development of the electroosmotic flow in the channel.

5.6.1. Theory

Electroosmotic flow in nanochannels was simulated using the LBE (Eq. (61)) with the external force term given by

$$\boldsymbol{F} = \rho_e \boldsymbol{E} \tag{92}$$

The net charge density distribution $\rho_e(x, y)$ in the nanochannels for a given zeta-potential on the channel walls and the net electric field $\boldsymbol{E}$ resulting from the applied electric field $\boldsymbol{E_a}$ along the length of the channel were computed using the LPBM solver through equation (80). The net electric force, thus computed, was substituted in the LBE (Eq. (61)) to simulate electroosmotic flow in the nanochannels.

5.6.2. Boundary conditions

Dirichlet boundary conditions were implemented using equation (84) on channel walls to specify the surface zeta-potentials while equation (86) was employed to specify the Neumann boundary conditions at the inlet and the outlet of the nanochannels to specify the externally applied electric field along the length of the channel.

For the simulation of the electroosmotic fluid flow using LBE (Eq. (61)), periodic boundary conditions were implemented at the channel inlet and outlet. No-slip boundary conditions on the channel walls for the fluid flow were implemented using bounce-back of density distribution functions f_α as described in equation (70).

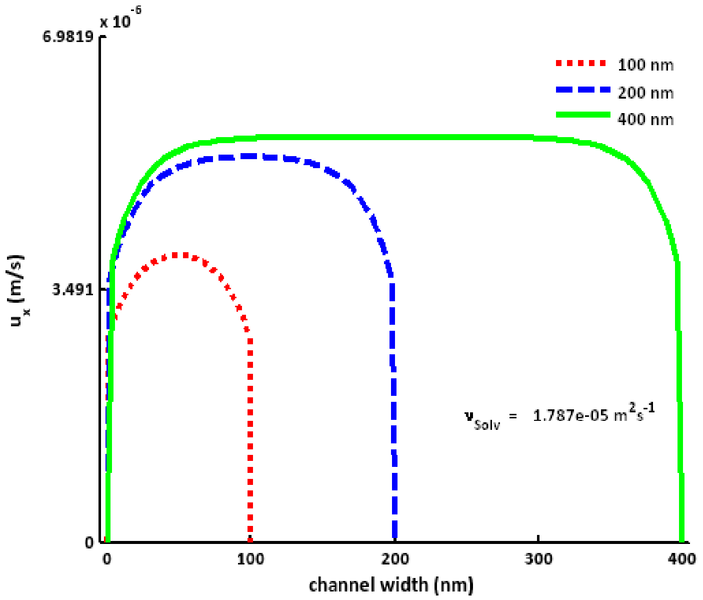

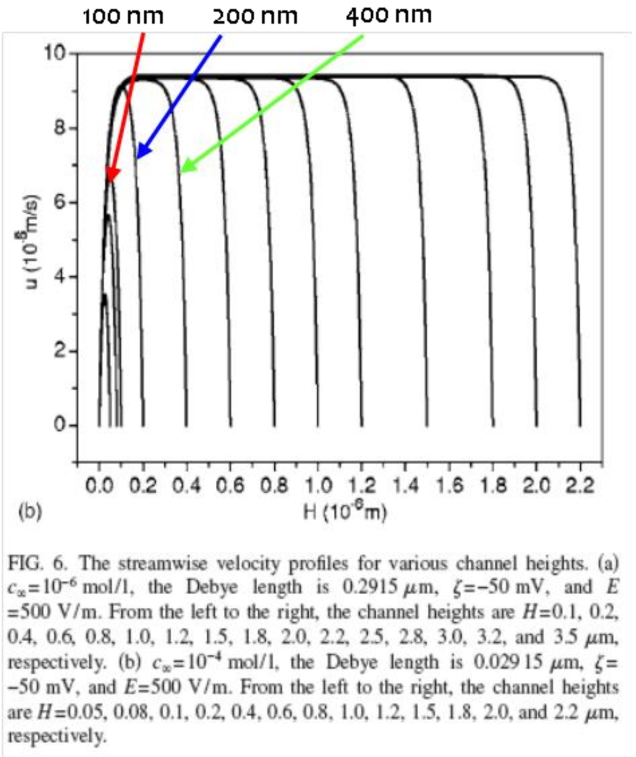

FIG. 6. The streamwise velocity profiles for various channel heights. (a) $c_\infty=10^{-6}$ mol/l, the Debye length is 0.2915 μm, $\zeta=-50$ mV, and $E=500$ V/m. From the left to the right, the channel heights are $H=0.1$, 0.2, 0.4, 0.6, 0.8, 1.0, 1.2, 1.5, 1.8, 2.0, 2.2, 2.5, 2.8, 3.0, 3.2, and 3.5 μm, respectively. (b) $c_\infty=10^{-4}$ mol/l, the Debye length is 0.029 15 μm, $\zeta=-50$ mV, and $E=500$ V/m. From the left to the right, the channel heights are $H=0.05$, 0.08, 0.1, 0.2, 0.4, 0.6, 0.8, 1.0, 1.2, 1.5, 1.8, 2.0, and 2.2 μm, respectively.

Figure 23. (A) Streamwise velocity profiles for electroosmotic flows in channels with widths of 100, 200 and 400 nm with a zeta potential of $\zeta = -50$ mV, $c_\infty = 0.1$ mM, solvent viscosity of $\upsilon = 1.787 \times 10^{-5}$ m^2/s and a lateral electric field of $E = 500$ V/m. (B) Results from Tang et al, J. App. Phys. 100 ,094908 (2006) for comparison.

5.6.3. Validation results

The results for electroosmotic flow simulations were validated against the published results of Tang et al [91]. A zeta potential of $\zeta = -50\ mV$ was applied on the channel walls while an external electric field of $E_x = 500\ V/m$ was applied across the length of the channels. The bulk electrolyte concentration was specified as $c_b = 0.1\ mM$ and the fluid viscosity was taken to be $\nu = 1.787 \times 10^{-5}\ m^2/s$. Simulations were carried out for channel widths of 100, 200 and 400 nm and a good match was found between simulated and published results (Figure 23 A and B).

5.7. Advection-diffusion of solute particles

A prerequisite for simulating ionic electrodiffusion at the neuron-microelectrode interface is the ability to solve for advection diffusion of particles in a fluid. This section presents results from the simulation of the advection-diffusion of an instantaneous point source of particles created at the center of the simulation domain under the influence of a concentration gradient and convection due to fluid flow.

5.7.1. Theory

5.7.1.1. One dimensional advection-diffusion

One dimensional advection-diffusion of particles was simulated using a one-dimensional three velocity D1Q3 LBM model. In the D1Q3 LBM model, the discrete particle velocities $\boldsymbol{e}_\alpha$ and the weights w_α for the corresponding distribution functions f_α ($\alpha \equiv 1, 2 \text{ and } 3$) are specified as

$$w_1 = \frac{2}{3}, w_2 = \frac{1}{6}, \text{and } w_3 = \frac{1}{6} \tag{93}$$

$$\boldsymbol{e_1} = 0, \boldsymbol{e_2} = 1, \text{and } \boldsymbol{e_3} = -1 \tag{94}$$

For the time evolution of the particle concentrations, the LBE excluding the body force term from equation (61) was used with the D1Q3 model parameters specified in equations (93) and (94).

5.7.1.2. Two dimensional advection-diffusion

Two dimensional advection-diffusion was simulated using the lattice Boltzmann algorithm outlined in section 5.3 for the D2Q9 model. LBE in equation (61) was employed to solve for the time evolution of the density distribution functions.

The non-dimensional velocity relaxation time for the solute particles was specified in terms of their diffusion coefficient as

$$\tau_D = 3D\frac{\Delta t}{\Delta x^2} + 0.5 \tag{95}$$

5.7.2. Boundary conditions

Simulations for, both one and two dimensional cases of advection-diffusion were performed for instantaneous point sources initialized at $t = 0$ in large reservoirs. Although no flux bounce-back boundary conditions were employed on the simulation boundaries, the simulations were restricted to a total time wherein the effects of the simulation domain boundary could be neglected.

5.7.3. Validation Results

The results for one and two dimensional advection and diffusion were validated against closed form theoretical solution of the advection-diffusion equation for instantaneous point source released at the center of the simulation domain given by

$$n(\boldsymbol{r}, t) = n_{init} + \frac{n_0}{\left(2\sqrt{\pi D t}\right)^m} exp\left[\frac{-(\boldsymbol{r} - \boldsymbol{r_0} - \boldsymbol{u}t)^2}{\left(2\sqrt{\pi D t}\right)^m}\right] \tag{96}$$

where D is the diffusion coefficient of the solute, m the dimension of the simulation or solution domain, $\boldsymbol{r}$ is the position vector and $\boldsymbol{r_0}$ is the position vector of the point of release of the instantaneous point source at $t = 0$.

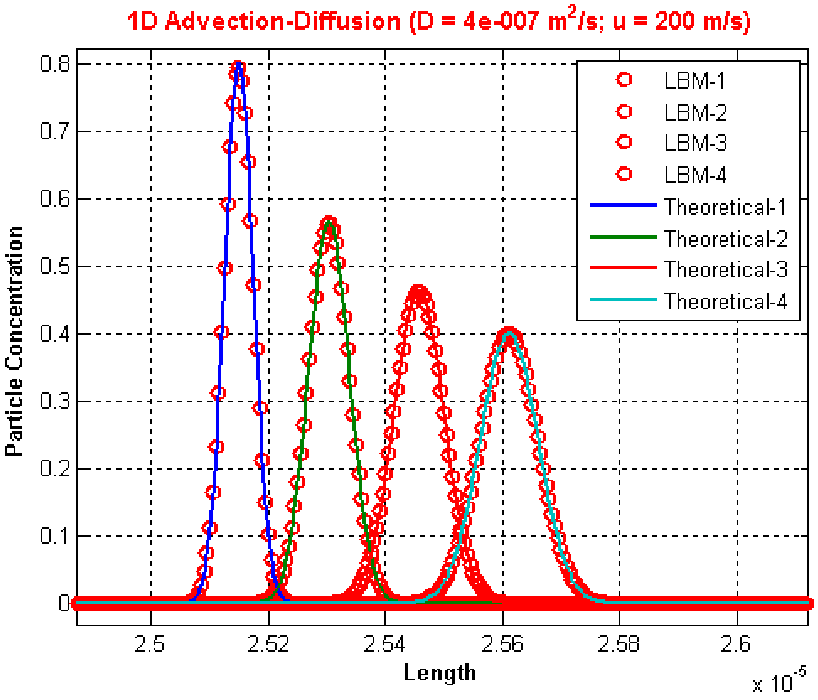

Figure 24. Advection-diffusion of an instantaneous point source created in the center of the simulation domain at $t = 0$. The peaks from left to right denote particle concentration profiles at 0.77, 1.54, 2.31 and 3.08 ns.

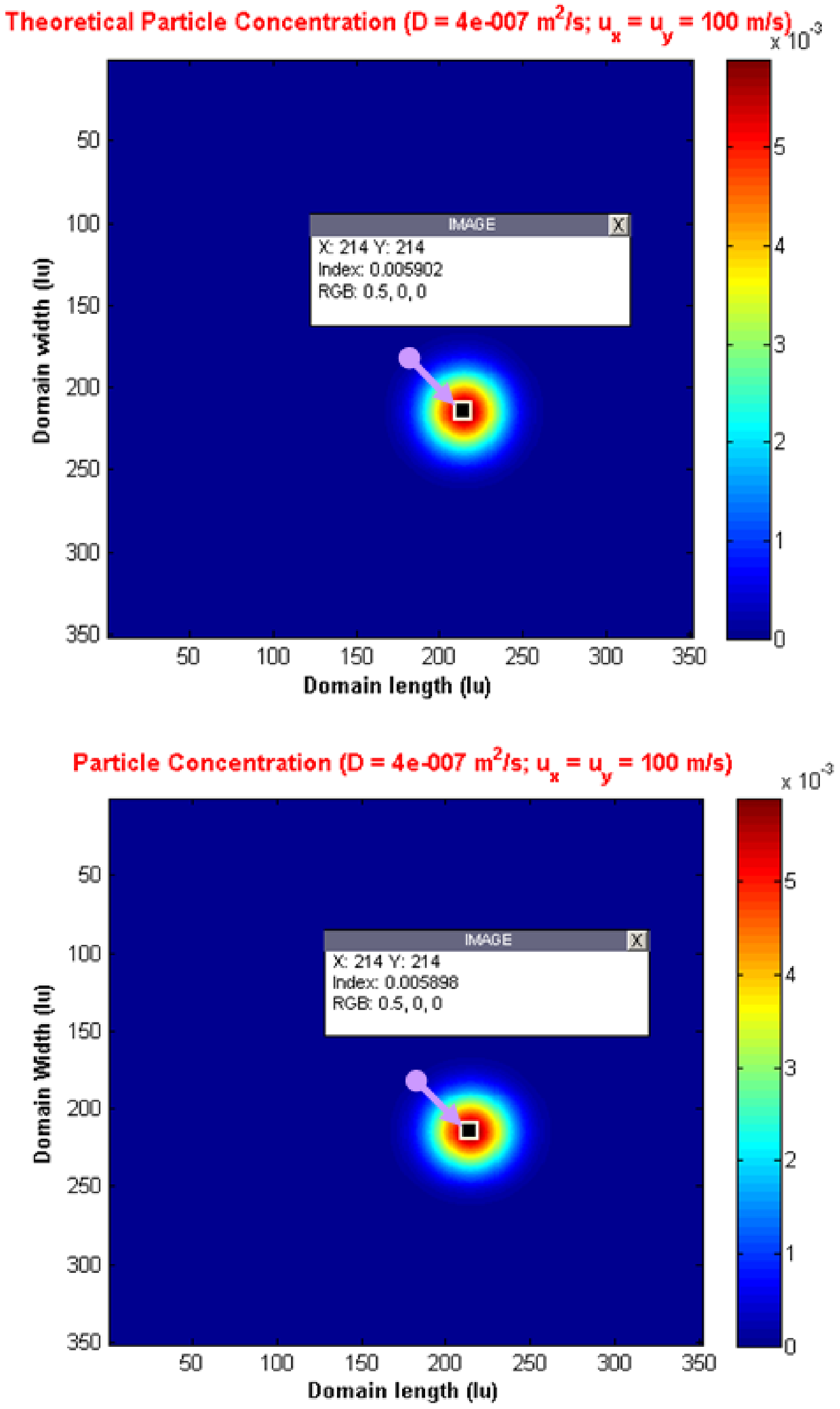

Figure 25. Concentration profiles of particles after 0.44 ns for a two-dimensional advection-diffusion of particles for corresponding to an instantaneous point source created at the center of the simulation domain at $t = 0$.(A) Theoretical plot and (B) LBM simulation.

Throughout the simulation domain, the fluid flow was initialized to $u = 200\ m/s$ for the one dimensional case and to $\boldsymbol{u} = [100\ 100]\ m/s$ for the two dimensional case and kept constant for the entire duration of the simulation. The fluid flow was not simulated explicitly in either of the cases. Initial concentration n_{init} of the solute was set to zero at $t = 0$ throughout the simulation domain for both the cases. The solute diffusion coefficient for the simulations was set to $D = 4 \times 10^{-7}\ m^2/s$ and the initial instantaneous non-dimensional point source concentrations for one and two dimensional simulations were set to $n_0 = 1$. The simulation results showed excellent agreement with the theoretical results obtained from equation (96) as shown in Figure 24 and Figure 25 A and B.

5.8. Surface chemical reaction in a microfluidic channel

Results from the previous section validated the LBM solver for the one and two dimensional advection-diffusion without any application of boundary conditions as such. However, for simulating the ionic electrodiffusion at the neuron-microelectrode interface one must be able to simulate particle fluxes across simulation domain boundaries or specify their concentration on them. Thus, to validate the Dirichlet and Neumann boundary conditions for particle concentrations on simulation domain boundaries, advection-diffusion of solute particles in a channel with a reacting wall boundary was carried out using the LBE (Eq. (61)).

5.8.1. Boundary Conditions

Similar to the advection-diffusion problems simulated in the previous section, the fluid flow in the channel was not explicitly simulated. Corresponding to no-slip boundary conditions for fluid flow on rough channel walls, a fully developed Hagen-Poiseuille flow with a parabolic flow velocity profile was initialized in the entire simulation domain at $t = 0$ and kept constant for the duration of the simulation (Figure 26).

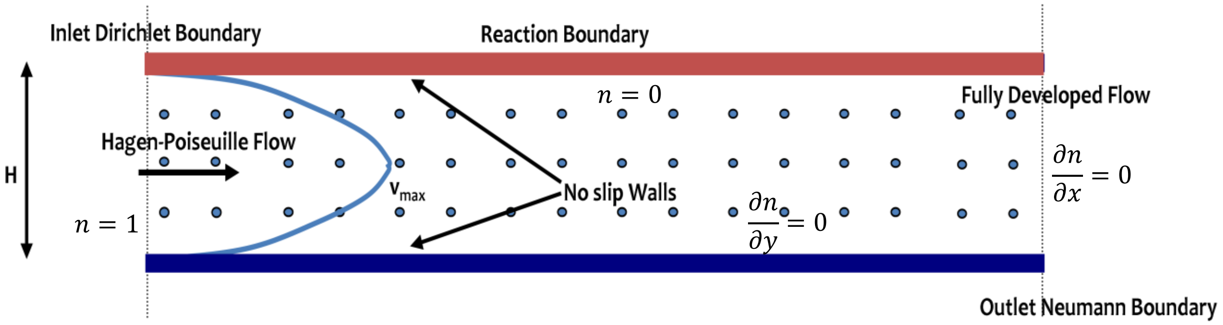
Inlet Dirichlet Boundary
Reaction Boundary
$n = 0$
Fully Developed Flow
Hagen-Poiseuille Flow
H
$\frac{\partial n}{\partial x} = 0$
$\mathrm{v}_{\max}$
No slip Walls
$n = 1$
$\frac{\partial n}{\partial y} = 0$
Outlet Neumann Boundary

Figure 26. A schematic depicting the boundary conditions on solute concentration and fluid flow for instantaneous surface chemical reaction on the upper wall of a microfluidic channel.

Observing that the non-equilibrium portion of the distribution function is proportional to the dot product of its microscopic velocity and the concentration gradient, the non-equilibrium portion in opposite directions must take an opposite sign [92]. Using this, the solute concentration at the inlet of the channel was specified as unity by computing the incoming distribution functions $f_{2,6,9}$ as

$$f_2 = -f_4 + f_2^{eq} + f_4^{eq} \tag{97}$$

$$f_6 = -f_8 + f_6^{eq} + f_8^{eq} \tag{98}$$

$$f_9 = -f_7 + f_9^{eq} + f_7^{eq} \tag{99}$$

where f_α^{eq} are given by equation (64). To account for the instantaneous reaction on the upper wall of the channel a Dirichlet boundary condition was implemented simply by setting all incoming distributions $f_{5,8,9}$ to zero which specified the solute concentration to be zero on the reaction wall boundary for all times. The non-dimensional diffusive flux is given by

$$\boldsymbol{j} = \sum_{\alpha} \boldsymbol{e}_{\alpha} f_{\alpha} \tag{100}$$

Using equations (100) and (64) and the assumption that the unknown distribution functions relax to equilibrium at the outlet boundary, as was done in section 5.5.2.1 for the electric potential, the Neumann boundary conditions on the lower channel wall and the channel outlet were set to no-diffusive flux.

5.8.2. Validation results

The LBM simulation results for the problem of surface chemical reaction in a microfluidic channel with a fully developed Hagen-Poiseuille flow were validated against simulations carried out in CFD-ACE+, a commercially available CFD solver. For simulations in CFD-ACE+, the Hagen-Poiseuille flow for the solvent was initialized in the simulation domain using results from a steady state simulation of the plain Poiseuille flow in a channel and the inlet boundary condition for the solvent flow was implemented using a user defined subroutine $\boldsymbol{ubound}$ written in FORTRAN. The surface chemical reaction in a microfluidic channel of dimensions $1 \times 4\ \mu m$ was simulated using the flow and chemistry modules of CFD-ACE+. The initial solute concentration in the simulation domain was set to zero for both of LBM and CFD-ACE+ simulations and a solute diffusion coefficient of $D = 4 \times 10^{-7}\ m^2/s$ was employed for all simulations. The simulations were carried out for Peclet numbers ($Pe \equiv u_{max}h/D$) of 0.125, 25 and 250. The LBM results were compared with CFD-ACE+ simulations for the steady state and an excellent match was obtained (Figure 27 and Figure 28).

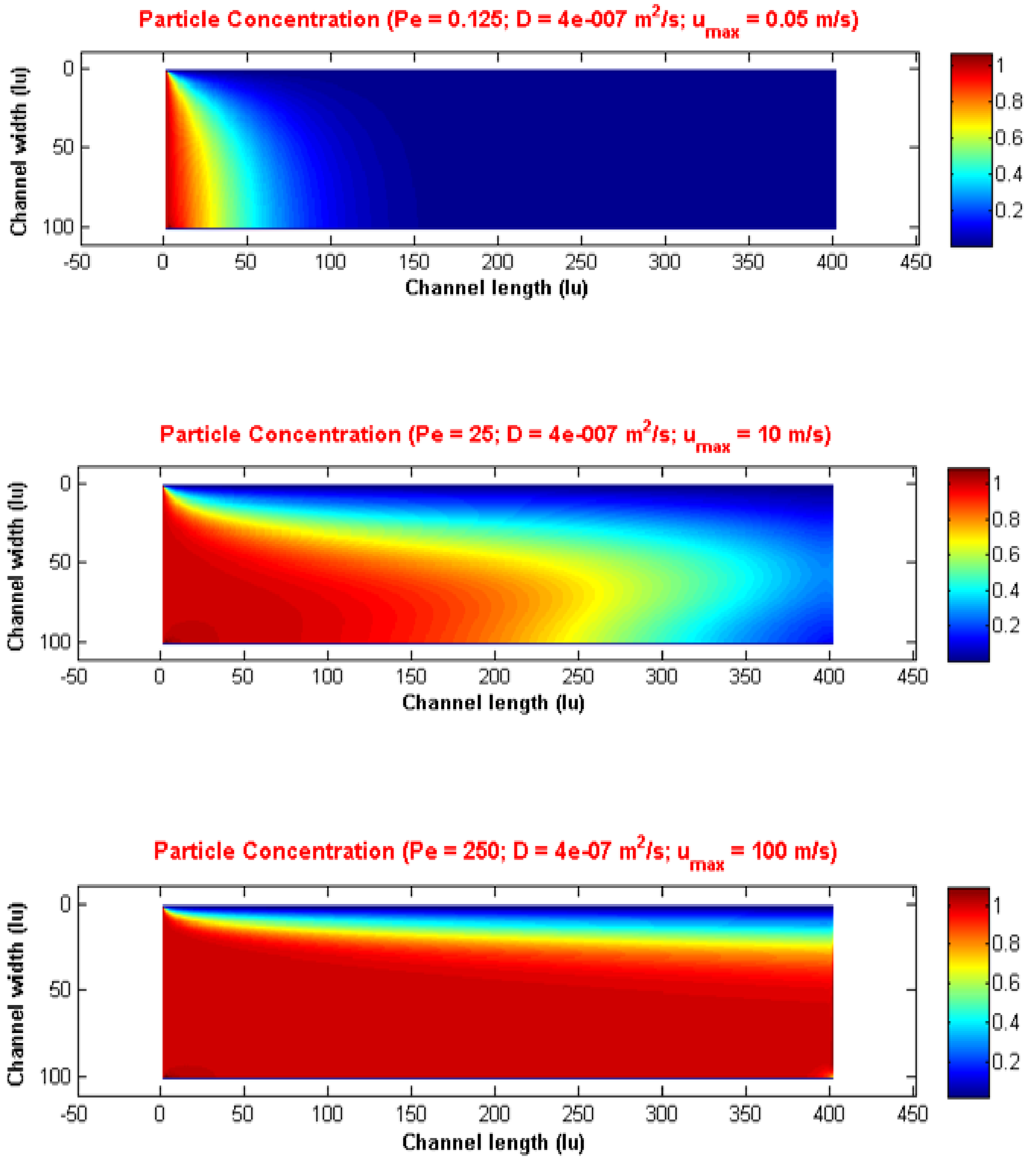

Figure 27. LBM simulation results for solute concentration profiles as a function of different Peclet numbers in a microfluidic channel with instantaneous chemical reaction on the upper wall that fixes the solute concentration to zero for all times on the reaction wall

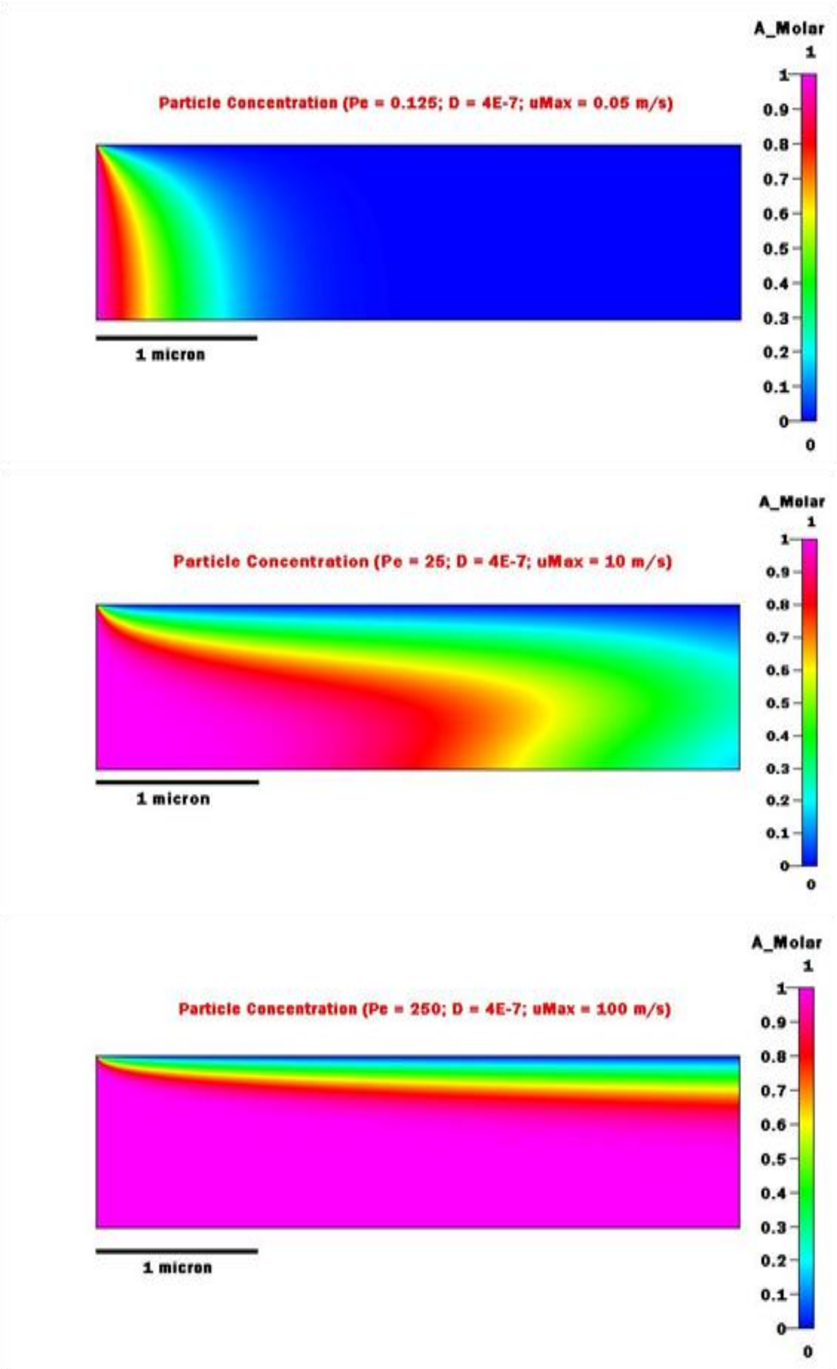

Figure 28. Results obtained using the commercially available multiphysics solver CFD-ACE+ for solute concentration profiles as a function of different Peclet numbers in a microfluidic channel with instantaneous chemical reaction on the upper wall that fixes the solute concentration to zero for all times on the reaction wall

5.9. Molecular speed dependent relaxation time – Entrance flow problem revisited

The lattice Boltzmann equation (61) makes use of a single relaxation time approximation referred to in the LBM literature as the Bhatnagar-Gross-Krook or BGK approximation [85]. Although the use of a single relaxation time in the LBE (61) simplifies computation, the simplification comes at the cost of stability of the LB algorithm. This is can be seen clearly from the case of the entrance flow problem as the assumption of a single relaxation time leads to an unphysical situation. The hydrodynamic pressure close to the point of transition from a free-slip boundary condition to a no-slip boundary condition for the fluid flow on the channel walls is higher than it is at the center of the channel at the same position along the x-axis (Figure 20 B) but, despite the pressure being higher closer to the point of transition in the boundary conditions, the fluid close to the walls is forced to relax, by virtue of the BGK approximation, at the same rate as the fluid at the center of the channel. A physically correct description, therefore, must have a higher rate of relaxation for the fluid in a region of higher pressure than in a region of lower pressure. Also, it is worth noting that the flow speed closer to the point of transition in boundary conditions from free-slip to no-slip in a region of higher pressure is lower than it is at the center of the channel where the hydrodynamic pressure is lower (Figure 20 B). Thus, with the aim of obtaining a physically correct description of microscopic phenomena, this section presents results from a lattice Boltzmann algorithm that makes use of a molecular speed dependent relaxation time in the LBE (61).

5.9.1. Molecular speed dependent relaxation time

In equation (68), the relaxation time τ_v involves the kinematic viscosity ν of the fluid. Based on kinetic theory, the kinematic viscosity ν^{eq} of a fluid is given by [93]

$$\nu^{eq} = \frac{1}{3}\bar{c}l \tag{101}$$

where $\bar{c} = \sqrt{8kT/\pi m_p}$ is the mean thermal speed of the particles, l their mean free path and m_p their molecular mass. The macroscopic velocity $\boldsymbol{u}$ of the fluid also represents a statistical average of the net microscopic velocity of the fluid particles. As such, at any given point in the simulation domain the average speed c of the particles can be written as the sum of the molecular speed $\bar{c}$ due to random Brownian motion and the magnitude of the macroscopic velocity $\boldsymbol{u}(\boldsymbol{r}, t)$**,** i.e.

$$c(r,t) = \bar{c} + u(r,t) \tag{102}$$

Based on equation (102), the local kinematic viscosity $\nu'(r,t)$ can then be written as

$$\nu'(r,t) \equiv \frac{1}{3}c(r,t)l'(c) \tag{103}$$

where $l'(c)$ is the local mean free path that depends on the local mean speed of the particles. Since the local macroscopic velocity $\boldsymbol{u}(\boldsymbol{r}, t)$ can be computed easily using equation (63) in the LB algorithm and the mean thermal speed $\bar{c}$ can be computed if molecular mass m_p and the temperature T of the system are known, the problem of computing a molecular speed dependent relaxation time now reduces to getting an estimate of the local mean free path $l'(c)$. This can be accomplished through a use of the Tait's theory of mean free path by turning again to the kinetic theory of gases with the underlying assumption that there are sufficient numbers of collisions in the system to allow for the existence of a local Maxwellian distribution of particle velocities [94].

The number of collisions occurring in the time interval dt between pairs of molecules m_1 and m_2 can be written as

$$dt\frac{1}{4}f_1f_2c_rd_{12}^2sin\chi d\chi d\epsilon d\boldsymbol{c_1}d\boldsymbol{c_2} \tag{104}$$

such that $\boldsymbol{c_1}$, $\boldsymbol{c_2}$, χ and ϵ lie in the ranges and $d\boldsymbol{c_1}$, $d\boldsymbol{c_2}$, $d\chi$ and $d\epsilon$ respectively. Here, $\boldsymbol{c_1}$, $\boldsymbol{c_2}$ are the particle velocities; c_r is the magnitude of the relative velocity ($\boldsymbol{c_{21}} = \boldsymbol{c_2} - \boldsymbol{c_1}$) of the particles; χ is the angle of scattering between the relative velocity $\boldsymbol{c_{21}}$ before collision and $\boldsymbol{c_{21}}'$ after collision; $d_{12}$is the average diameter of the molecules of two types; and, ϵ is the angle between the plane LMN and AP' (Figure 29). f_1 and $f_2$are the single particle velocity distribution functions given by

$$f_i = n_i\left(\frac{m_i}{2\pi kT}\right)^{3/2}exp\left(\frac{-m_ic_i^2}{2kT}\right); i = 1, 2 \tag{105}$$

where n_i is the number density of the ith type of molecules. The total number of these collisions such that $\boldsymbol{c_1}$ lies between $\boldsymbol{c_1}$ and $\boldsymbol{c_1} + d\boldsymbol{c_1}$ can be obtained by integrating over all values of $\boldsymbol{c_2}$, χ and ϵ. Denoting the total number of such collisions by

$$P_{12}(c_1)f_1d\boldsymbol{c_1}dt \tag{106}$$

where $P_{12}(c_1)$ signifies the average number of collisions per unit time (or collision frequency) per molecule of speed $c_1$with the molecules of mass m_2.

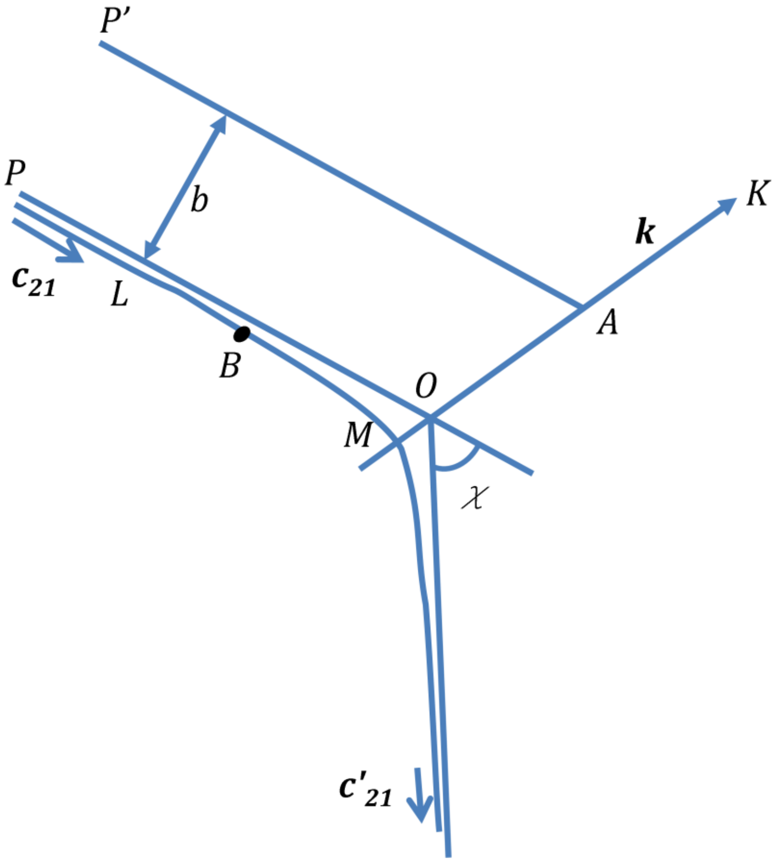

Figure 29. Representation of a binary collision between two molecules in the center of mass frame.

Division by $f_1 d\boldsymbol{c_1} dt$ and comparison with equation (104) gives

$$P_{12}(c_1) = \frac{1}{4} \iiint f_2 c_r d_{12}^2 sin\chi d\chi d\epsilon d\boldsymbol{c_2} \tag{107}$$

Integrating equation (107) with respect to χ, ϵ and $\boldsymbol{c_2}$, we get

$$P_{12}(c_1) = n_2 d_{12}^2 \sqrt{\frac{2\pi kT}{m_2}} \left(e^{-x^2} + 2x + \frac{1}{x} \right) Erf(x) \tag{108}$$

where $x = c_1\sqrt{m_2/2kT}$ and Erf denotes the un-normalized error function. The collision frequency $P_{11}(c_1)$ of collisions of a molecule of type 1 with molecules of its own kind can also be written with a similar expression. In general, frequency of collisions of molecules of type 1 with molecules of type i is given by

$$P_{1i}(c_1(r,t)) = n_i(r,t) d_{1i}^2 \sqrt{\frac{2\pi kT}{m_i}} \left(e^{-{x_i}^2} + 2x_i + \frac{1}{x_i} \right) Erf(x_i) \tag{109}$$

where $x_i = c_1\sqrt{m_i/2kT}$ and d_{1i} is the average molecular diameter of the molecules of type 1 and type i. Thus, the total collision frequency for molecules of type 1 moving with speed c_1 is given by

$$P_1(c_1) = \sum_i P_{1i} = \frac{1}{\tau_1(c_1)} \tag{110}$$

where τ_1 is the characteristic collision interval. The length of the mean free paths of molecules of type 1 moving with speeds c_1 is thus given by

$$l_1(c_1) = c_1\tau_1(c_1) = \frac{c_1}{\sum_i P_{1i}} \tag{111}$$

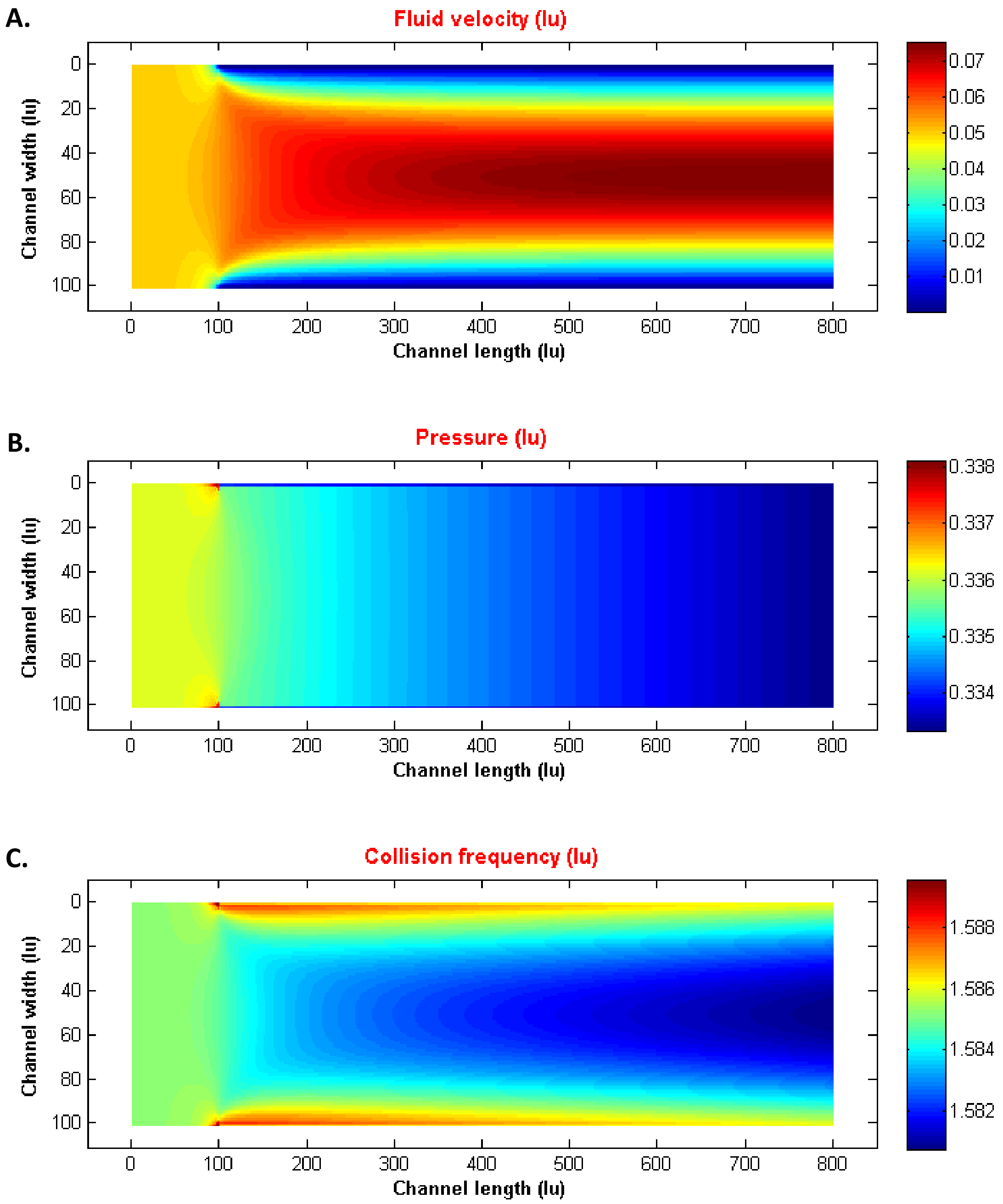

Figure 30. Poiseuille flow in a microfluidic channel computed using a molecular speed dependent relaxation time based LBM algorithm. (A) Fluid velocity, (B) Pressure gradient and (C) Non-dimensional collision frequency.

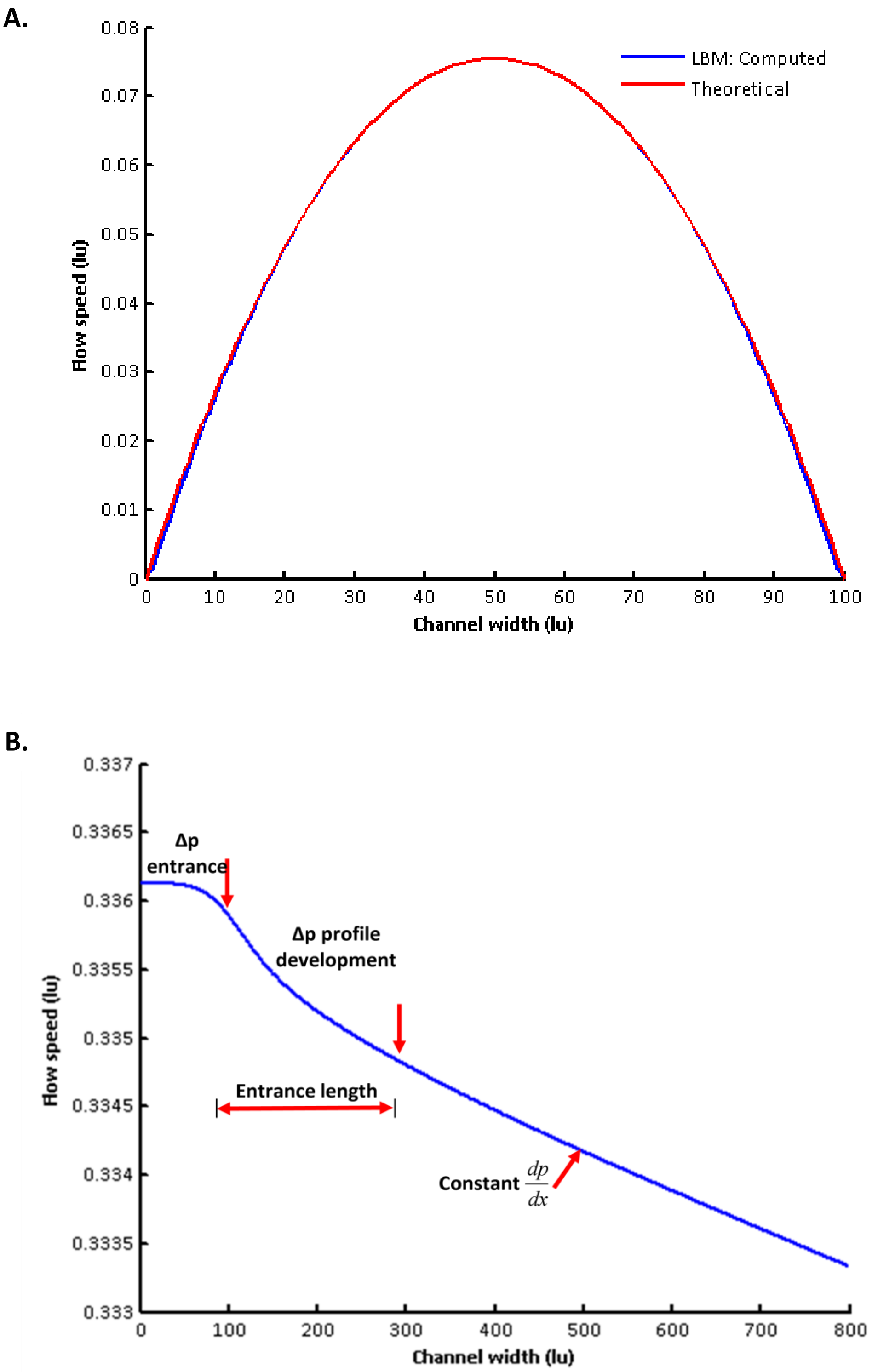

Figure 31. Poiseuille flow in a microfluidic channel computed using a molecular speed dependent relaxation time based LBM algorithm. (A) Steady state parabolic flow profile across the width of the channel. (B) Pressure gradient along the length of the channel for a fully developed Poiseuille flow.

Substituting the value for the mean free path in equation (103), one obtains the local kinematic viscosity of the fluid as

$$\nu'(r,t) \equiv \frac{1}{3}\frac{c_1^2(r,t)}{\sum_i P_{1i}} \qquad (112)$$

This can now be used with equation (68) to compute a local non-dimensional relaxation time for the LB algorithm.

5.9.2. Validation results

The formalism for the molecular speed dependent relaxation time was validated by simulating the entrance flow problem described in section 5.4.1 again. The mass of the fluid particles was specified as $m_f = 18.015\, amu$; temperature as $T = 298\, K$; density as $\rho_f = 996.25\, kg/m^3$; and, diameter as $d_f = 1.92\, A$. The non dimensional flow velocity at the inlet was specified as $\boldsymbol{u_{in}} = [0.05\ 0]$ as in the previous simulation (section 5.4.3) for the validation of the hydrodynamic LB solver. Figure 30 A, B and C show the flow velocity, pressure and the molecular speed dependent non-dimensional collision frequency respectively. A comparison of Figure 30 B and C shows clearly that, as expected, the non-dimensional collision frequency $\omega_f(r,t)$ is higher in regions of higher pressure and lower velocity and vice versa. The molecular speed dependent relaxation time thus helps recover the correct physical description of the microscopic phenomena which was not possible with the BGK approximation. The flow velocity profile across the width of the channel at the outlet matched the theoretical parabolic profile for the Poiseuille flow well (Figure 31 A) and the pressure gradient along the length of the channel also matched the simulation results from the single relaxation time BGK approximation (Figure 31 B and Figure 21 B).

5.9.3. Discussion

Besides the molecular speed dependent relaxation time model proposed in this chapter for the LBE and the single relaxation time lattice Bhatnagar-Gross-Krook (SRT or LBGK) model employed for the development of the LBM based multiphysics solver, there are several other variants for the relaxation time models that include the multiple relaxation time (MRT), two relaxation time (TRT) and the entropic lattice Boltzmann equation (ELBE) models [95, 96]. All these models have been developed as an alternative to the LBGK model to improve the numerical stability of the LBE. MRT models are constructed in the moment space rather than the velocity space and approximate the collision process as linear relaxations in the moment space. Corresponding to the nine discrete velocities in the D2Q9 model, nine moments are defined of which the ones corresponding to the density and the x and y components of the flux are conserved and the rest are unconserved. In the diagonal matrix for the relaxation times, the three relaxation times related to the conserved moments are set to zero while the ones related to the unconserved moments are computed from the constant bulk and shear viscosities. Now, if the relaxation rates for the even order moments are fixed to $1/\tau$, the relaxation rates for the odd order moments are equal and can be computed in terms of the shear viscosity. This then reduces the MRT model to a TRT model. Further, if the odd order moments are also fixed to $1/\tau$, then the TRT model reduces to the SRT or the LBGK model. Recently, it has been shown by Luo et al that among all the variants of the relaxation time models, including the ELBE model, the MRT model performs the best in terms of numerical stability because it employs a greater number of relaxation times than the TRT and the LBGK models for the LBE. They also show that since ELBE models employ just a single relaxation time, they perform as poorly as the LBGK models in terms of stability [96].

The molecular speed dependent relaxation time model proposed here in this chapter admits a continuously varying relaxation time based on the local speeds of the fluid or solute particles. Thus, presumably, a LBE based on the molecular speed dependent relaxation time ought to be more stable than all the other relaxation time models proposed so far, although no stability studies are being reported here to support this assertion. Additionally, the use of a molecular speed dependent relaxation time preserves the simplicity and elegance of the single relaxation time LBGK models.

5.10. Conclusions

In conclusion, this chapter describes the development of a LBM based multiphysics solver aimed at the simulation of ionic electrodiffusion in mesoscale systems in a systematic step-by-step fashion by resolving the development process into tractable parts. Each of these sub-components of the multiphysics solver is validated with the solution of a model test problem through a comparison with either a known theoretical solution or against published literature. This chapter also describes a molecular speed dependent relaxation time model for the LBE which is validated with the simulation of results for the entrance flow problem. Unlike the single relaxation time LBGK model, this model recovers the correct description of microscopic phenomena of collision frequency variation with pressure gradients in the entrance flow problem.

CHAPTER-6: SIMULATION OF IONIC ELECTRODIFFUSION AT MESOSCALE INTERFACES

6.1. Introduction

Chapter 5 presented results from the development of an LBM based multiphysics solver and put in place a framework that can now be exploited for the simulation of the transient dynamics of mesoscale electrochemical systems.

The electrical coupling between the neuron and the microelectrode at the neuroelectronic junction is a capacitive coupling as the extracellular recording amplifier for the microelectrode arrays is a high-input-impedance-high-gain amplifier that draws a negligible ionic current from the neuron-microelectrode junction. Therefore, for the simulation of transient ionic electrodiffusion at the mesoscale neuron-electrode junction under the influence of neuron driven ionic currents and potentials, a primary requirement for a multiphysics solver is the capability to simulate the transient dynamics of a capacitive coupling between two plane parallel electrodes with overlapping electric double layers between them. This chapter, thus, presents results from the simulations for the charge relaxation dynamics of an electrolytic nanocapacitor using fully coupled LPBM solver for the Poisson's equation with the LBE for the ionic electrodiffusion that employs a molecular speed dependent relaxation time.

6.2. Theory

For simulating the dynamics of the electrolytic nanocapacitor, a primitive model of a symmetric $1:1$ electrolyte was considered. The primitive model of an electrolyte describes the ions in the solvent as point particles and includes the effect of the solvent by describing it as a background medium with a characteristic dielectric constant and a constant density. As such, the dynamics of the solvent were excluded from the simulations. However, for the purposes of computing the molecular speed dependent relaxation times for the time evolution of the ionic distribution functions on the lattice, hydrated ions with an effective mass and finite diameter were considered. Based on kinetic theory, just as in the case of the fluid viscosity ν (101), the equilibrium ionic diffusion coefficients D_i^{eq} for the ith ionic specie can be calculated using [93]

$$D_i^{eq} = \frac{1}{3}\overline{c_\iota}\,\overline{l_\iota}(\overline{c_\iota}) \tag{113}$$

where $\overline{c_\iota} = \sqrt{8kT/\pi m_i}$ is the mean thermal speed of the ions at equilibrium, m_i is the effective ionic mass, $\overline{l_\iota}$ is the equilibrium mean free path for the ith ionic specie that can be computed using equations (109) and (110) described in chapter 5 (section 5.9.1) and rewritten here as

$$P_{1i}(\overline{c_1}(r,t)) = n_i(r,t)d_{1i}^2\sqrt{\frac{2\pi kT}{m_i}}\left(e^{-x_i{}^2} + 2x_i + \frac{1}{x_i}\right)Erf(x_i) \tag{114}$$

where $x_i = \overline{c_1}\sqrt{m_i/2kT}$ and $i = 1, 2 \text{ and } 3$ corresponds to cation, anion and the solvent molecules. Thus, the total collision frequency for ions of type 1 moving with speed c_1 is given by

$$P_1(\overline{c_1}) = \sum_i P_{1i} = \frac{1}{\tau_1(\overline{c_1})} \tag{115}$$

where τ_1 is the characteristic collision interval. The length of the mean free path of ions of type 1 moving with speed c_1 is thus given by

$$l_1(\bar{c_1}) = \bar{c_1}\tau_1(\bar{c_1}) = \frac{\bar{c_1}}{\sum_i P_{1i}} \tag{116}$$

Substituting equations (114) and (116) in equation (113) shows that the equilibrium ionic diffusion coefficients D_i^{eq} depend on the densities of the ions and the solvent as also on their diameters. Thus, if the equilibrium diffusion coefficients D_i^{eq} along with the densities of the components of the electrolyte mixture and the diameter of the solvent molecules are prescribed for a simulation, the diameters for the ions d_i would need to be computed through a set of coupled quadratic equations. This was accomplished numerically through the use of iterative Newton-Raphson method.

The LPBM solver described in Chapter 5 (section 5.5) was employed to solve for the electric potential and field at every time step of the simulation to account for a change in the distribution of ions on the lattice in response to the applied electric field. The time evolution of the ionic distribution functions $f_{i,\alpha}$ on a two dimensional nine velocity D2Q9 lattice was computed using the following lattice Boltzmann equation (LBE) given below

$$f_{i,\alpha}(\boldsymbol{r} + \boldsymbol{e}_\alpha \Delta t, t + \Delta t) = f_{i,\alpha}(\boldsymbol{r}, t) - \frac{f_{i,\alpha}(\boldsymbol{r}, t) - {f_{i,\alpha}}^{eq}(\boldsymbol{r}, t)}{\tau_i} + \Delta t F_i \tag{117}$$

where τ_i is the non-dimensional molecular speed dependent relaxation time, $\boldsymbol{e}_\alpha$ are the discrete particle velocities given by equation (67). The discrete external force term F_i is given by [97]

$$F_i = \left(1 - \frac{1}{2\tau_i}\right)\left[\frac{\boldsymbol{e}_\alpha - \boldsymbol{u_i}}{RT} + \frac{\boldsymbol{e}_\alpha \cdot \boldsymbol{u_i}}{(RT)^2}\right] \cdot [z_i e\boldsymbol{E} - 3\pi d_i \phi_i \mu_{solv}(\boldsymbol{u_i} - \boldsymbol{u_{solv}})]{f_{i,\alpha}}^{eq} \tag{118}$$

where $\boldsymbol{E}$ is the electric field; $\boldsymbol{u_i}$ the ionic velocity; $\boldsymbol{u_{solv}}$ and μ_{solv} are the flow velocity and the dynamic viscosity of the solvent respectively; and ϕ_i is the number fraction of the ions of the ith type in the electrolyte mixture. Since, with the use of a primitive model for the electrolyte the solvent dynamics were excluded from the simulations, the solvent velocity $\boldsymbol{u_{solv}}$ was approximated to zero. The first and the second terms in the second square brackets in equation (121) represented the electric and the viscous drag forces on the ions respectively. The molecular speed dependent relaxation time τ_i was computed using

$$\tau_i = 3D_i(r,t)\frac{\Delta t}{\Delta x^2} + 0.5 \tag{119}$$

with $D_i(r,t)$ given by

$$D_i(r,t) = \frac{1}{3}c_i(r,t)l_i(c_i) \tag{120}$$

where $c(r,t) = \overline{c_i} + u_i(r,t)$ and $l_i(c_i)$ can be computed using equations (109), (110) and (111).

The equilibrium distribution functions for each ion type were computed using equation (64). The macroscopic ionic concentrations n_i and the momentum densities were then given by

$$n_i = \sum_\alpha f_{i,\alpha} = \sum_\alpha f_{i,\alpha}^{eq} \tag{121}$$

$$n_i\boldsymbol{u_i} = \sum_\alpha \boldsymbol{e}_\alpha f_{i,\alpha} + \frac{\Delta t}{2}\boldsymbol{F_i} \tag{122}$$

where $\boldsymbol{F_i}$ is the force on the ith ion type given by

$$\boldsymbol{F_i} = \boldsymbol{F_{electric}} + \boldsymbol{F_{visc}} = z_i n_i e\boldsymbol{E} - 3\pi n_i d_i \phi_i \mu_{solv} \boldsymbol{u_i} \tag{123}$$

The equation (122) for the momentum densities for the ions was modified from equation (63) to include the additional force term to account for the spatially varying nature of the force field in the simulations for the electrolytic nanocapacitor [97]. Also, global electroneutrality of the electrolyte was enforced at each time step to account for round-off errors over long simulation runs.

6.3. Boundary Conditions

Dirichlet boundary conditions were applied for the electric potential V_e on the electrode surfaces using the method described in section 5.5.2 such that

$$V_e = \pm V \text{ for all } t \geq 0 \tag{124}$$

while no-flux boundary conditions were applied for the ions on the electrode surfaces using equation (122) to simulate perfectly blocking electrodes. Periodic boundary conditions were applied on the simulation domain boundaries perpendicular to the electrode surfaces for all distribution functions used in LPBM and LBE for the simulation of ionic electrodiffusion.

6.4. Results

At $t = 0$, an initial condition of linearly varying electric potential from $+10\ mV$ at the cathode to $-10\ mV$ at the anode was specified throughout the simulation domain. A lattice spacing of $\Delta x = 0.5\ A$ corresponding to a simulation time step of $\Delta t = 0.58\ ps$ was employed for all simulations. For electrode spacings of $h = 50\ nm$ and $h = 100\ nm$ at $t = 0$, ions in the electrolyte experienced an initial electric field of $E_y = 4 \times 10^5$ and $E_y = 2 \times 10^5\, V/m$ respectively. This resulted in electric force acting on the cations and anions in the electrolyte causing them to move towards the electrodes of opposite polarities. To study the subsequent relaxation dynamics of the ions in the region between the two electrodes, simulations were carried out for various degrees of electric double layer (EDL) overlap (defined by $\alpha = 10\lambda_D/h$, where λ_D is the Debye length given by equation (91)), solvent viscosity μ_{solv}, electrode separations of 50 and 100 nm and cation to anion diffusion coefficient ratios of $1{:}\,1$and $2{:}\,1$.

The anion diffusion coefficient was specified as $D_{an} = 4 \times 10^{-9}\, m^2/s$ or $D_{an} = 2 \times 10^{-9}\, m^2/s$ depending on the diffusion coefficient ratio while the cation diffusion coefficient was fixed at $D_{cn} = 4 \times 10^{-9}\, m^2/s$. Since the electrode spacing for almost all simulations was fixed at $h = 50\, nm$, the EDL overlap parameter was varied to $\alpha = 1.4,\ 0.9,\ 0.65, 0.2 \text{ or } 0.1$ by varying bulk electrolyte concentrations to $n^b = 1.89, 4.57, 8.76, 92.54 \text{ or } 370.19\, mM$ respectively. The effect of electrode spacing was studied by changing h to $100\, nm$ while keeping the electrolyte concentration fixed. The temperature for all simulations was fixed at $T = 298\, K$; solvent molecular mass m_{solv} and density ρ_{solv} were fixed at $18.015\, amu$ and $1000\, kg/m^3$ respectively; molecular masses of hydrated ions were fixed at $113.065\, amu$ corresponding to five molecular masses of the solvent molecule in the hydration shell and an ionic mass of $m_{ion} = 22.99\, amu$. Corresponding to these conditions, the ionic diameters for the two anion to cation diffusion coefficient ratios of $1{:}\,1$and $2{:}\,1$ were obtained from the Newon-Raphson method based iterative solution of the coupled quadratic equations described in section 6.2 as $d_{cn} = d_{an} \approx 3.48\, A$ and $d_{cn} \approx 3.48\, A;\ d_{an} \approx 5.71\, A$ respectively.

6.4.1. Spatially averaged current density J_{avg}

To understand the global effect of various parameters outlined above on the charge relaxation dynamics of the electrolytic nanocapacitor, the variation of spatially averaged total current densities as a function of time was first plotted and analyzed.

6.4.1.1. Effect of overlapping electric double layers and solvent viscosity

The effect of overlapping electric double layers and solvent viscosity on the spatially averaged current density J_{avg} is depicted in Figure 32 through Figure 34. It can be seen through these figures that, as the degree of EDL overlap is reduced from $\alpha = 1.4$ to $\alpha = 0.65$ and then to $\alpha = 0.1$, the behavior of the spatially averaged current density changes gradually from oscillatory to monotonic accompanied by a decrease in the maximum amplitude.

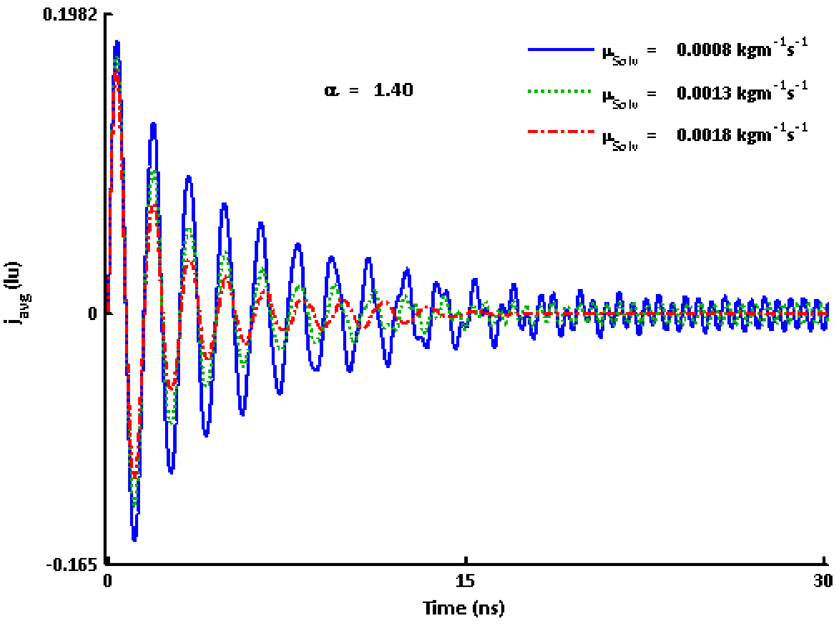

Figure 32. Effect of solvent viscosity μ_{solv} on the spatially averaged current density for an electric double layer overlap of $\alpha = 1.4$.

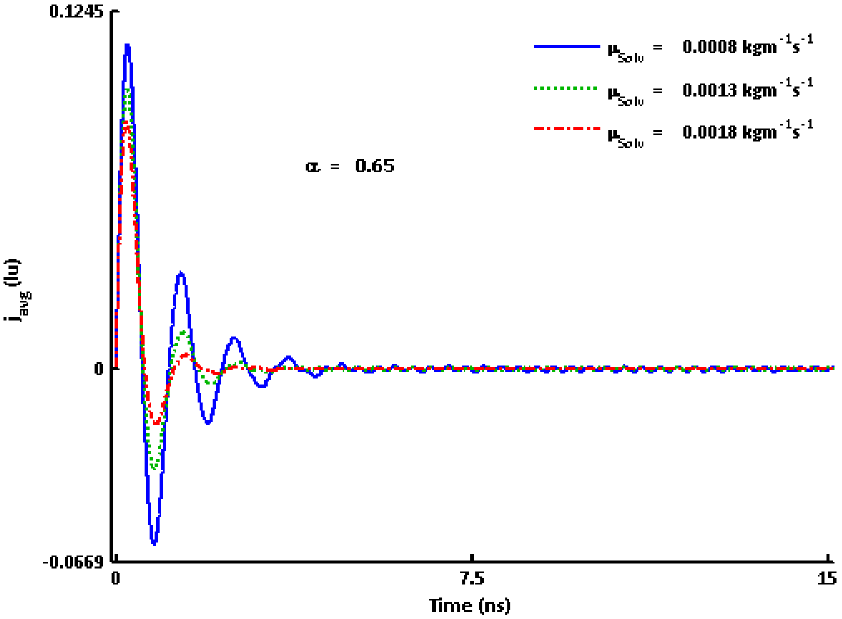

Figure 33. Effect of solvent viscosity μ_{solv} on the spatially averaged current density for an electric double layer overlap of $\alpha = 0.65$.

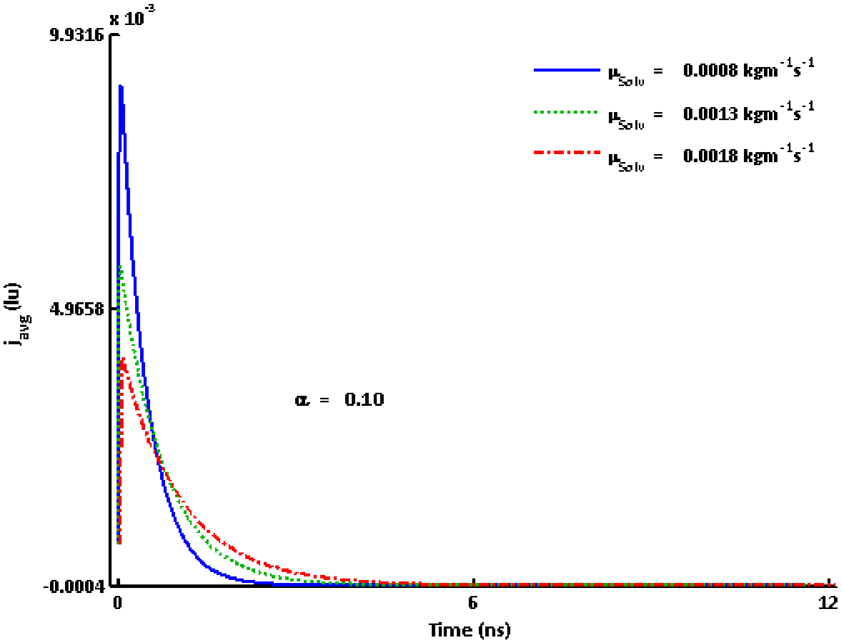

Figure 34. Effect of solvent viscosity μ_{solv} on the spatially averaged current density for an electric double layer overlap of $\alpha = 0.1$.

The effect of increase in solvent viscosity μ_{solv} in going from $0.0008\,kgm^{-1}s^{-1}$ to $0.0018\,kgm^{-1}s^{-1}$ is to dampen the oscillatory behavior for $\alpha = 1.4$ and $\alpha = 0.65$ (Figure 32 and Figure 33) and reduce the amplitude of the oscillations while it increases the relaxation time to equilibrium for the spatially averaged current density in the case of $\alpha = 0.1$ (Figure 34). Also, it is observed that the oscillatory behavior in the case of EDL overlap of 1.4 and 0.65 persists for solvent viscosities of $0.0008\,kgm^{-1}s^{-1}$ and $0.0013\,kgm^{-1}s^{-1}$ much longer than what might be expected (Figure 32 and Figure 33).

6.4.1.2. Effect of ratio of ionic diffusion coefficients

The effect of ratio of cation to anion diffusion coefficients for a solvent viscosity of $0.0018\,kgm^{-1}s^{-1}$ on J_{avg} is shown in Figure 35 and Figure 36.

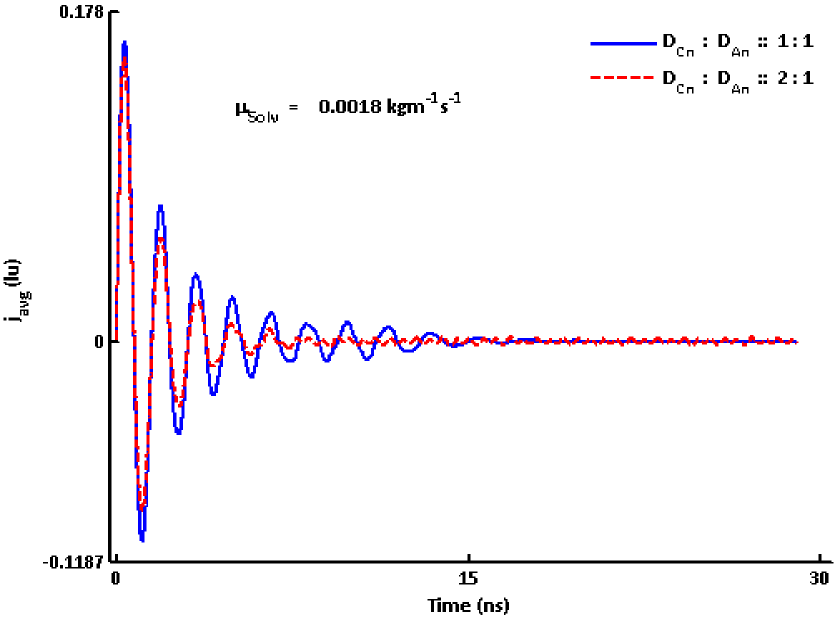

Figure 35. Effect of cation to anion diffusion coefficient ratio on spatially averaged current density for $\alpha = 1.4$.

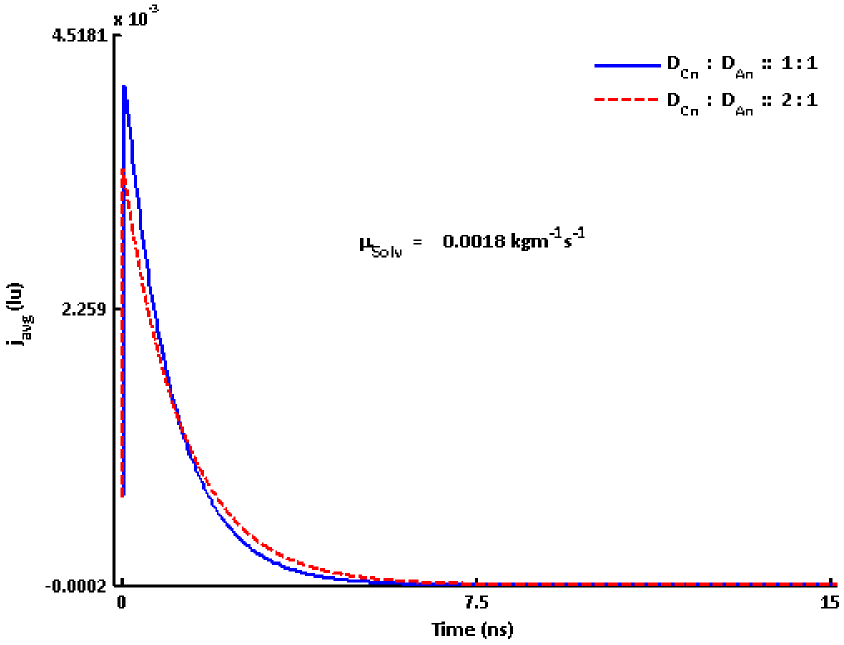

Figure 36. Effect of cation to anion diffusion coefficient ratio on spatially averaged current density for $\alpha = 0.1$.

Since the cation diffusion coefficient is fixed at $D_{cn} = 4 \times 10^{-9}\, m^2/s$ for both $1{:}1$ and $2{:}1$ cases, changing the cation to anion diffusion coefficient ratio from $1{:}1$ to $2{:}1$ has the effect of reducing the anion diffusion coefficient by half. For both $\alpha = 1.4$ and $\alpha = 0.1$, this reduces the amplitude of J_{avg} and a slight increase in relaxation time is seen for $\alpha = 0.1$. It also introduces very small amplitude persistent oscillations, almost imperceptible, in the case of EDL overlap of 1.4 as J_{avg} never really goes to zero completely like the curve for the diffusion coefficient ratio of $1{:}1$. Thus, it introduces oscillatory behavior in J_{avg}.

6.4.1.3. Effect of electrode separation

The effect of increasing electrode separation from $h = 50\, nm$ to $h = 100\, nm$ was to again decrease the maximum amplitude of J_{avg} for both bulk ionic concentrations of $n_b = 4.6\, mM$ and $n_b = 92.5\, mM$ as can be seen in Figure 37 and Figure 38.

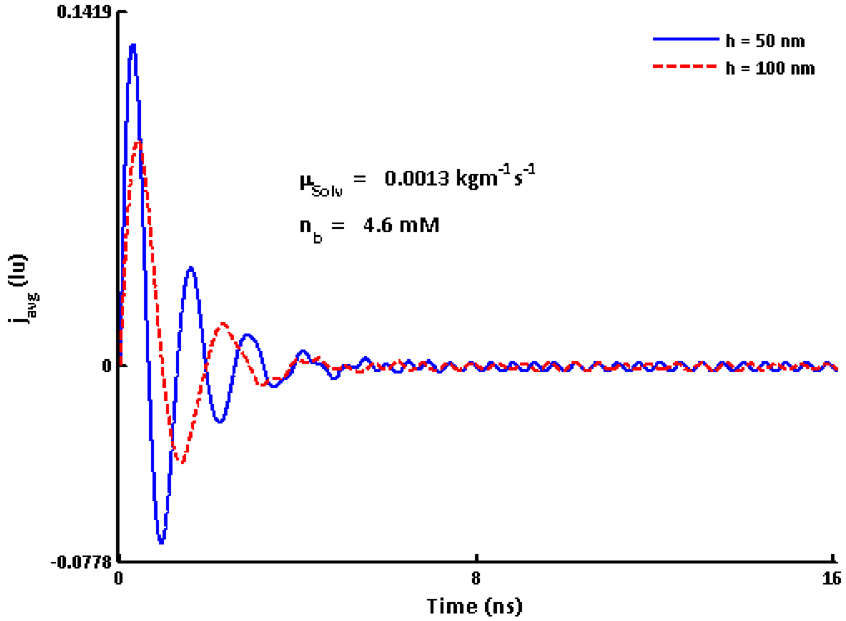

Figure 37. Effect of electrode separation on the spatially averaged current density for bulk electrolyte concentration of $n_b = 4.6$ mM.

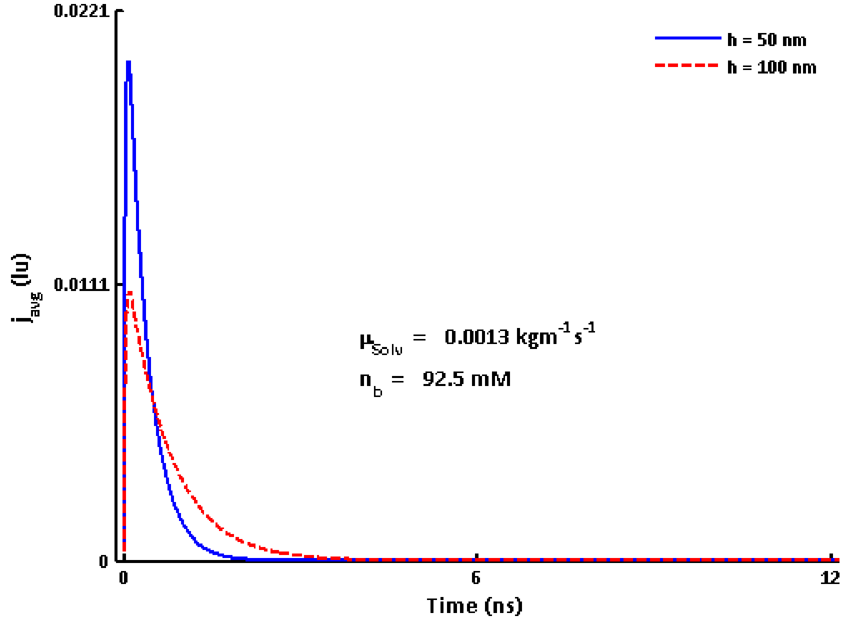

Figure 38. Effect of electrode separation on the spatially averaged current density for bulk electrolyte concentration of $n_b = 92.5$ mM.

The maximum value for J_{avg} in the case of $n_b = 92.5\ mM$ and $h = 100\ nm$ decreased to about half of its value in $h = 50\ nm$. Doubling the electrode separation also increased the period of oscillations in J_{avg} by a factor of ~1.5-2.0 for $n_b = 4.6\ mM$ and doubled the relaxation time to equilibrium for $n_b = 92.5\ mM$.

6.4.1.4. Summary and discussion

In terms of underlying physics, the decrease in maximum value of J_{avg} in the cases of increasing solvent viscosity μ_{solv} (Figure 32 through Figure 34) and a reduction of the anionic diffusion coefficient D_{an} by half (Figure 35 and Figure 36) are similar and result from a reduction in the mobility of ions as both viscosity and diffusion coefficient are related to each other and mobility through the Nernst-Einstein and Stokes-Einstein relations given by

$$D_i = \frac{\mu_i kT}{z_i e} = \frac{kT}{3\pi d_i \mu_{solv}} \tag{125}$$

A decrease in ionic mobility due to increased viscosity or reduced diffusion coefficient, therefore, leads to a decreased conductivity of the electrolytic medium between the capacitor electrodes resulting in an increase in the potential drop across the electrolyte which is then accompanied by a consequent decrease in the maximum value of the spatially averaged current density J_{avg}. This also explains faster relaxation to equilibrium for the monotonic case of $\alpha = 0.1$ (Figure 34) with decreasing viscosity of the solvent as more mobile ions charge up the electrodes faster. In case of $\alpha = 1.4$ and $\alpha = 0.65$, a decrease in viscosity and the consequent increase in ionic mobility causes the ions to oscillate longer (Figure 32 and Figure 33).

The origins of a decrease in amplitude of J_{avg} with an increase in electrode spacing h

(Figure 37 and Figure 38) and an increase in relaxation time for J_{avg} (Figure 38) for $n_b = 92.5$ mM are purely geometric and must be explainable as such. Now, for a charging capacitor the current density as a function of time can be written as

$$J = J_0 e^{-t/\tau_c} \tag{126}$$

where $\tau_c = RC = (h/\sigma A)C$ is the characteristic relaxation time for the capacitor, A is the effective area of the capacitor electrodes, C is the capacitance and σ is the conductivity of the dielectric medium between the two electrodes. With this, it is self apparent that a doubling of the electrode spacing h must result in a doubling of the characteristic RC time τ_c as well. An increase in the resistance $R = (h/\sigma A)$ also accounts for the decrease in the maximum value for J_{avg} for both ionic concentrations of $n_b = 4.6\,mM$ and $n_b = 92.5\,mM$ (Figure 37 and Figure 38). Similarly, doubling the distance between the capacitor electrodes would presumably double the time taken by ions in moving from one electrode to another thereby resulting in a near doubling of the period of oscillations observed in the case of $n_b = 4.6\,mM$ (Figure 37).

In summary, the results for the space averaged current density presented in this section raise more questions than they answer about the charge relaxation dynamics of an electrolytic nanocapacitor. The relaxation of J_{avg} for the case of EDL overlap of 0.1 is easily explained on the basis of what is already known but this is to be expected since with a thin EDL it approximates more closely the case of macroscopic systems where thin EDLs can be neglected and this is what results in an all too familiar behavior. The case of EDL overlap of 1.4 is, however, more intriguing because of the oscillatory behavior observed for J_{avg} in general and the presence of apparently persistent oscillations in particular. This oscillatory behavior thus warrants further understanding through a comparative analysis and exploration of other accessible simulation variables.

6.4.2. Oscillations in J_{avg}

This section compares the time evolution of electric potential and electric field, ionic charge densities and cation and anion current densities, for electric double layer overlaps of $\alpha = 1.4$ and $\alpha = 0.1$, cation to anion diffusion coefficient of $1:1$, an electrode spacing of $50\,nm$ and a solvent viscosity of $0.0018\,kgm^{-1}s^{-1}$. As expected from the space averaged current densities for the two cases, electric potential and field, normalized ionic density distributions and anion and cation current density distributions exhibit an oscillatory behavior for EDL overlap of $\alpha = 1.4$ which is evident from the various snapshots in time shown in Figure 39 to Figure 41 while in the case of EDL overlap of $\alpha = 0.1$ Figure 42 to Figure 44 show a monotonic convergence to equilibrium electrostatic plots for these variables. The force that ions experience at any point between the two electrodes of the capacitor is proportional to the electric field $\boldsymbol{E}$ seen by the ions at that location. A comparison of the electric field profiles in the gap between the capacitor electrodes in Figure 39 and Figure 42 for the two cases of EDL overlap shows that both exhibit a trough in the middle. This trough in the case of an EDL overlap of $\alpha = 1.4$ is parabolic in shape while the one for $\alpha = 0.1$ is flat bottomed. So, in terms of an analogy, the oscillatory motion of ions can be likened to the motion of a ball rolled in a parabolic trough and a flat bottomed trough with rough surfaces under the influence of gravity from the top edges of the troughs respectively.

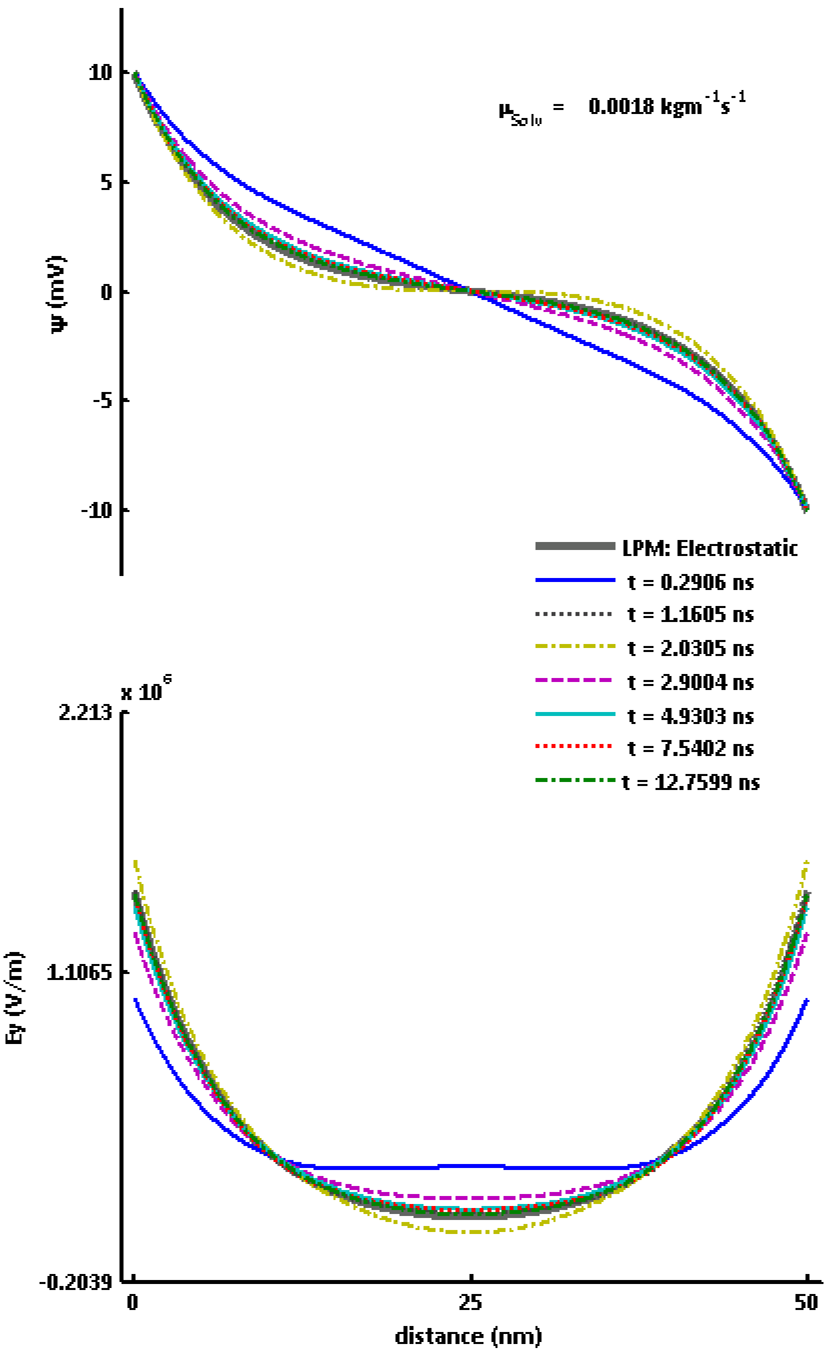

Figure 39. Oscillating electric potential ψ and y-component of the electric field E_y for EDL overlap $\alpha = 1.4$ and cation to anion diffusion coefficient ratio of 1: 1.

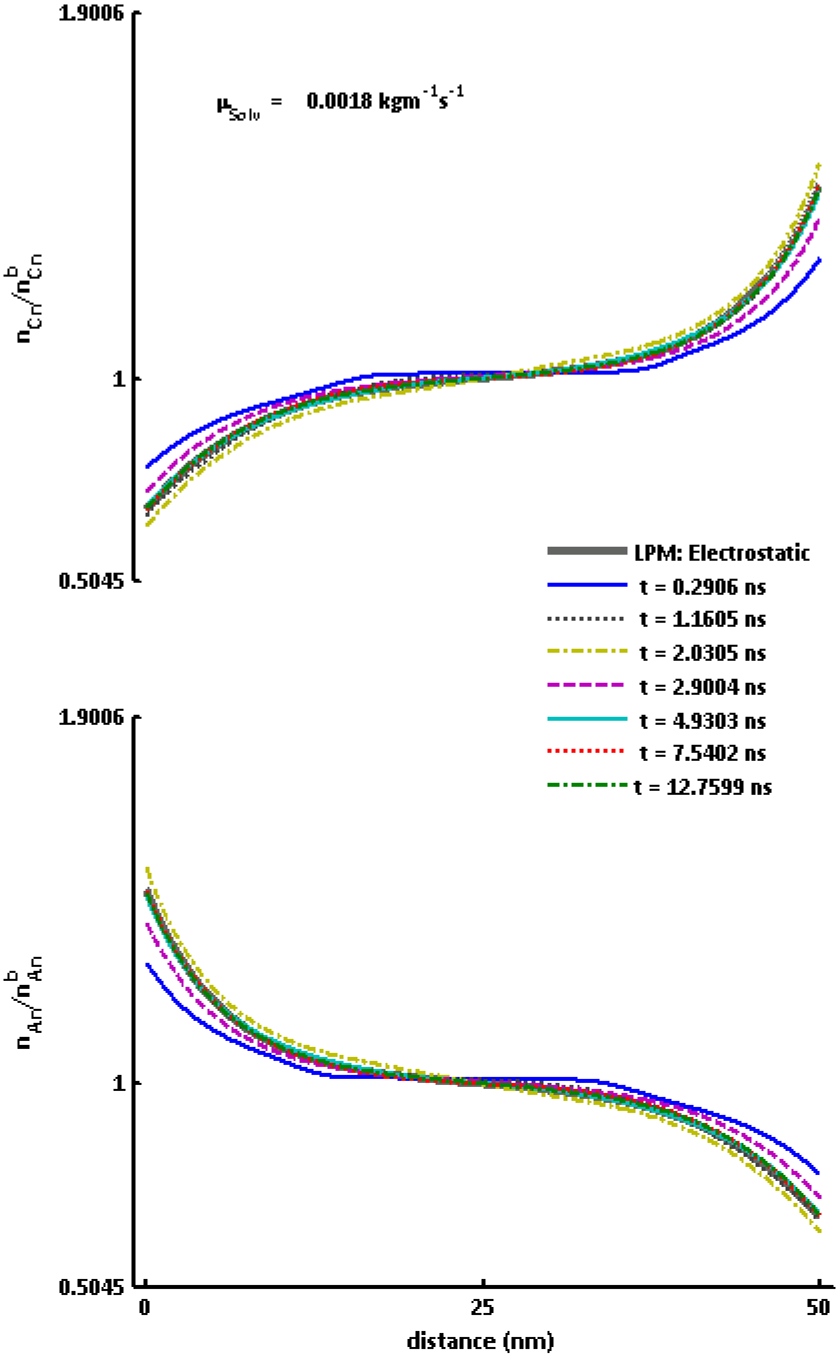

Figure 40. Oscillating cation and anion density distributions for EDL overlap $\alpha = 1.4$ and cation to anion diffusion coefficient ratio of $1:1$.

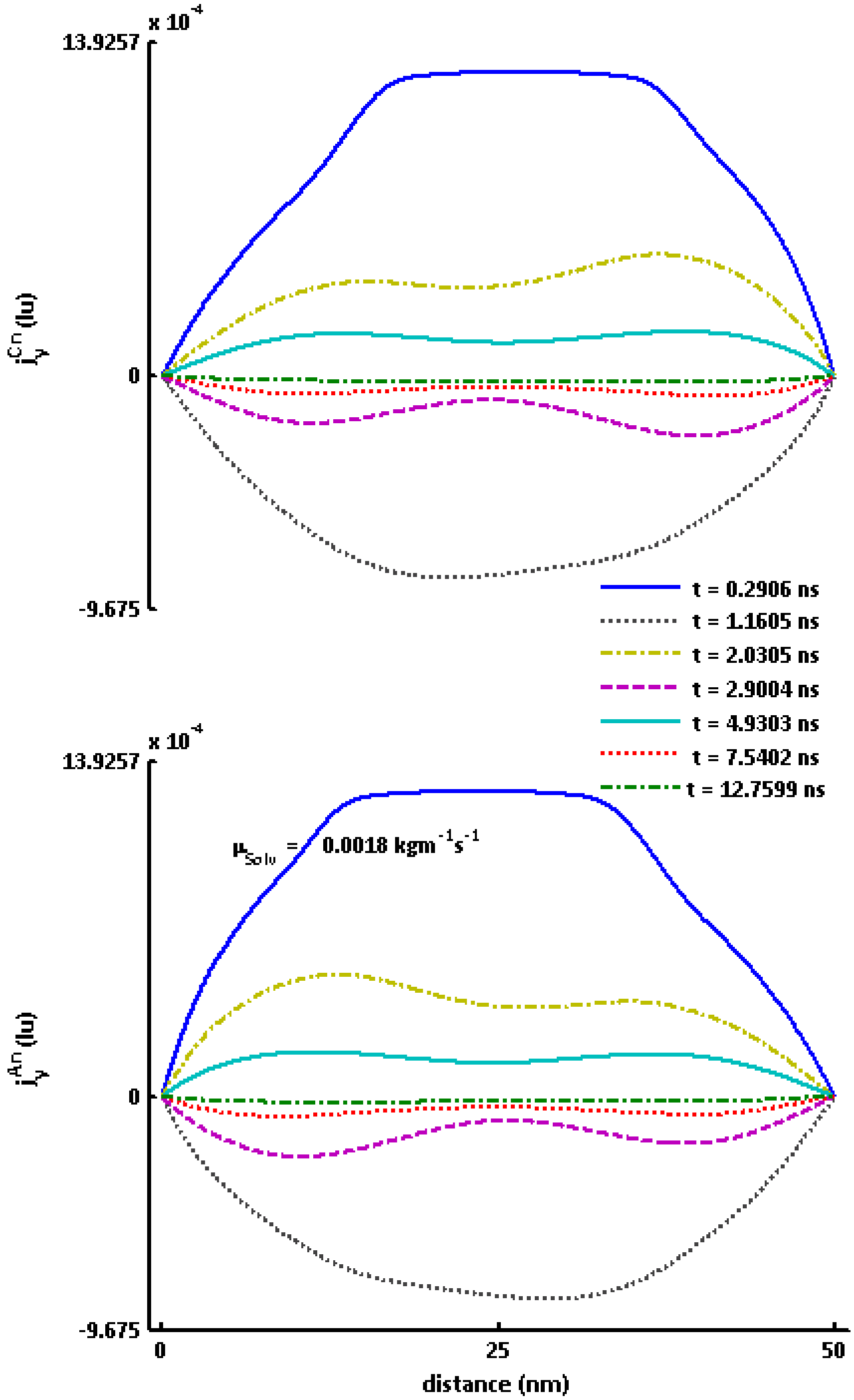

Figure 41. Oscillating non-dimensional cation and anion current density distributions for EDL overlap $\alpha = 1.4$ and cation to anion diffusion coefficient ratio of $1:1$.

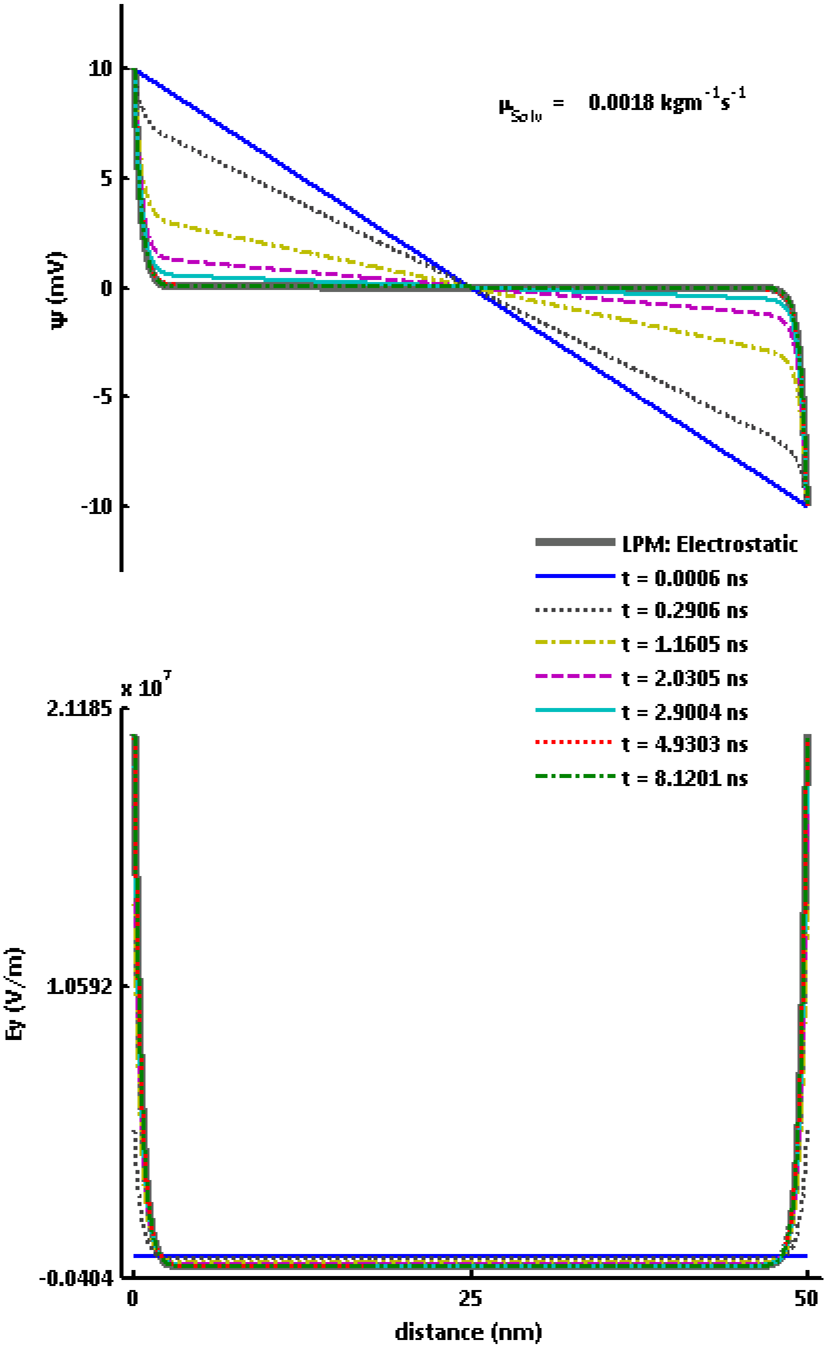

Figure 42. Monotonic behavior of electric potential ψ and y-component of the electric field E_y for EDL overlap $\alpha = 0.1$ and cation to anion diffusion coefficient ratio of $1:1$.

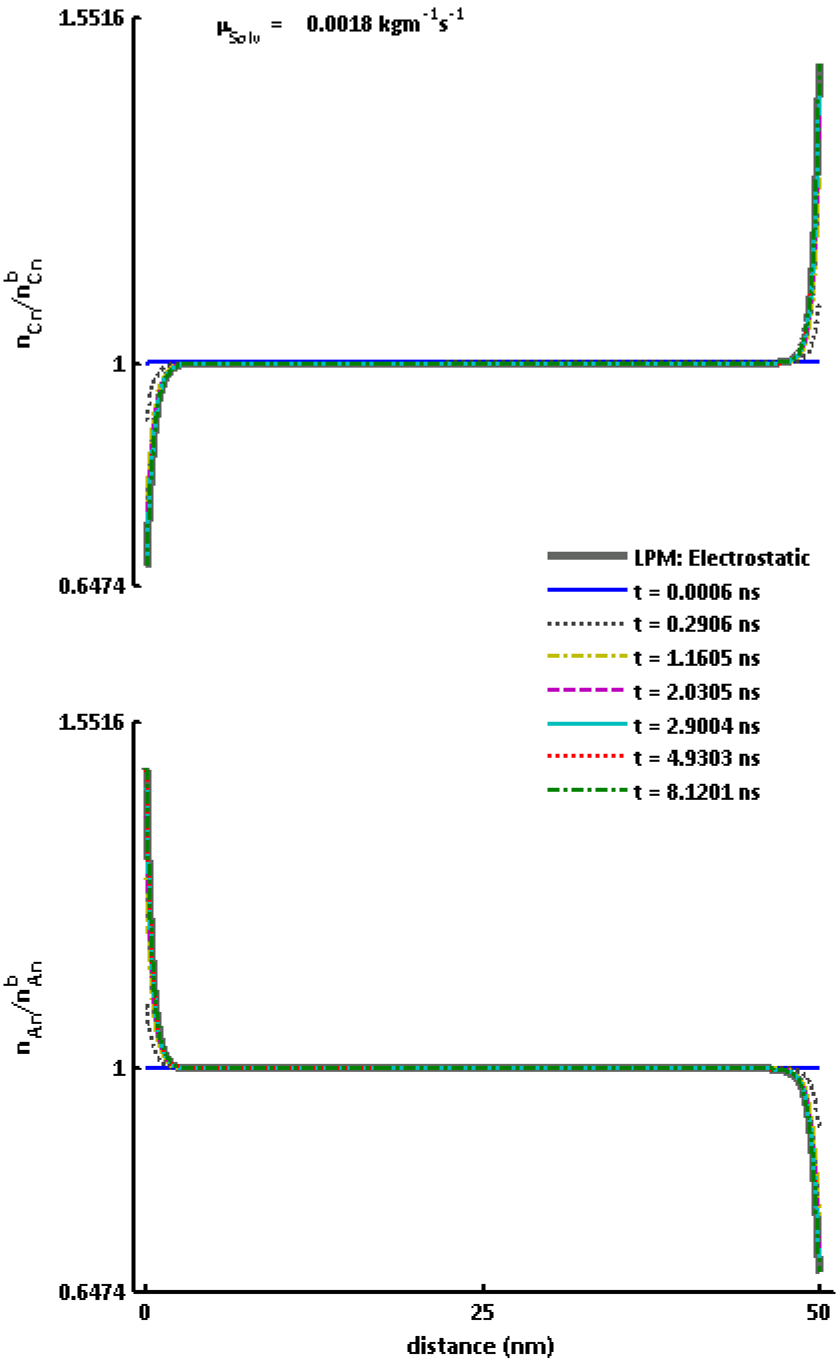

Figure 43. Monotonic behavior of cation and anion density distributions for EDL overlap $\alpha = 0.1$ and cation to anion diffusion coefficient ratio of $1:1$.

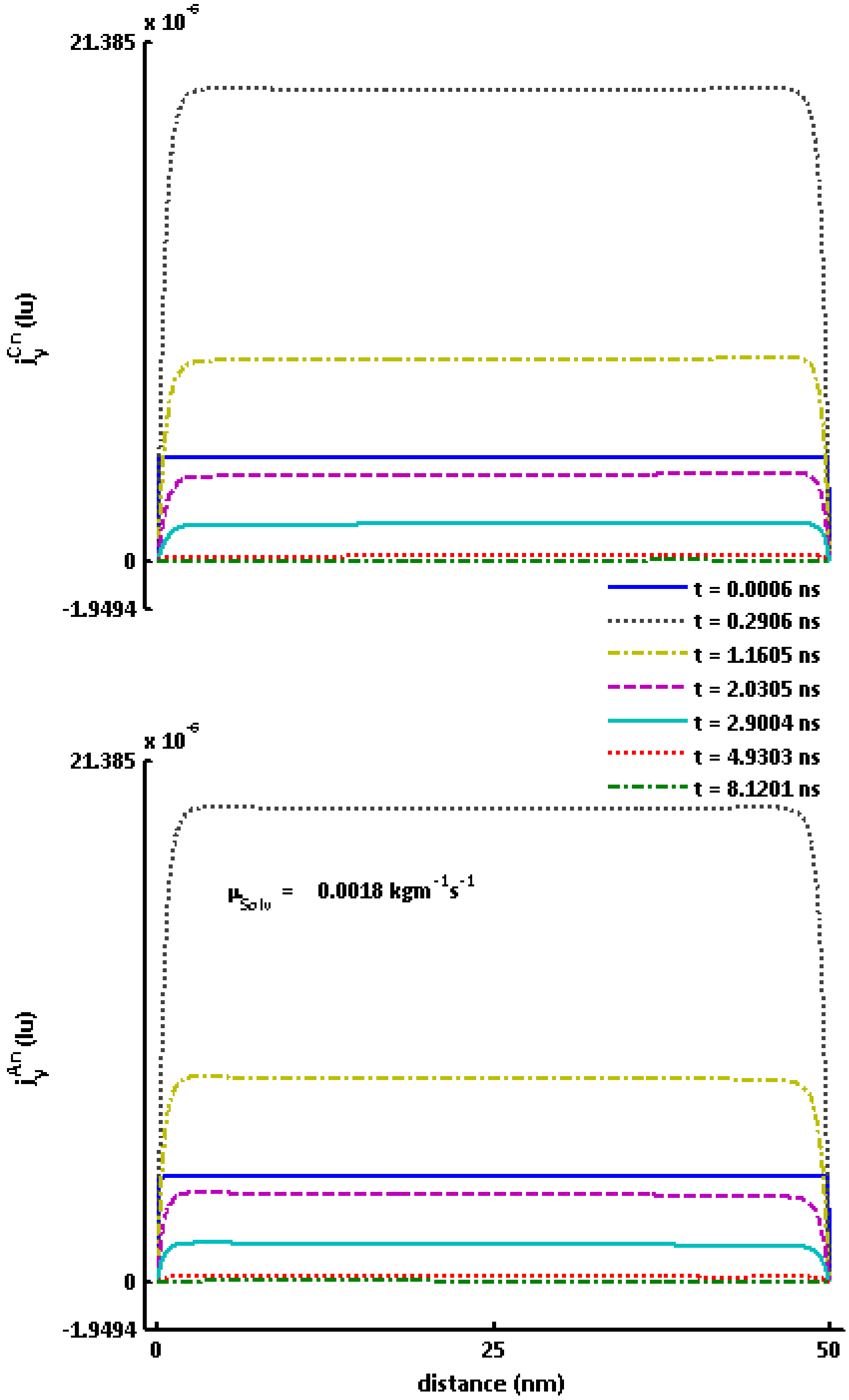

Figure 44. Monotonic behavior of non-dimensional cation and anion current density distributions for EDL overlap $\alpha = 0.1$ and cation to anion diffusion coefficient ratio of 1: 1.

In the parabolic case, the ball exhibits a to-and-fro oscillatory motion before coming to rest while in the flat-bottomed case it comes to rest more or less monotonically. Thus, this explains that the parabolic or near parabolic shape of the electric field profile in the case of overlapping electric double layers between the nanocapacitor electrodes is what is responsible for the observed oscillatory behavior. More fundamentally, the damped oscillatory behavior of J_{avg} for overlapping EDLs with a high degree of overlap, in response to a step potential applied to the capacitor electrodes at $t = 0$, results from a cyclic conversion of the kinetic energy of the moving ions to potential energy and vice versa in the presence of a viscous dissipative force exerted by the solvent.

But this still does not explain the persistence of oscillations observed in some of the cases for the space averaged current density J_{avg}. The next section tries to answer this question.

6.4.3. Persistence of oscillations in J_{avg}: A quest for an answer

A persistence of oscillations in the space averaged current density $J_{avg}$was observed in three cases for an EDL overlap of $\alpha = 1.4$: (i) For $\mu_{solv} = 0.0008\, kgm^{-1}s^{-1}$ (Figure 32), (ii) $\mu_{solv} = 0.0013\, kgm^{-1}s^{-1}$ (Figure 32), and (iii) For $\mu_{solv} = 0.0018\, kgm^{-1}s^{-1}$ when an asymmetry was introduced by changing the cation to anion diffusion coefficient ratio from $1{:}\,1$ to $2{:}\,1$ (Figure 35). Since the origin of persistent oscillations is similar for cases (i) and (ii), besides case (iii), only the case pertaining to $\mu_{solv} = 0.0008\, kgm^{-1}s^{-1}$ is analyzed further.

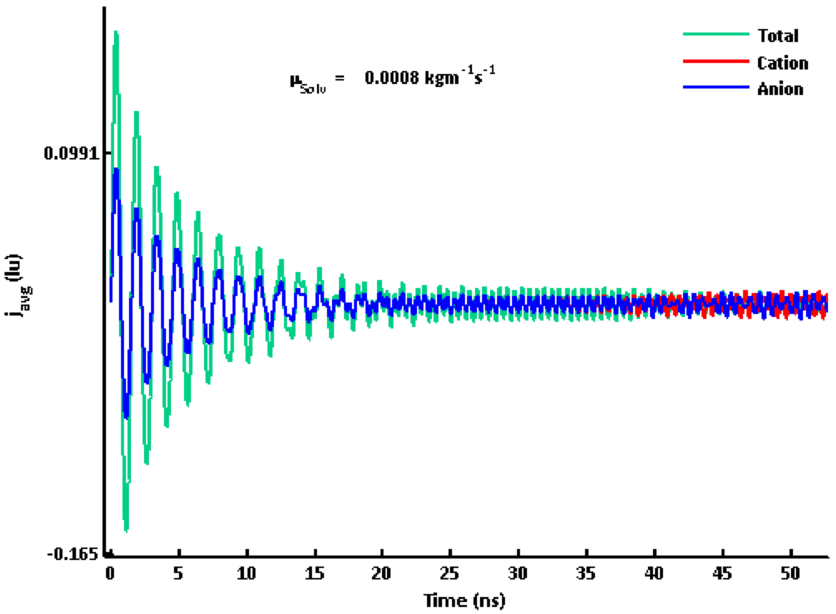

Figure 45. Oscillatory behavior of the space averaged total, cation and anion current densities for an EDL overlap of $\alpha = 1.4$ and cation to anion diffusion coefficient ratio of $1:1$.

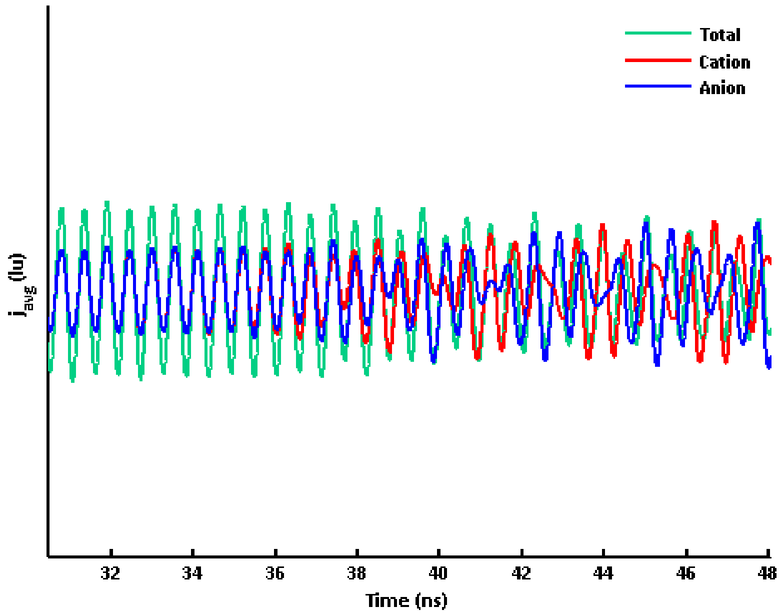

Figure 46. (Zoomed-In) Oscillatory behavior of the space averaged total, cation and anion current densities for an EDL overlap of $\alpha = 1.4$, cation to anion diffusion coefficient ratio of $1:1$ and $\mu_{solv} = 0.0008\ kgm^{-1}s^{-1}$.

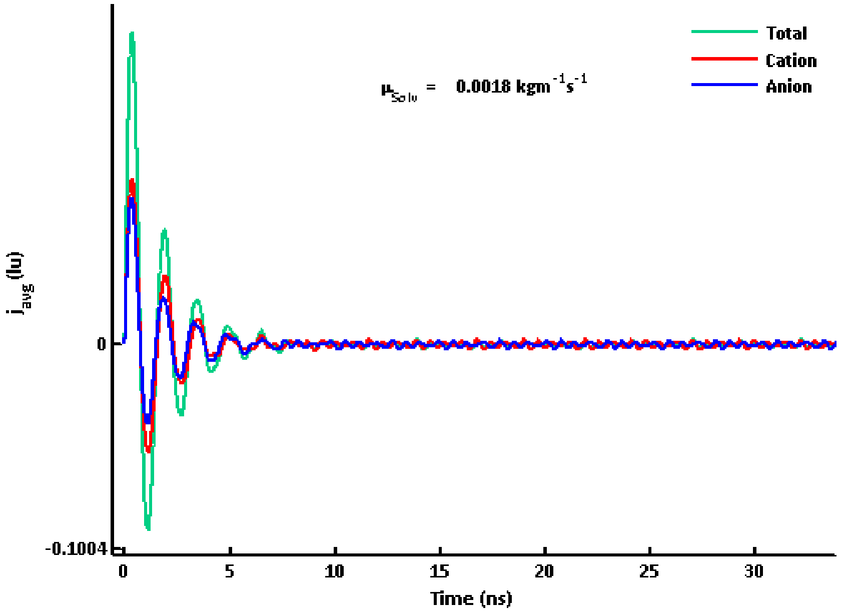

Figure 47. Oscillatory behavior of the space averaged total, cation and anion current densities for an EDL overlap of $\alpha = 1.4$ and cation to anion diffusion coefficient ratio of $2:1$.

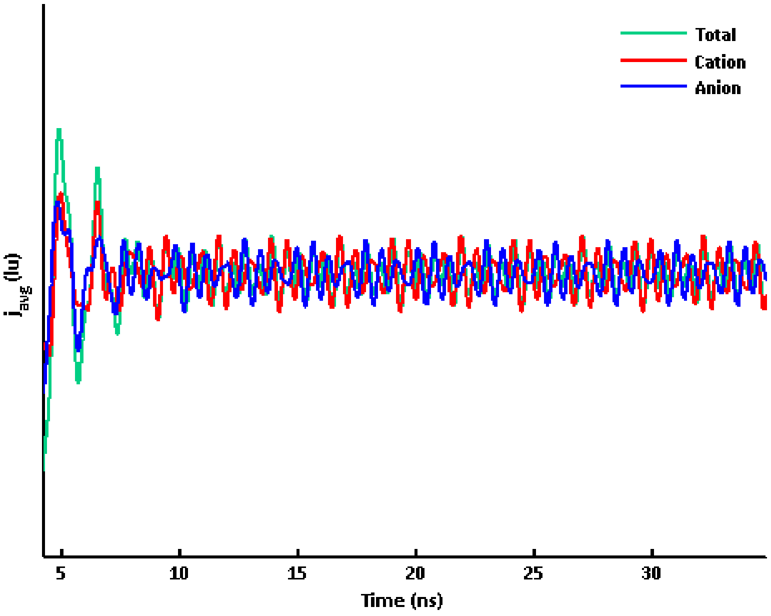

Figure 48. (Zoomed-In) Oscillatory behavior of the space averaged total, cation and anion current densities for an EDL overlap of $\alpha = 1.4$, cation to anion diffusion coefficient ratio of $2:1$ and $\mu_{solv} = 0.0008\ kgm^{-1}s^{-1}$.

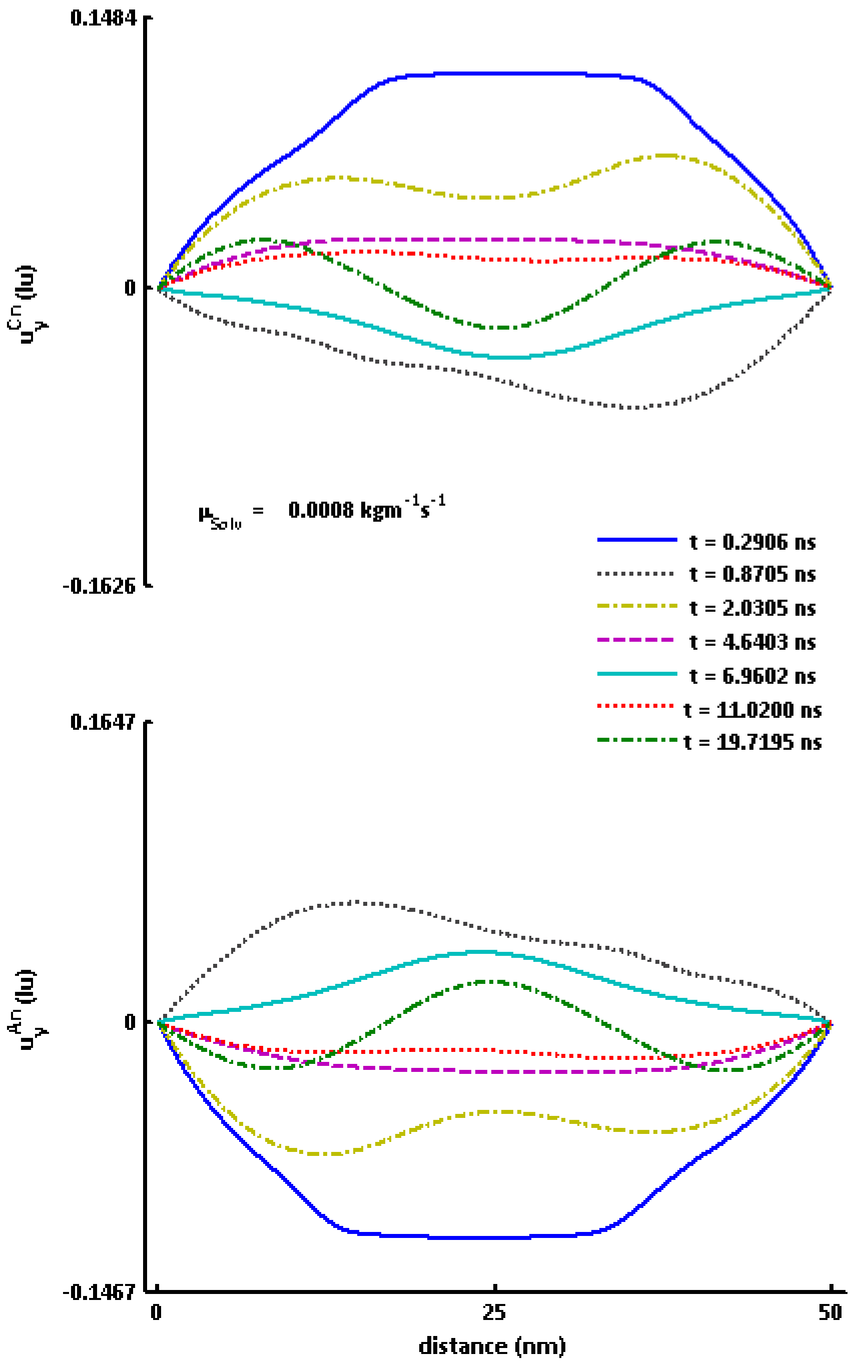

Figure 49. Time evolution of y-component of cation u_y^{Cn} and anion u_y^{An} velocities for the times when the space-averaged cation J_{Cn}^{avg} and anion J_{An}^{avg} current densities are in-phase for an EDL overlap of $\alpha = 1.4$.

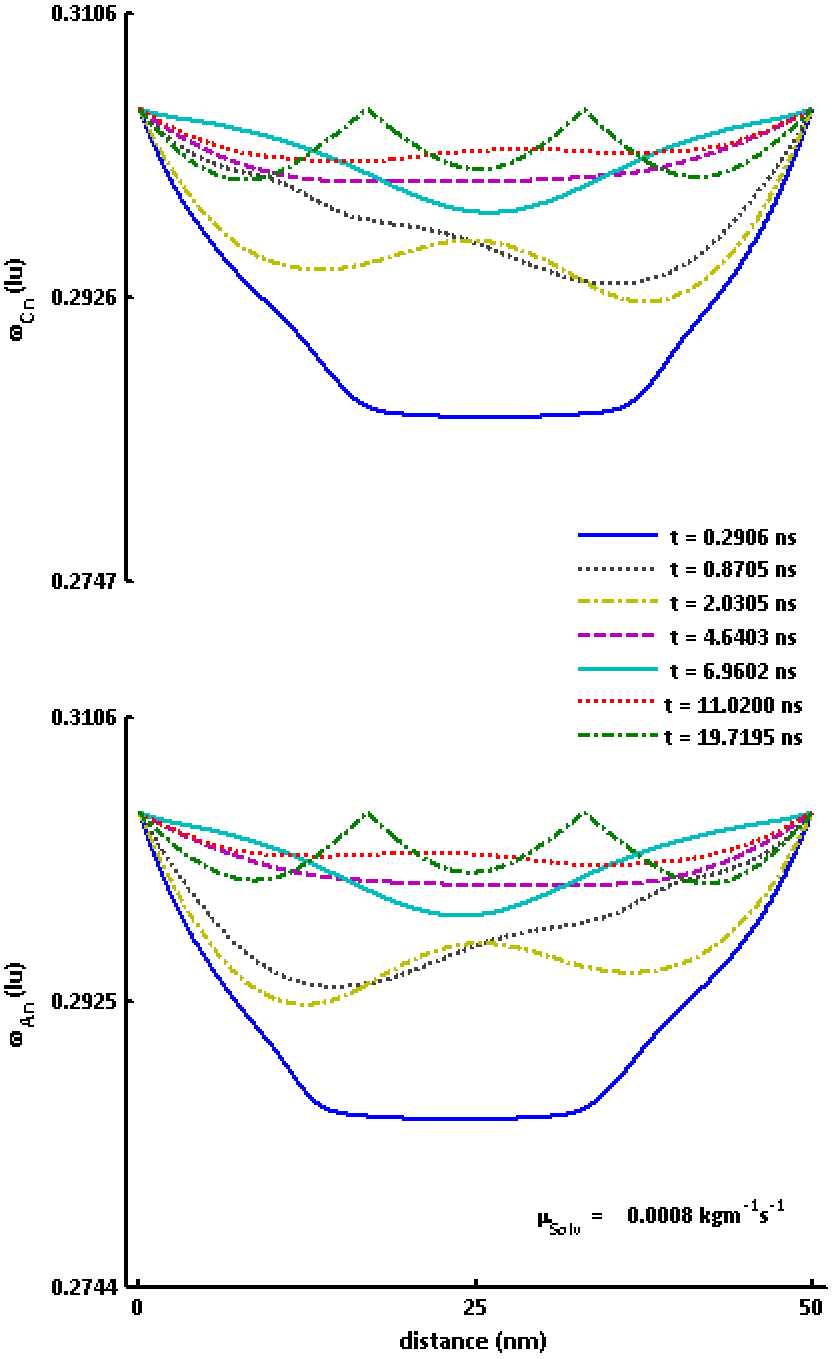

Figure 50. Time evolution of cation ω_{Cn} and anion ω_{An} collision frequencies for the times when the space-averaged cation J_{cn}^{avg} and anion J_{an}^{avg} current densities are in-phase for an EDL overlap of $\alpha = 1.4$.

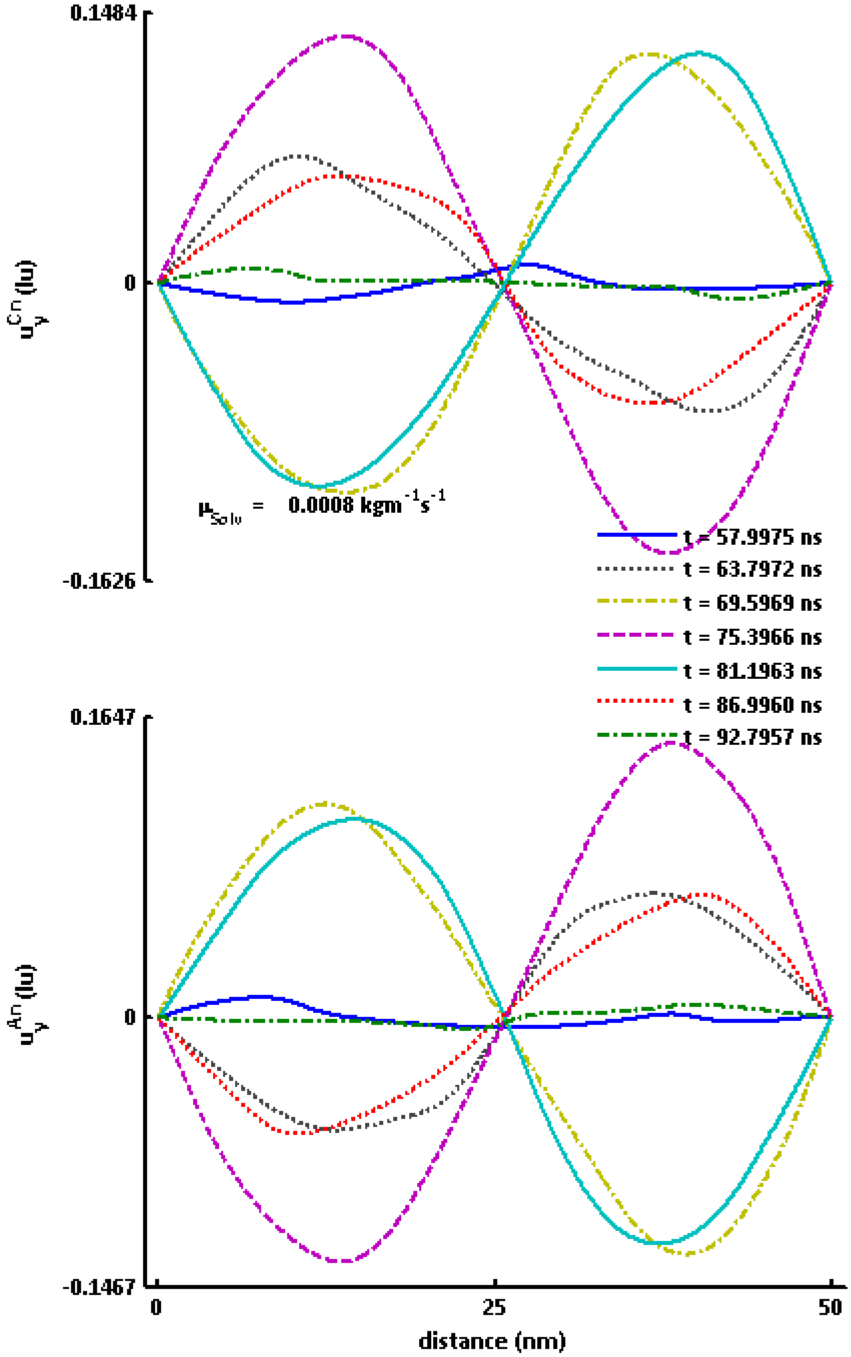

Figure 51. Time evolution of y-component of cation u_y^{Cn} and anion u_y^{An} velocities for the times when the space-averaged cation J_{Cn}^{avg} and anion J_{An}^{avg} current are out-of-phase for an EDL overlap of $\alpha = 1.4$.

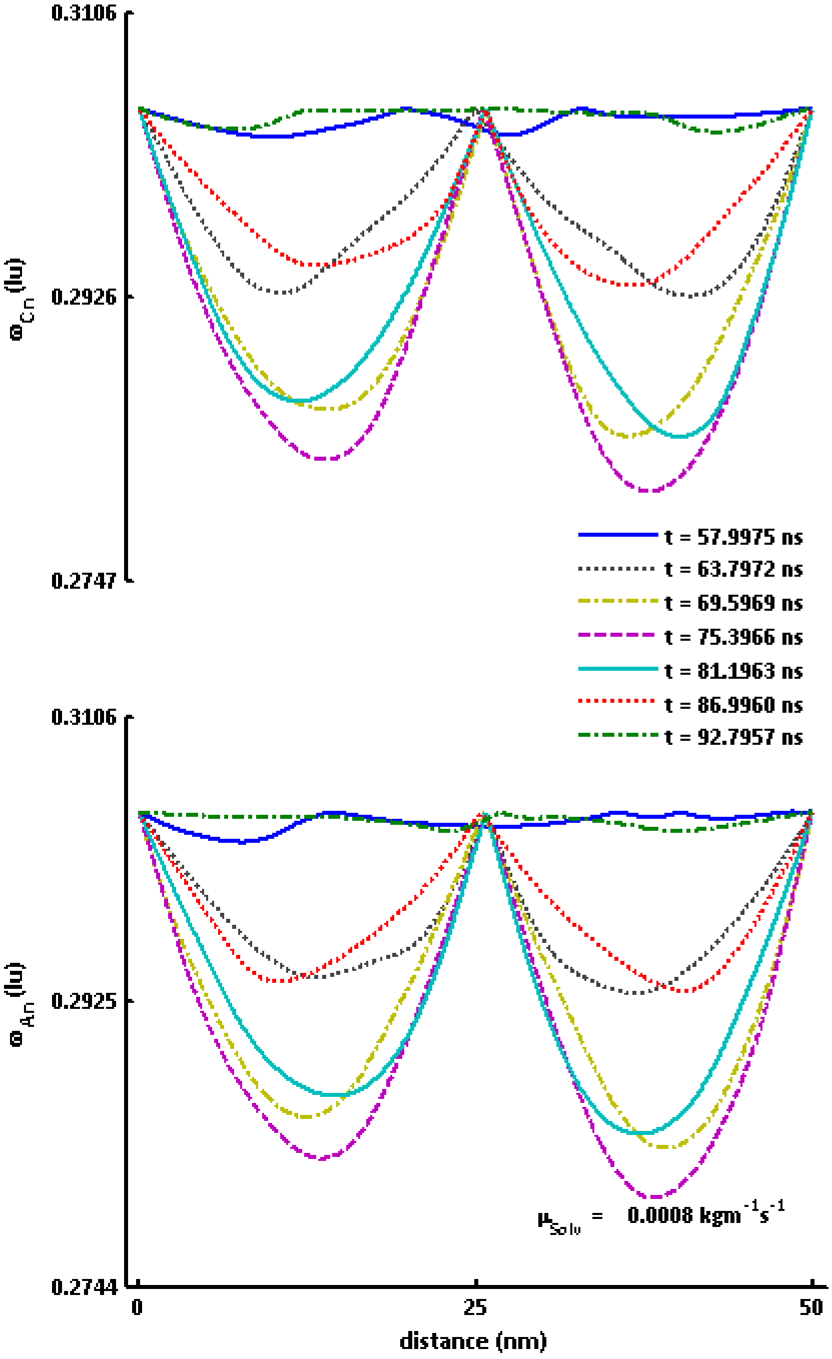

Figure 52. Time evolution of cation ω_{Cn} and anion ω_{An} collision frequencies for the times when the space-averaged cation J_{cn}^{avg} and anion J_{an}^{avg} current densities are out-of-phase for an EDL overlap of $\alpha = 1.4$.

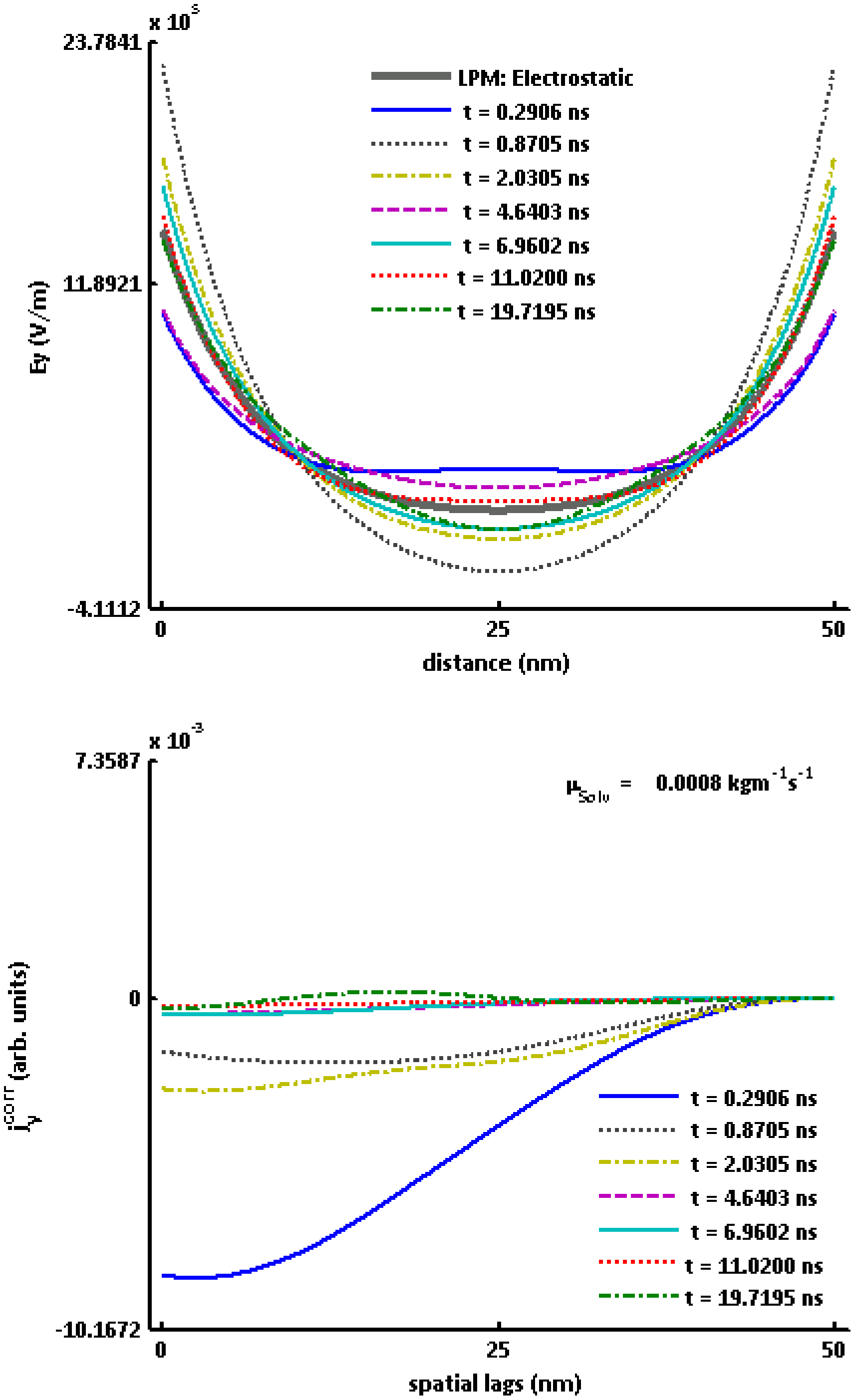

Figure 53. Time evolution of y-component of the electric field E_y and spatial cross-correlation j_y^{corr} of ionic flux densities J_{Cn}^{f} and J_{An}^{f} for the times when the space-averaged cation J_{cn}^{avg} and anion J_{an}^{avg} current densities are in-phase for an EDL overlap of $\alpha = 1.4$.

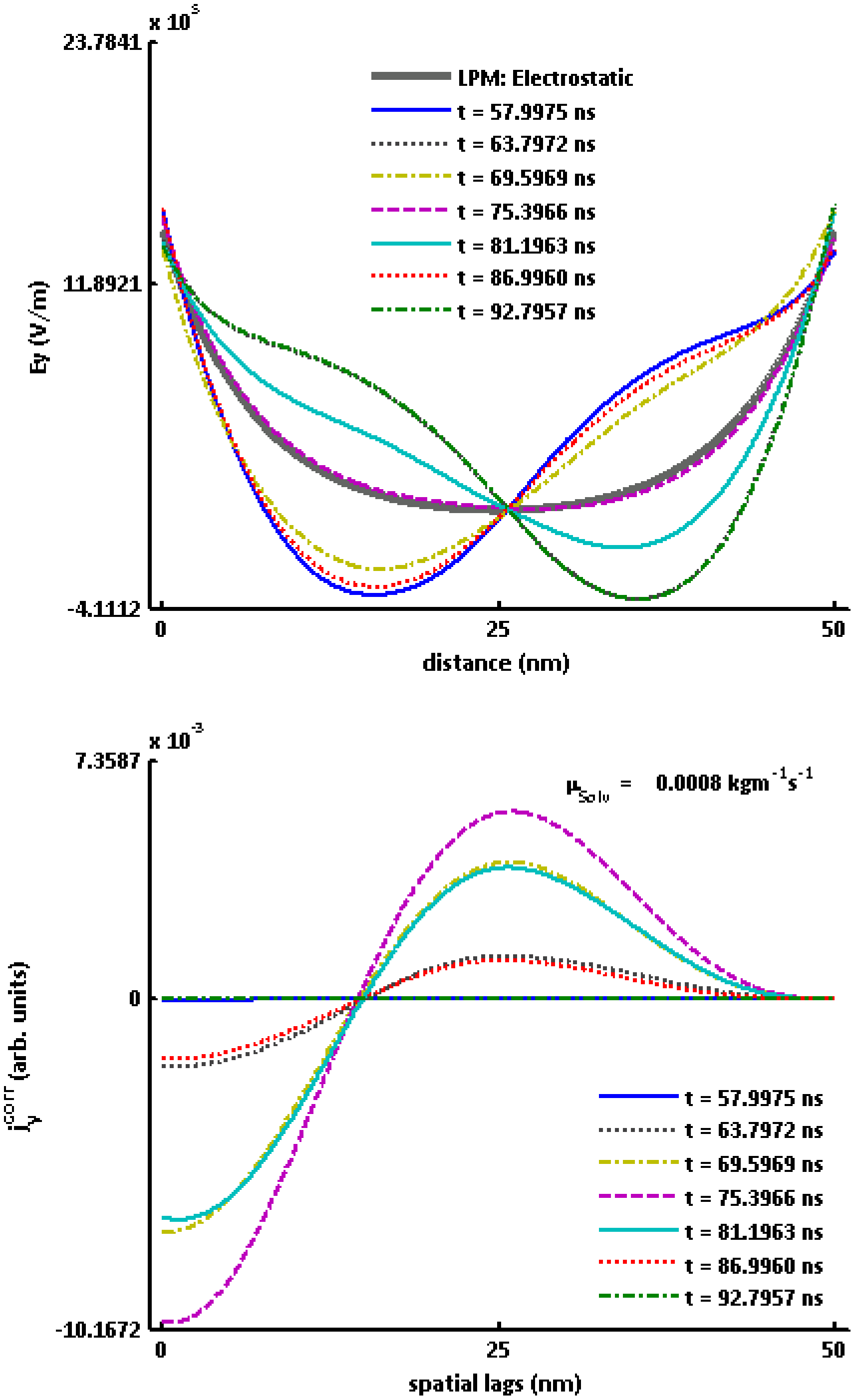

Figure 54. Time evolution of y-component of the electric field E_y and spatial cross-correlation j_y^{corr} of ionic flux densities J_{Cn}^{f} and J_{An}^{f} for the times when the space-averaged cation J_{cn}^{avg} and anion J_{an}^{avg} current densities are out-of-phase for an EDL overlap of $\alpha = 1.4$.

To understand this phenomena, time and space dependencies of new simulation variables of space averaged ionic current densities (J_{Cn}^{avg} and J_{An}^{avg}), y-component of ionic velocities (u_y^{Cn} and u_y^{An}), non-dimensional ionic collision frequencies (ω_{Cn} and ω_{An}) and spatial cross-correlation $J_y^{corr}$of the y-component of ionic flux densities $J_{Cn}^f(t)$ and $J_{An}^f(t)$ are plotted and examined.

Figure 45 and Figure 46 (zoomed in version of Figure 45) show that in the first case for $\mu_{solv} = 0.0008\ kgm^{-1}s^{-1}$, initially the space averaged ionic current densities J_{Cn}^{avg} and J_{An}^{avg} are in-phase with each other but once the pattern of persistent oscillations develops J_{Cn}^{avg} and J_{An}^{avg} become out-of-phase. A similar behavior can be seen for case (iii) of $\mu_{solv} = 0.0018\ kgm^{-1}s^{-1}$ and cation to anion diffusion coefficient ratio of $2:1$ in Figure 47 and Figure 48.

Considering case (i) first, the ionic velocities plotted in Figure 49 corresponding to the in-phase period for J_{Cn}^{avg} and J_{An}^{avg} show a general oscillatory behavior reflected in the total current density J_{avg} for a period up to 11 ns. Thereafter, between 11 and 20 ns there develop two nodes at roughly 1/3rd of the electrode spacing from either electrode where the ionic velocities go to zero and switch signs. The region of these two nodes between the nanocapacitor electrodes is marked by intense collisions as evidenced by the presence of two sharp peaks at roughly 1/3rd of the separation between the two electrodes from each electrode (Figure 50). Once the persistent oscillations are fully developed, in the period between 58 and 93 ns the ionic velocities exhibit only a single node between the capacitor plates where they switch sign at any one given instance of time (Figure 51) and the region of this node in the center of the nanocapacitor is again marked by intense collisions between ions (Figure 52). On either side of this region there exist regions where the collision frequencies are much lower and the ionic velocities are high. In these regions of low collisions the ionic velocities switch sign at different instances of time suggesting an oscillatory behavior in time. Next, upon examination of the spatial cross-correlation $J_y^{corr}$of the y-component of the ionic flux densities $J_{Cn}^{f}(t)$ and $J_{An}^{f}(t)$ in the time regime (0-11 ns) when J_{Cn}^{avg} and J_{An}^{avg} are in-phase, one observes that spatial cross-correlation J_y^{corr} stays negative and the electric field amplitude for E_y exhibits oscillatory behavior about the equilibrium electrostatic electric field in the center of the simulation domain (Figure 53). The negative values of J_y^{corr} are consistent with the in-phase behavior of J_{Cn}^{avg} and J_{An}^{avg} because for a given electric field at a point oppositely charged ions must move in opposite directions and hence the negative correlation in their respective fluxes. Between 11 and 20 ns, however a positive correlation between the ionic flux densities $J_{Cn}^{f}(t)$ and $J_{An}^{f}(t)$ begins to manifest itself (Figure 53). For the spatial cross-correlation $J_y^{corr}$of the y-component of the ionic flux densities $J_{Cn}^{f}(t)$ and $J_{An}^{f}(t)$, in the out-of-phase time regime (58-93 ns) for J_{Cn}^{avg} and J_{An}^{avg}, positive values for J_y^{corr} are observed with a peak at a spatial lag or separation of about 25.3 nm (Figure 54). Also, the electric field E_y starts to exhibit spatial oscillations in this time regime (Figure 54) unlike the case of simple oscillations in amplitude at the center of the nanocapacitor in the time regime when J_{Cn}^{avg} and J_{An}^{avg} are in-phase (Figure 53). It is easy to see that the minima of these spatial oscillations are again separated roughly by 25.3 nm.

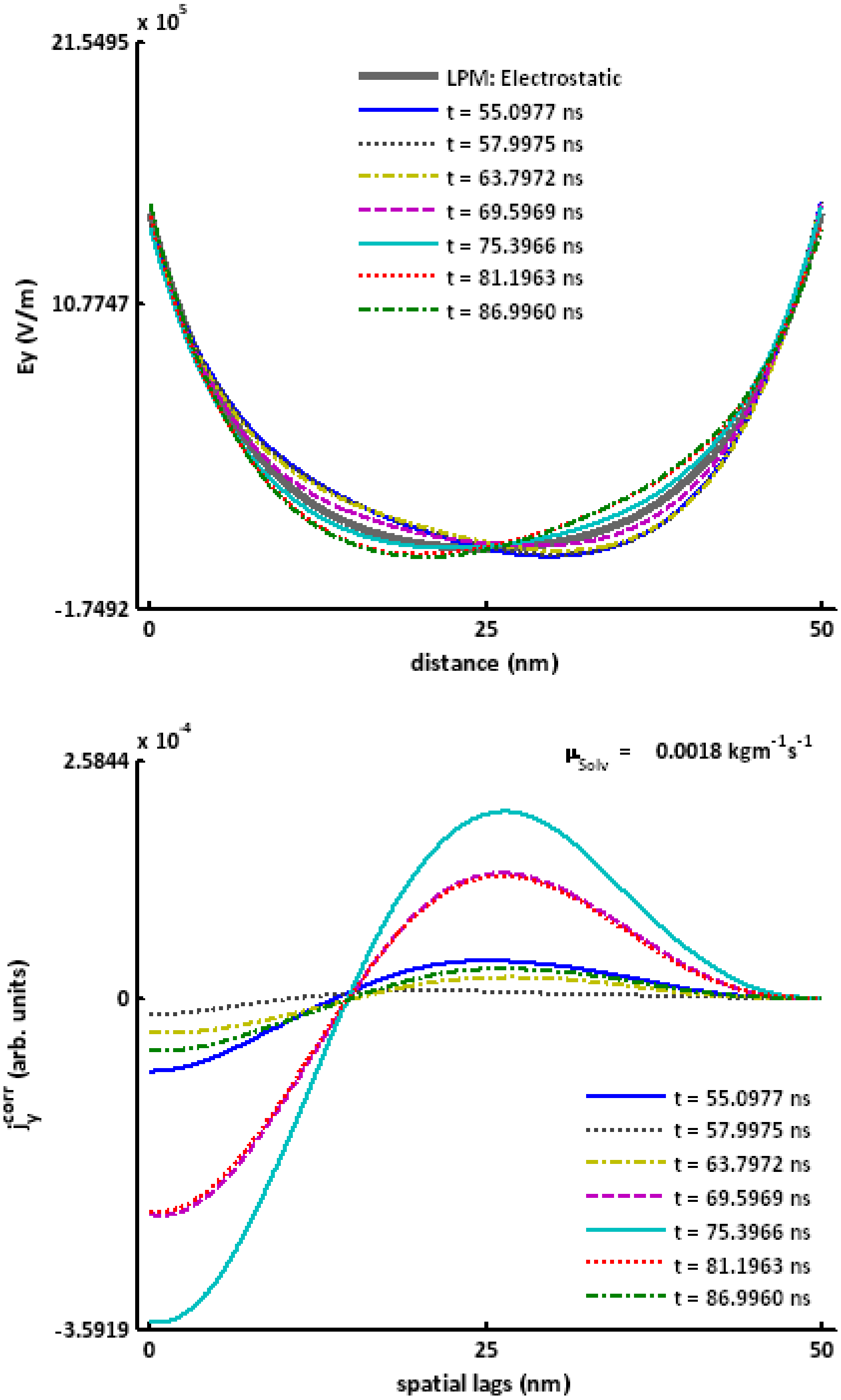

Figure 55. Time evolution of y-component of the electric field E_y and spatial cross-correlation j_y^{corr} of ionic flux densities J_{Cn}^f and J_{An}^f for the times when the space-averaged J_{cn}^{avg} and J_{an}^{avg} are out-of-phase for $\alpha = 1.4$ and ionic diffusion coefficient ratio of 2: 1.

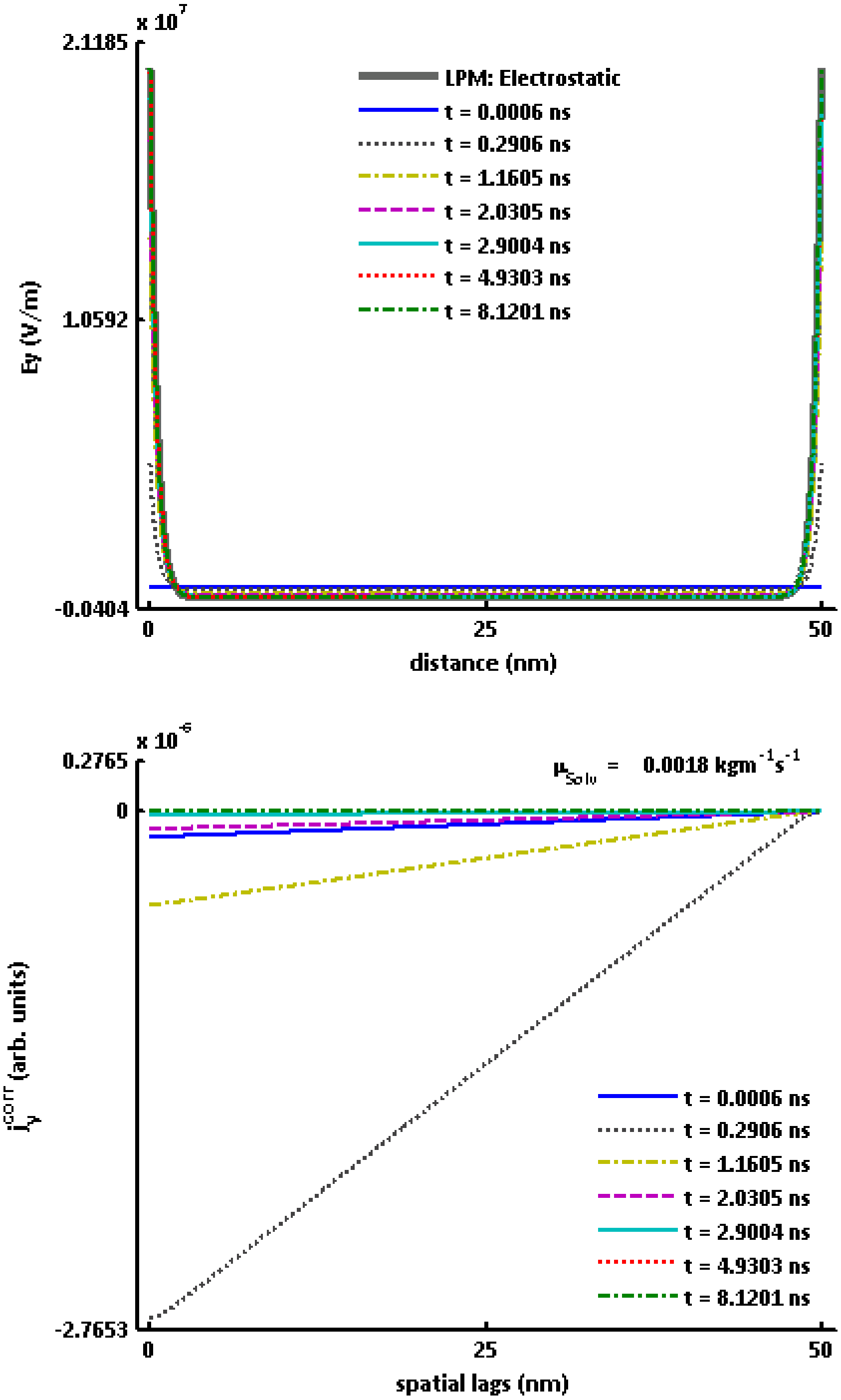

Figure 56. Time evolution of y-component of the electric field E_y and spatial cross-correlation j_y^{corr} of ionic flux densities J_{Cn}^{f} and J_{An}^{f} for an EDL overlap of $\alpha = 0.1$ and ionic diffusion coefficient ratio of $1:1$.

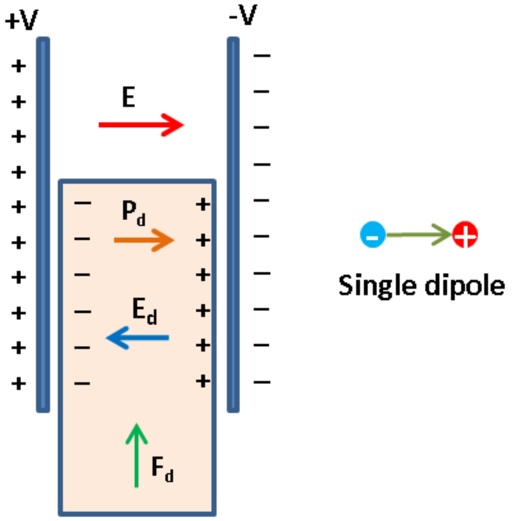

Figure 57. Dielectric slab in a capacitor.

Now, if Figure 51 is examined again, this time more closely, it can be seen that the ionic velocities of oppositely charged ions are positively correlated in the opposite halves of the simulation domain and exhibit a sort of standing wave-pattern.

Similar positive correlation of ionic flux densities, although a lot weaker than in case (i), is also observed for case (iii) with an EDL overlap of $\alpha = 1.4$, cation to anion diffusion coefficient ratio of $2:1$ and a solvent viscosity of $\mu_{solv} = 0.0008\, kgm^{-1}s^{-1}$ (Figure 55). Since such a behavior is absent in the case of $1:1$ diffusion coefficient ratio, the effect of introduction of an asymmetry in the diffusion coefficients or mobility of the ions is to cause persistent oscillations in electric field E_y and a positive correlation in the ionic flux densities J_{Cn}^{f} and J_{An}^{f}. Compared to the three cases discussed above, an exact contrast is presented in the case of an EDL overlap of $\alpha = 0.1$, cation to anion diffusion coefficient ratio of $1:1$ and a solvent viscosity of $\mu_{solv} = 0.0018\, kgm^{-1}s^{-1}$ (Figure 56) where the linear negative spatial cross-correlation monotonically goes to zero while the system marches to equilibrium as evidenced in the time evolution of the electric field E_y.

6.5. Discussion

With all the arguments and results presented in the previous section, it becomes apparent that in the time regime of out-of-phase space averaged ionic current densities J_{Cn}^{avg} and J_{An}^{avg} the oppositely charged ions in the two opposite halves of the simulation domain exhibit positively correlated motions implying a collective behavior resulting in plasma like oscillations. But then what is the reason behind such a collective behavior?

The reason becomes clear when one analyzes the behavior of a dielectric slab upon insertion into a capacitor (Figure 57). A dielectric slab, when slowly introduced into a capacitor, experiences a non-uniform electric field that exerts a force on it given by

$$\boldsymbol{F_d} = \boldsymbol{\nabla}(\boldsymbol{p_d}.\boldsymbol{E}) \tag{127}$$

that tends to drive it into a region of higher electric field. Since the field inside a dielectric slab points in a direction opposite to that of the electric field between the capacitor plates, the insertion of the dielectric slab has the effect of lowering the net electric field in the region occupied by it. Now consider the dielectric slab to be made up of oppositely charged ions interacting with each other to form temporary dipoles. With this, if the binding energy of the dipoles in the dielectric slab were less than the interaction energy of the individual ions (forming the dipole) with the external electric field of the capacitor then the dipoles will be pulled apart into individual ions and forced to move away (in the same direction) from the region of higher electric field as both types of ions are in a position that is far away from the equilibrium for the individual ions. Consider now a set of conditions like a region of lower electric field in the center of the capacitor or lower ionic velocities due to a viscous drag force acting on the ions that allows them to interact again to form dipoles. Now, if the field between the capacitor plates be non-uniform as in the case of the electrolytic nanocapacitor considered in this chapter, the dipolar interaction between the ions would again force them to move in to a region of higher electric field but this time in the opposite direction because of a residual momentum from their previous interaction with a region of high electric field. The net electric field in the region occupied by the ions interacting like dipoles would also be lowered until the time they again encounter a region of high electric field sufficiently strong to break them apart and cause a repeat of the cycle described above. Such a repetitive behavior would thus result in an oscillatory behavior of the electric field in space and spatially correlated motion of oppositely charged ions the kind of which was observed in the results presented in section 6.4.3 (Figure 54 and Figure 55).

Thus, it can be concluded that the persistent spatial oscillations observed in the y-component of the electric field E_y and the space averaged current densities J_{cn}^{avg} and J_{an}^{avg} are most likely due to a dipolar interaction occurring between the ions that results in a plasma like collective behavior of ions which is manifested in the positive peak of the spatial correlation j_y^{corr} for the ionic flux densities J_{Cn}^{f} and J_{An}^{f}.

The plasma frequency ω_p for an electrolyte in terms of the Debye length λ_D is given by

$$\omega_p = \frac{1}{\lambda_D}\sqrt{\frac{kT}{m^*}} \tag{128}$$

where m^* is the harmonic mean of the cation and anion masses [98]. An EDL overlap of $\alpha = 1.4$ corresponding to an ionic concentration of $n_b = 1.89\, mM$ gives a plasma frequency of $\omega_p \cong 20.6\, GHz$ while the collision frequency for the ions in a solvent of density $\rho_{solv} = 1000\; kg/m^3$ is of the order of $\nu_c \approx 5\, THz$. Since for such an electrolyte the collision frequency $\nu_c \gg \omega_p$, the current density is always in phase with the applied electric field and a plasma oscillation cannot be excited [98]. However, even with an oscillation frequency of $1.85\; GHz\; (< \omega_p)$ for the in-phase space averaged ionic current densities J_{cn}^{avg} and J_{an}^{avg} just before the onset of the out-of-phase behavior, collective plasma like oscillations are observed (Figure 46). Thus, the results pertaining to plasma-like collective oscillatory motion of ions presented here for overlapping electric double layers in an electrolytic nanocapacitor (in response to a step voltage of $\pm 10\; mV$ applied at $t = 0$ to the capacitor electrodes) appear to be purely an effect of nanoscale confinement.

Traditionally, the dynamics of a capacitor with blocking electrodes have been studied using the Poisson-Nernst-Planck (PNP) system of equations (54) and (55) that assume a constant ratio between ionic diffusion coefficient and mobility governed by the Nernst-Einstein relation (125). In simulations of the dynamics of most electrochemical systems using the PNP system of equations thin electric double layers are assumed which permit the use of the quasi-equilibrium description of ionic diffusion and mobility through the Nernst-Einstein relation. However, as pointed out in the introduction for chapter 5, the use of the PNP system of equations is not appropriate for simulating the dynamics of mesoscale electrochemical systems because of an assumption of continuum dynamics [77].

In LBM based modeling of electrochemical systems and electroosmotic flows researchers have either employed assumptions of bulk electroneutrality and thin electric double layers or assumed fully developed profiles for overlapping electric double layers [90, 91, 99]. Such an approach has permitted them the use of single relaxation time based on ionic diffusion coefficients in the lattice Boltzmann equation (LBE) for the simulation of ionic electrodiffusion. The use of a single relaxation time in the BGK approximation in the LBE assumes the validity of the Nernst-Einstein relation between the ionic diffusion coefficients and their mobilities. The Nernst-Einstein relation between the mobility and diffusion coefficient for transient dynamics of charge transport has been shown to be violated by several researchers, both experimentally and theoretically, in a number of diverse systems [100-109]. For the simulation of the charge relaxation dynamics of a mesoscale electrode-electrolyte interface with overlapping electric double layers such an assumption leads to a physically incorrect microscopic description of ionic collisions. Under such an unphysical assumption, regions of high ionic velocities and low concentrations relax at the same rate as the regions of low ionic velocities and high concentrations thereby leading to numerical instabilities and a failure of the multiphysics solver. Simulations of the entrance flow problem carried out in the previous chapter using molecular speed dependent relaxation time prove a case in point. Further, a quasiequilibrium description of the system dynamics allows one to conveniently ignore the effects of the viscous drag force exerted on the ions by the solvent molecules. This works fine under assumptions of bulk electroneutrality and thin electric double layers because of the diffusive nature of the ionic transport resulting in small ionic velocities but fails spectacularly when simulating conditions of overlapping electric double layers characterized by high electric fields and the resultant high ionic velocities. It is in this context that the results presented in this chapter for the simulation of charge relaxation dynamics in an electrolytic nanocapacitor using molecular speed dependent relaxation time assume significance.

6.6. Conclusions

The multiphysics solver developed in the previous chapter together with the molecular speed dependent relaxation time model of the lattice Boltzmann equation is successfully employed for the simulation of the transient dynamics of a mesoscale electrode-electrolyte interface. Simulations for the electrolytic nanocapacitor presented in this chapter show that the degree of overlap of electric double layers associated with the capacitor electrodes significantly alters and influences the nature of charge relaxation dynamics in response to an applied electric field or potential. The results presented in this chapter for the dynamics of overlapping electric double layers are of particular import for the simulation of ionic electrodiffusion at the neuron-microelectrode interface because, though the electric double layers at physiological ionic concentrations (120-150 mM) are only 1-2 nm in width, the overlapping electric double layers at the interface extend across its entire width (20-110 nm) due to the presence of the porous protein-glycocalyx matrix that helps neurons adhere to the microelectrode surface. The role that viscous drag forces play in affecting the dynamics of charge relaxation in the mesoscale coupling of plane parallel electrodes is also significant from the point of simulating ionic electrodiffusion at the neuron-microelectrode interface because the Volterra-Wiener kernels estimated using characterization of the neuron-electrode junction with Gaussian bandlimited white noise in chapter 2 (Figure 8 A and B) show overly damped dynamics for the neuroelectronic interface. This shows that the interfacial medium that fills the neuron-microelectrode cleft behaves like a highly viscous fluid. Thus, engineering approaches that lead to a reduction in the viscosity of the interfacial medium through surface chemical modification of the microelectrodes or a structurally more open less viscous interface like that provided by microelectrodes coated with carbon nanotube mats [36, 60, 65] might help improve the strength of the extracellular signals recorded at the neuroelectronic interface.

CHAPTER-7: CONCLUSIONS AND FUTURE WORK

7.1. Conclusions

Results presented in this dissertation focused on advancing an understanding of the mechanism of signal transduction at the neuron-microelectrode interface. An understanding of the mechanism of signal transduction, it was hoped, would help develop tools and strategies for an engineering of the neuroelectronic interface to improve the signal to noise ratio for the extracellular signals recorded using microelectrode or field effect transistor arrays.

With the above mentioned goals in mind, a 'data-true' characterization of the neuron-electrode junction was carried out using nonlinear Volterra-Wiener modeling. The experimental nonlinear dynamic characterization of the neuroelectronic interface employed Gaussian bandlimited white noise as a specialized stimulus to the neuron-microelectrode junction. Using the Lee-Schetzen technique of cross-correlation a nonlinear Volterra-Wiener model was estimated using the experimentally obtained stimulus response data. The results from Volterra-Wiener characterization presented in chapter 2 showed a nonlinear contribution to the extracellular signal recorded at the neuron-microelectrode interface. However, there was no conclusive evidence to say if the nonlinear contribution to the extracellular signal originated from the nonlinear dynamics of the neuron or it had nonlinear contributions from the interface as well.

In chapter 3, results from an optimization based study of equivalent circuit models of the neuroelectronic interface to determine their suitability for representing signals recorded at the neuron-electrode junction were presented. These results conclusively proved that there were nonlinear contributions from the interfacial medium during the process of signal transduction at the neuron-electrode junction that could not be modeled using linear equivalent circuit models.

Chapter 4 of the dissertation presented a theoretical framework for extraction of nonlinear material parameters like the dielectric permittivity, conductivity and diffusivity tensors employing Volterra-Wiener modeling based nonlinear impedance spectroscopy. It was argued that Volterra-Wiener modeling based nonlinear impedance spectroscopy presented a distinct advantage over the current method of characterizing nonlinear electrochemical systems using nonlinear harmonic analysis of input sinusoidal signals. It is expected that the material parameters thus extracted for the nonlinear dynamics of the neuroelectronic interface using this theoretical framework can be used in conjunction with a multiphysics model for ionic electrodiffusion to facilitate engineering of the neuron-microelectrode interface.

Chapter 5 presented results from a step-by-step development of a lattice Boltzmann method based multiphysics solver suitable for simulation of ionic electrodiffusion at the mesoscale neuron-microelectrode interface. Also, a molecular speed dependent relaxation time was proposed for use with the lattice Boltzmann equation that helped recover a physically correct microscopic description of particle collisions in the entrance flow problem. The use of continuously varying molecular speed dependent relaxation time in LBE promises to be numerically more stable compared to multiple relaxation time, two relaxation time and entropic lattice Boltzmann equation based methods while preserving the simplicity and elegance of the LBE based on single relaxation time BGK approximation.

Chapter 6 employed the multiphysics solver developed in chapter 5 along with the molecular speed dependent relaxation time to simulate the charge relaxation dynamics of a mesoscale electrolytic capacitor. Results were presented in this chapter for various degrees of electric double layer (EDL) overlap, solvent viscosities, electrode separations and cation to anion diffusion coefficient ratios. For an EDL overlap of 1.4, anomalous plasma like collective behavior of ions was observed which could be attributed to the occurrence of dipole like interaction between oppositely charged oscillating ions. Generally neglected in the Poisson-Nernst-Planck system of equations based modeling of electrochemical systems, the viscosity of the solvent was shown to play an important role in the charge relaxation dynamics of the mesoscale electrode-electrolyte interface in response to an applied voltage step across the nanocapacitor at t = 0. These results were then discussed in the context of their relevance for the mechanism of signal transduction at the neuroelectronic junction.

Thus, with the tools and strategies developed for and presented in this dissertation a synergistic approach to engineering the neuron-microelectrode can now be fruitfully pursued (Figure 58).

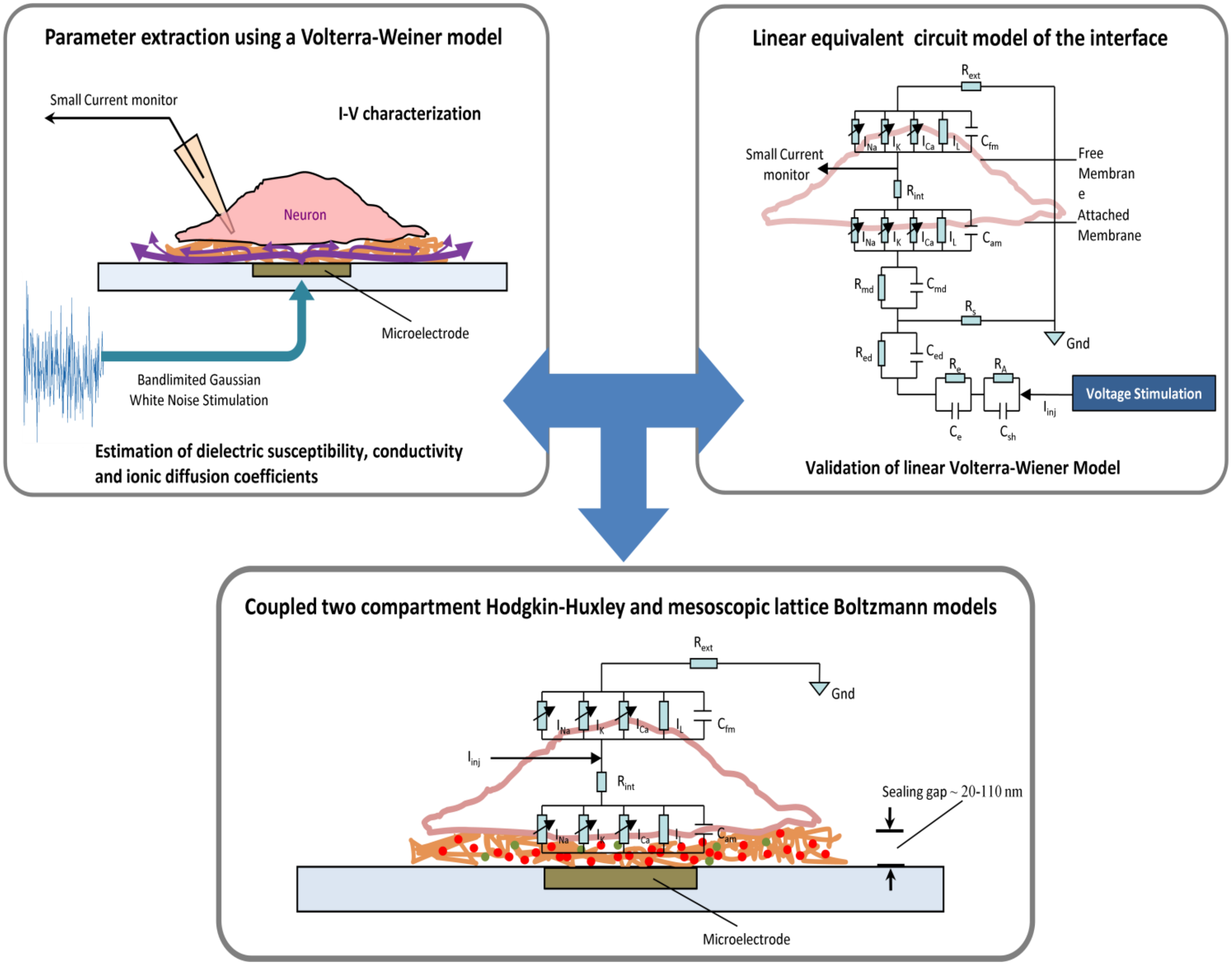
Parameter extraction using a Volterra-Weiner model
Small Current monitor
I-V characterization
Neuron
Microelectrode
Bandlimited Gaussian White Noise Stimulation
Estimation of dielectric susceptibility, conductivity and ionic diffusion coefficients
Linear equivalent circuit model of the interface
R_{ext}
I_{Na}
I_K
I_{Ca}
I_L
C_{fm}
Small Current monitor
Free Membran e
R_{int}
C_{am}
Attached Membrane
R_{md}
C_{md}
R_s
Gnd
R_{ed}
C_{ed}
R_e
R_A
Voltage Stimulation
I_{inj}
C_e
C_{sh}
Validation of linear Volterra-Wiener Model
Coupled two compartment Hodgkin-Huxley and mesoscopic lattice Boltzmann models
R_{ext}
Gnd
I_{Na}
I_K
I_{Ca}
I_L
C_{fm}
I_{inj}
R_{int}
C_{am}
Sealing gap ~ 20-110 nm
Microelectrode

Figure 58. A schematic of the sysnergistic approach advocated in this dissertation for engineering the neuron-microelectrode interface.

7.2. Future work

Future work on modeling, simulation and characterization of the neuroelectronic interface with the objective of engineering it to improve fidelity of the extracellular signals recorded from microelectrode or field effect transistor arrays would need to proceed as described in the following two sections:

7.2.1. Lattice Boltzmann model of the neuron-electrode interface

The next step in the development of an LB model of the neuron-microelectrode interface would be to couple the dynamics of the Hodgkin-Huxley model of the neuron to the mesoscopic LB model of ionic electrodiffusion in the interfacial medium by employing Neumann boundary conditions for ionic concentrations at the interface between the neural membrane and the LB model. No-diffusive flux boundary conditions could be employed at the boundary of the interface with the bulk extracellular medium to simulate the effect of the ground electrode and the effect of the bulk extracellular medium that acts as a source or sink depending on ion type. Development of such a hybrid model would allow for evaluation and analysis of the effect of various zeta-potential boundary conditions on the microelectrode, of variations in the conductivity of the interfacial medium etc on the mechanism of signal transduction at the neuroelectronic interface.

7.2.2. Nonlinear impedance spectroscopy based on Volterra-Wiener modeling

Starting with a very simple test system, the theoretical framework for extraction of interface parameters like the nonlinear dielectric permittivity, conductivity and diffusivity tensors would need to be systematically validated using progressively complex systems. The instrumentation employed in experiments to record experimental data and for stimulating systems with bandlimited Gaussian white noise and their effect on the recorded data would need to be carefully evaluated before trying to interpret the experimental stimulus-response data thus acquired. Linear impedance spectroscopy making use of equivalent circuit models for a description of the electrochemical phenomena and nonlinear harmonic analysis of sinusoidal stimuli on system behavior can be employed to good effect for validating the linear and nonlinear results obtained from Volterra-Wiener modeling based nonlinear impedance spectroscopy. Once a certain level of confidence is acquired working with the technique it can then be employed for use in the engineering of the neuron-microelectrode interface in conjunction with the multiphysics LB model of the neuroelectronic junction. It would then be possible to predict the effect of boundary conditions and material parameters using the LB model and verify the predictions using experimental recordings from the neuron-microelectrode interface. The experimental evaluation of the material parameters used in the LB model using nonlinear impedance spectroscopy would provide an appropriate feedback for fine tuning their effect on signal transduction using the LB model.

REFERENCES

1. Varghese, K., P. Molnar, M. Das, N. Bhargava, S. Lambert, M. S. Kindy, and J. J. Hickman. 2010. A New Target for Amyloid Beta Toxicity Validated by Standard and High-Throughput Electrophysiology. PloS One 5:e8643.
2. Bousse, L. 1996. Whole cell biosensors. Sensors and Actuators B-Chemical 34:270-275.
3. Akanda, N., P. Molnar, M. Stancescu, and J. J. Hickman. 2009. Analysis of Toxin-Induced Changes in Action Potential Shape for Drug Development. Journal of Biomolecular Screening 14:1228-1235.
4. Chiappalone, M., A. Vato, M. B. Tedesco, M. Marcoli, F. Davide, and S. Martinoia. 2003. Networks of neurons coupled to microelectrode arrays: a neuronal sensory system for pharmacological applications. Biosensors & Bioelectronics 18:627-634.
5. Chi, L. Y., J. Yu, H. Zhu, X. G. Li, S. G. Zhu, Z. Z. Li, L. C. Pettigrew, D. Grass, J. J. Hickman, and M. S. Kindy. 2010. Dual neuronal response to tumor necrosis factor-alpha following spinal cord injury. Neural Regeneration Research 5:917-926.
6. Das, M., J. W. Rumsey, N. Bhargava, M. Stancescu, and J. J. Hickman. 2010. A defined long-term in vitro tissue engineered model of neuromuscular junctions. Biomaterials 31:4880-4888.
7. Edwards, D., M. Das, P. Molnar, and J. J. Hickman. 2010. Addition of glutamate to serum-free culture promotes recovery of electrical activity in adult hippocampal neurons in vitro. Journal of Neuroscience Methods 190:155-163.
8. Bonomini, M. P., J. M. Ferrandez, and E. Fernandez. 2009. Searching for semantics in the

retinal code. Neurocomputing 72:806-813.

9. Nakamura, T., N. Morimoto, F. Goto, Y. Shioda, H. Hoshino, M. Kubota, and H. Taiji. 2012. Langerhans cell histiocytosis with disequilibrium. Auris Nasus Larynx 39:627-630.

10. Nam, S. H., M. J. Kwon, J. Lee, C. G. Lee, H. J. Yu, C. S. Ki, and M. Lee. 2012. Clinical and Genetic Analysis of Three Korean Children with Pyridoxine-Dependent Epilepsy. Annals of Clinical and Laboratory Science 42:65-72.

11. Uesaka, N., T. Mikuni, K. Hashimoto, H. Hirai, K. Sakimura, and M. Kano. 2012. Organotypic Coculture Preparation for the Study of Developmental Synapse Elimination in Mammalian Brain. Journal of Neuroscience 32:11657-11670.

12. Katayama, T., H. Kobayashi, T. Okamura, Y. Yamasaki-Katayama, T. Kibayashi, H. Kimura, K. Ohsawa, S. Kohsaka, and M. Minami. 2012. Accumulating Microglia Phagocytose Injured Neurons in Hippocampal Slice Cultures: Involvement of p38 MAP Kinase. Plos One 7.

13. Vlachos, A., C. B. Orth, G. Schneider, and T. Deller. 2012. Time-lapse imaging of granule cells in mouse entorhino-hippocampal slice cultures reveals changes in spine stability after entorhinal denervation. Journal of Comparative Neurology 520:1891-1902.

14. Rao, L., H. H. Zhou, T. Li, C. Y. Li, and Y. W. Y. Duan. 2012. Polyethylene glycol-containing polyurethane hydrogel coatings for improving the biocompatibility of neural electrodes. Acta Biomaterialia 8:2233-2242.

15. Zhang, F., M. Aghagolzadeh, and K. Oweiss. 2012. A Fully Implantable, Programmable and Multimodal Neuroprocessor for Wireless, Cortically Controlled Brain-Machine Interface Applications. Journal of Signal Processing Systems for Signal Image and Video

Technology 69:351-361.

16. Zhang, H. N., J. Shih, J. Zhu, and N. A. Kotov. 2012. Layered Nanocomposites from Gold Nanoparticles for Neural Prosthetic Devices. Nano Letters 12:3391-3398.

17. Bellamkonda, R. V., S. B. Pai, and P. Renaud. 2012. Materials for neural interfaces. Mrs Bulletin 37:557-565.

18. Mason, T. W. 1993. Fluorescent and Luminescent Probes for Biological Activity. Academic Press, London.

19. Gross, G. W., A. Harsch, B. K. Rhoades, and W. Gopel. 1997. Odor, drug and toxin analysis with neuronal networks in vitro: Extracellular array recording of network responses. Biosensors & Bioelectronics 12:373-393.

20. Pancrazio, J. J., P. P. Bey, D. S. Cuttino, J. K. Kusel, D. A. Borkholder, K. M. Shaffer, G. T. A. Kovacs, and D. A. Stenger. 1998. Portable cell-based biosensor system for toxin detection. Sensors and Actuators B-Chemical 53:179-185.

21. Xia, Y., K. V. Gopal, and G. W. Gross. 2003. Differential acute effects of fluoxetine on frontal and auditory cortex networks in vitro. Brain Research 973:151-160.

22. Amigo, J. M., J. Szczepanski, E. Wajnryb, and M. V. Sanchez-Vives. 2003. On the number of states of the neuronal sources. Biosystems 68:57-66.

23. Joye, N., A. Schmid, and Y. Leblebici. 2009. Electrical modeling of the cell-electrode interface for recording neural activity from high-density microelectrode arrays. Neurocomputing 73:250-259.

24. Bove, M., S. Martinoia, M. Grattarola, and D. Ricci. 1996. The neuron-transistor junction: Linking equivalent electric circuit models to microscopic descriptions. Thin Solid Films

285:772-775.

25. Buitenweg, J., W. L. C. Rutten, and E. Marani. 2003. Geometry-based finite-element modeling of the electrical contact between a cultured neuron and a microelectrode. IEEE Transactions on Biomedical Engineering 50:501-509.

26. Martinoia, S., P. Massobrio, M. Bove, and G. Massobrio. 2004. Cultured neurons coupled to microelectrode arrays: Circuit models, simulations and experimental data. IEEE Transactions on Biomedical Engineering 51:859-864.

27. Offenhausser, A., and W. Knoll. 2001. Cell-transistor hybrid systems and their potential applications. Trends in Biotechnology 19:62-66.

28. Weis, R., and P. Fromherz. 1997. Frequency dependent signal transfer in neuron transistors. Phys. Rev. E 55:877-889.

29. Djilas, M., C. Oles, H. Lorach, A. Bendali, J. Degardin, E. Dubus, G. Lissorgues-Bazin, L. Rousseau, R. Benosman, S. H. Ieng, S. Joucla, B. Yvert, P. Bergonzo, J. Sahel, and S. Picaud. 2011. Three-dimensional electrode arrays for retinal prostheses: modeling, geometry optimization and experimental validation. Journal of Neural Engineering 8:9.

30. Joucla, S., and B. Yvert. 2012. Modeling extracellular electrical neural stimulation: From basic understanding to MEA-based applications. J. Physiol.-Paris 106:146-158.

31. Moulin, C., A. Gliere, D. Barbier, S. Joucla, B. Yvert, P. Mailley, and R. Guillemaud. 2008. A new 3-D finite-element model based on thin-film approximation for microelectrode array recording of extracellular action potential. IEEE Transactions on Biomedical Engineering 55:683-692.

32. Cantrell, D. R., S. Inayat, A. Taflove, R. S. Ruoff, and J. B. Troy. 2008. Incorporation of the

electrode-electrolyte interface into finite-element models of metal microelectrodes. Journal of Neural Engineering 5:54-67.

33. Ignatius, M. J., N. Sawhney, A. Gupta, B. M. Thibadeau, O. R. Monteiro, and I. G. Brown. 1998. Bioactive surface coatings for nanoscale instruments: Effects on CNS neurons. J. Biomed. Mater. Res. 40:264-274.

34. Jung, D. R., D. S. Cuttino, J. J. Pancrazio, P. Manos, T. Cluster, R. S. Sathanoori, L. E. Aloi, M. G. Coulombe, M. A. Czamaski, D. A. Borkholder, G. T. A. Kovacs, P. Bey, D. A. Stenger, and J. J. Hickman. 1998. Cell-based sensor microelectrode array characterized by imaging x-ray photoelectron spectroscopy, scanning electron microscopy, impedance measurements, and extracellular recordings. J. Vac. Sci. Technol. A-Vac. Surf. Films 16:1183-1188.

35. Stelzle, M., R. Wagner, W. Nisch, W. Jagermann, R. Frohlich, and M. Schaldach. 1997. On the chemical modification of pacemaker electrodes and patterned surface functionalization of planar substrates. Biosens. Bioelectron. 12:853-865.

36. Mazzatenta, A., M. Giugliano, S. Campidelli, L. Gambazzi, L. Businaro, H. Markram, M. Prato, and L. Ballerini. 2007. Interfacing Neurons with Carbon Nanotubes: Electrical Signal Transfer and Synaptic Stimulation in Cultured Brain Circuits. J. Neurosci. 27:6931-6936.

37. Thein, M., F. Asphahani, A. Cheng, R. Buckmaster, M. Q. Zhang, and J. Xu. 2010. Response characteristics of single-cell impedance sensors employed with surface-modified microelectrodes. Biosensors & Bioelectronics 25:1963-1969.

38. Thakore, V., A. Behal, P. Molnar, D. C. Leistritz, and J. J. Hickman. 2008. Nanoscale

Nonlinear Dynamic Characterization of the Neuron-Electrode Junction. Journal of Computational and Theoretical Nanoscience 5:2164-2169.

39. Thakore, V., P. Molnar, and J. J. Hickman. 2012. An Optimization-Based Study of Equivalent Circuit Models for Representing Recordings at the Neuron-Electrode Interface. IEEE Transactions on Biomedical Engineering 59:2338-2347.

40. Marmarelis, P. Z., and V. Z. Marmarelis. 1978. Analysis of physiological systems. Plenum Press, New York.

41. Marmarelis, V. Z. 2004. Nonlinear dynamic modeling of physiological systems. John Wiley and Sons, Inc., Hoboken, NJ.

42. Fromherz, P., C. O. Muller, and R. Weis. 1993. Neuron Transistor - Electrical transfer-function measured by the patch clamp technique. Physical Review Letters 71:4079-4082.

43. Buitenweg, J. R., W. L. C. Rutten, E. Marani, S. K. L. Polman, and J. Ursum. 2002. Extracellular detection of active membrane currents in the neuron-electrode interface. Journal of Neuroscience Methods 115:211-221.

44. Buitenweg, J. R., W. L. C. Rutten, W. P. A. Willems, and J. W. van Nieuwkasteele. 1998. Measurement of sealing resistance of cell-electrode interfaces in neuronal cultures using impedance spectroscopy. Med. Biol. Eng. Comput. 36:630-637.

45. Lee, Y. W., and M. Schetzen. 1965. Measurement of Wiener Kernels of a Nonlinear System by Cross-Correlation. International Journal of Control 2:237-&.

46. Higashida, H., R. A. Streaty, W. Klee, and M. Nirenberg. 1986. Bradykinin-activated transmembrane signals are coupled via No or Ni to production of inositol 1,4,5-

trisphosphate, a second messenger in NG108-15 neuroblastoma-glioma hybrid cells. Proceedings of The National Academy of Sciences of The United States of America 83:942-946.

47. Ma, W., J. J. Pancrazio, M. Coulombe, J. Dumm, R. Sathanoori, J. L. Barker, V. C. Kowtha, D. A. Stenger, and J. J. Hickman. 1998. Neuronal and glial epitopes and transmitter-synthesizing enzymes appear in parallel with membrane excitability during neuroblastomaxglioma hybrid differentiation. Developmental Brain Research 106:155-163.

48. Braun, D., and P. Fromherz. 1998. Fluorescence Interferometry of Neuronal Cell Adhesion on Microstructured Silicon. Physical Review Letters 81:5241.

49. Ingebrandt, S., C. K. Yeung, M. Krause, and A. Offenhausser. 2005. Neuron-transistor coupling: interpretation of individual extracellular recorded signals. European Biophysics Journal with Biophysics Letters 34:144-154.

50. Brittinger, M., and P. Fromherz. 2005. Field-effect transistor with recombinant potassium channels: fast and slow response by electrical and chemical interactions. Applied Physics a-Materials Science & Processing 81:439-447.

51. Pabst, M., G. Wrobel, S. Ingebrandt, F. Sommerhage, and A. Offenhausser. 2007. Solution of the Poisson-Nernst-Planck equations in the cell-substrate interface. European Physical Journal E 24:1-8.

52. Wrobel, G., R. Seifert, S. Ingebrandt, J. Enderlein, H. Ecken, A. Baumann, U. B. Kaupp, and A. Offenhausser. 2005. Cell-transistor coupling: Investigation of potassium currents recorded with p- and n-channel FETs. Biophysical Journal 89:3628-3638.

53. Jenkner, M., and P. Fromherz. 1997. Bistability of membrane conductance in cell adhesion observed in a neuron transistor. Physical Review Letters 79:4705-4708.

54. Schatzthauer, R., and P. Fromherz. 1998. Neuron-silicon junction with voltage-gated ionic currents. European Journal of Neuroscience 10:1956-1962.

55. Fromherz, P. 1999. Extracellular recording with transistors and the distribution of ionic conductances in a cell membrane. European Biophysics Journal with Biophysics Letters 28:254-258.

56. Buitenweg, J. R., W. L. C. Rutten, and E. Marani. 2002. Modeled channel distributions explain extracellular recordings from cultured neurons sealed to microelectrodes. IEEE Transactions on Biomedical Engineering 49:1580-1590.

57. Hodgkin, A. L., and A. F. Huxley. 1952. A quantitative description of membrane current and its application to conduction and excitation in nerve. Journal of Physiology 117:500-544.

58. Mohan, D. K., P. Molnar, and J. J. Hickman. 2006. Toxin detection based on action potential shape analysis using a realistic mathematical model of differentiated NG108-15 cells. Biosensors & Bioelectronics 21:1804-1811.

59. Destexhe, A., and J. R. Huguenard. 2000. Nonlinear thermodynamic models of voltage-dependent currents. J. Comput. Neurosci. 9:259-270.

60. Gabay, T., M. Ben-David, I. Kalifa, R. Sorkin, Z. R. Abrams, E. Ben-Jacob, and Y. Hanein. 2007. Electro-chemical and biological properties of carbon nanotube based multi-electrode arrays. Nanotechnology 18:6.

61. http://www.multichannelsystems.com.

62. Muralidharan, V. S. 1997. Warburg impedance - Basics revisited. Anti-Corrosion Methods and Materials 44:26-&.

63. Patolsky, F., B. P. Timko, G. H. Yu, Y. Fang, A. B. Greytak, G. F. Zheng, and C. M. Lieber. 2006. Detection, stimulation, and inhibition of neuronal signals with high-density nanowire transistor arrays. Science 313:1100-1104.

64. Patolsky, F., G. Zheng, and C. M. Lieber. 2006. Nanowire sensors for medicine and the life sciences. Nanomedicine 1:51-65.

65. Kotov, N. A., J. O. Winter, I. P. Clements, E. Jan, B. P. Timko, S. Campidelli, S. Pathak, A. Mazzatenta, C. M. Lieber, M. Prato, R. V. Bellamkonda, G. A. Silva, N. W. S. Kam, F. Patolsky, and L. Ballerini. 2009. Nanomaterials for Neural Interfaces. Advanced Materials 21:3970-4004.

66. Barsoukov, E., and J. R. Macdonald, editors. 2005. Impedance Spectroscopy - Theory, Experiment and Applications. John Wiley and Sons, Inc., Hoboken, NJ.

67. Lvovich, V. F. 2012. Impedance Spectroscopy - Applications to Electrochemical and Dielectric Phenomena. John Wiley and Sons, Inc., Hoboken.

68. Butcher, P. N., and D. Cotter. 1990. The Elements of Nonlinear Optics. Cambridge University Press, Cambridge.

69. Blakecoleman, B. C., M. J. Hutchings, and P. Silley. 1994. Harmonic Signatures of Microorganisms. Biosensors & Bioelectronics 9:231-242.

70. Hutchings, M. J., B. C. Blakecoleman, and P. Silley. 1994. Harmonic-Generation in Nonlinear Biological-Systems. Biosensors & Bioelectronics 9:91-103.

71. Munn, R. W. 1993. Microscopic Theory of Dielectric Response for Molecular Multilayers.

Journal of Chemical Physics 99:1404-1408.

72. Alieva, E. V., G. Beitel, L. A. Kuzik, A. A. Sigarev, V. A. Yakovlev, G. N. Zhizhin, A. F. G. van der Meer, and M. J. van der Wiel. 1998. Linear and nonlinear FEL-SEW spectroscopic characterization of nanometer-thick films. Journal of Molecular Structure 449:119-129.

73. Chang, B. Y., and S. M. Park. 2010. Electrochemical Impedance Spectroscopy. In Annual Review of Analytical Chemistry, Vol 3. 207-229.

74. Blajiev, O. L., R. Pintelon, and A. Hubin. 2005. Detection and evaluation of measurement noise and stochastic non-linear distortions in electrochemical impedance measurements by a model based on a broadband periodic excitation. Journal of Electroanalytical Chemistry 576:65-72.

75. Kiel, M., O. Bohlen, and D. U. Sauer. 2008. Harmonic analysis for identification of nonlinearities in impedance spectroscopy. Electrochimica Acta 53:7367-7374.

76. Xu, N., and J. Riley. 2011. Nonlinear analysis of a classical system: The double-layer capacitor. Electrochemistry Communications 13:1077-1081.

77. Karniadakis, G., A. Beskok, and N. Aluru. 2005. Microflows and Nanoflows - Fundamentals and Simulation. Springer-Science+Business Media, Inc., New York.

78. Patankar, N. A., and H. H. Hu. 1998. Numerical simulation of electroosmotic flow. Anal. Chem. 70:1870-1881.

79. Frisch, U., B. Hasslacher, and Y. Pomeau. 1986. Lattice gas cellular automata for the Navier-Stokes equation. Physical Review Letters 56:1505-1508.

80. Wolf-Gladrow, D. A. 2000. Lattice Gas Cellular Automata and Lattice Boltzmann Models. Springer-Verlag, Berlin.

81. Succi, S. 2001. The Lattice Boltzmann Equation for Fluid Dynamics and Beyond. Clarendon Press, Oxford.

82. McNamara, G. R., and G. Zanetti. 1988. Use of the Boltzmann equation to simulate lattice-gas automata. Physical Review Letters 61:2332-2335.

83. Qian, Y. H., D. Dhumieres, and P. Lallemand. 1992. Lattice BGK models for Navier-Stokes equation. Europhysics Letters 17:479-484.

84. Higuera, F. J., and J. Jimenez. 1989. Boltzmann approach to lattice gas simulations. Europhysics Letters 9:663-668.

85. Bhatnagar, P. L., E. P. Gross, and M. Krook. 1954. A model for collision processes in gases. I. Small amplitude processes in charged and neutral one-component systems. Physical Review 94:511-525.

86. He, X. Y., and L. S. Luo. 1997. Theory of the lattice Boltzmann method: From the Boltzmann equation to the lattice Boltzmann equation. Physical Review E 56:6811-6817.

87. He, X. Y., and L. S. Luo. 1997. A priori derivation of the lattice Boltzmann equation. Physical Review E 55:R6333-R6336.

88. Panton, R. L. 1984. Incompressible Flows. John Wiley and Sons, Inc., New York.

89. Zou, Q. S., and X. Y. He. 1997. On pressure and velocity boundary conditions for the lattice Boltzmann BGK model. Physics of Fluids 9:1591-1598.

90. Wang, J. K., M. Wang, and Z. X. Li. 2006. Lattice Poisson-Boltzmann simulations of electro-osmotic flows in microchannels. Journal of Colloid and Interface Science 296:729-736.

91. Tang, G. H., Z. Li, J. K. Wang, Y. L. He, and W. Q. Tao. 2006. Electroosmotic flow and

mixing in microchannels with the lattice Boltzmann method. Journal of Applied Physics 100.

92. He, X. Y., N. Li, and B. Goldstein. 2000. Lattice Boltzmann simulation of diffusion-convection systems with surface chemical reaction. Molecular Simulation 25:145-156.

93. Reif, F. 1985. Fundamentals of Statistical and Thermal Physics. McGraw-Hill, Inc., Singapore.

94. Chapman, S., and T. G. Cowling. 1970. The Mathematical Theory of Non-Uniform Gases. Cambridge University Press, London.

95. Lallemand, P., and L. S. Luo. 2000. Theory of the lattice Boltzmann method: Dispersion, dissipation, isotropy, Galilean invariance, and stability. Physical Review E 61:6546-6562.

96. Luo, L. S., W. Liao, X. W. Chen, Y. Peng, and W. Zhang. 2011. Numerics of the lattice Boltzmann method: Effects of collision models on the lattice Boltzmann simulations. Physical Review E 83.

97. Guo, Z. L., C. G. Zheng, and B. C. Shi. 2002. Discrete lattice effects on the forcing term in the lattice Boltzmann method. Physical Review E 65.

98. Dodo, T., M. Sugawa, E. Nonaka, and S. Ikawa. 2002. Submillimeter spectroscopic study of concentrated electrolyte solutions as high density plasma. Journal of Chemical Physics 116:5701-5707.

99. He, X. Y., and N. Li. 2000. Lattice Boltzmann simulation of electrochemical systems. Computer Physics Communications 129:158-166.

100. Heil, S. R., and M. Holz. 1998. Electrical transport in a disordered medium: NMR measurement of diffusivity and electrical mobility of ionic charge carriers. Journal of

Magnetic Resonance 135:17-22.

101. Tankovsky, N., and E. Syrakov. 2009. A modified Einstein-Nernst relation between mobility and diffusion of charges to evaluate the non-equilibrium, transient processes of ions in electrolytes. Ionics 15:589-595.

102. Tankovsky, N., and E. Syrakov. 2005. Transient ion fluxes, driven by an external electric field in a thin electrolytic cell with blocking electrodes. Journal of Physics-Condensed Matter 17:1225-1238.

103. Ngai, K. L., and F. S. Liu. 1981. Dispersive diffusion transport and noise, time-dependent diffusion coefficient, generalized Einstein-Nernst relatio, and dispersive diffusion controlled unimolecular and biomolecular reactions. Physical Review B 24:1049-1064.

104. Fang, B., X. L. Wang, X. Z. Tang, and P. F. Zhu. 2002. Ionic interactions and transport mechanism in polyurethane electrolytes. Journal of Applied Polymer Science 83:785-790.

105. Saito, Y., H. Kataok, and S. Deki. 2001. Ionic mobility measurements applying a controlled direct electric field on pulsed gradient spin echo nuclear magnetic resonance. Journal of the Electrochemical Society 148:E382-E385.

106. Berlin, Y. A., L. D. A. Siebbeles, and A. A. Zharikov. 1999. Deviation from the Einstein relation: mobility of unrelaxed carriers. Chemical Physics Letters 305:123-131.

107. Jungemann, C., B. Neinhus, and B. Meinerzhagen. 2001. Investigation of the local force approximation in numerical device simulation by full-band Monte Carlo simulation. VLSI Design 13:281-285.

108. Barkai, E., and V. N. Fleurov. 1998. Generalized Einstein relation: A stochastic modeling

approach. Physical Review E 58:1296-1310.

109. Metzler, R., E. Barkai, and J. Klafter. 1999. Anomalous diffusion and relaxation close to thermal equilibrium: A fractional Fokker-Planck equation approach. Physical Review Letters 82:3563-3567.